Repump Methods for Magneto Optically Trapped Calcium Atoms

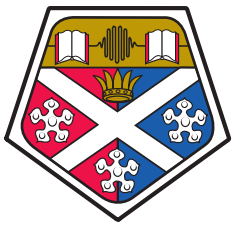

Christopher Burrows

Department of Physics and SUPA

University of Strathclyde

A thesis presented in the fulfilment of the requirements for the degree of

Doctor of Philosophy

2012

This thesis is the result of the author's original research. It has been composed by the author and has not been previously submitted for examination which has lead to the award of a degree.

Signed: Date:

Abstract

This thesis presents work done on the calcium magneto optic trap experiment at the University of Strathclyde.

The apparatus used to cool and trap $\sim 10^6 - 10^7$ ^{40}Ca atoms is summarised within.

Results pertaining to the 672 nm repump laser are presented. The laser is used to increase the number of detected trapped atoms by more than an order of magnitude. A rate equation model used to simulate the behaviour of the repumped MOT is introduced. It is also used to detect some of the naturally occurring calcium isotopes (and their frequency shifts), ^{42,44,48}Ca, the latter of which has less than 0.2% natural abundance. Expected isotope shifts for three other isotopes, ^{41,43,46}Ca, are calculated.

Work carried out on the 1530 nm repump laser is presented. Alterations to the rate equation model are presented. When used in conjunction with the 672 nm laser, the 1530 nm laser increases the number of detected trapped atoms by an extra $20 - 40\%$ over and above the increase due to the 672 nm laser. The lifetime of atoms trapped in the $^3P_2$ level is experimentally determined. Work carried out on a 1530 nm fibre amplifier is presented, showing that increased power has little effect.

The design, construction and testing of an interference filter based external cavity diode laser is presented, along with measurements made of the 370 HZ intercombination line $4s^2\ ^1S_0 - 4s4p\ ^3P_1$. Explanations for the broader linewidths seen are offered.

Acknowledgements

Wow. The lesser spotted *physics thesis*. Well, who would have thought I'd get this far or produce one of these? It's been a long process and it likely wouldn't have happened but for the help of a lot of people.

The first and most important of these is without doubt my first supervisor, Professor Erling Riis. Without his passion for the subject and ability to dumb it down to my level, this thesis would probably never have seen the light of day. He always seemed able to produce just the piece of equipment you needed from his seemingly magical pockets at any time and always had a suggestion when things in the lab weren't making sense. His sense of humour also made working with him a genuine pleasure. What's more, Erling's unwavering belief in me and my abilities in the lab made me believe in myself more than I would have thought possible before I began my PhD studies. Thank you, Erling. You have helped make the last three and a half years an experience to be remembered.

Thanks should also go to my second supervisor, Dr. Aidan Arnold. While our paths didn't often cross on experimental matters, he always had a suggestion to offer when problems needed solving and always apologised when he was caught 'borrowing' things from my lab...

During the first year or so of my PhD, I had the pleasure of working with Dr. Umakanth Dammalapati in the lab. Without him showing me the ropes and teaching me how to run the experiment I have little doubt things would have moved much more slowly than they did. His experience early on was invaluable to me.

Dr. Paul Griffin. 'Griff knows everything' was a popular saying among some of the PhD students and though he might try to deny it, his almost encyclopedic knowledge will have been a great help to more than just me. Not only that, he

was always willing to answer any questions, lend a hand in the lab or simply offer suggestions with a smile on his face, never once seeming to get annoyed at me saying 'Hey, Griff. Stupid question, but...' even if it was my 113th stupid question of the year. Cheers, Griff.

Matt... sorry, Dr. Matthieu Vangeleyn. Well, I've known him longer as a student than I have as a Doctor. Matt's experience and expertise in electronics was a great help more than once. He was very clumsy, though, he kept on dropping things. The others in the photonics group helped make the time go more quickly (especially on Friday lunchtimes) and were always keen to lend a hand to the poor man in the calcium lab all on his own. Aline, Neal, Yoanne, Alessio, Mateusz, Kenneth, Stephanie, thanks to all of you. To the newer guys, Chris, Elmar, Jesus, Savino, Pedro, James, Andrew, Chidi, best of luck for the rest of your time at Strathclyde.

I'd also like to single out two of the newer post-docs in the photonics group: Dr. Jon Pritchard and Dr. Graham Bruce. As two people who had very recently written their own thesii (thesises? theses?), their support and help while writing this thesis was more useful to me than I can quantify. Cheers, guys.

Last, but by no means least for those at Strathclyde, are the guys in the workshop, Bob Wylie and Ewan Maclagan. Without them the setup just wouldn't exist. It is as simple as that - they put it together, maintain it and make any and all alterations and improvements required to the highest standard. Truly, masters of their craft.

Outside of Strathclyde, I want to take the time to thank my parents, Mike and Margaret Burrows. The pair of you have given me more support than I probably deserve and have always, *always* encouraged and believed in me. This thesis is a testament to that. Thank you so very, very much.

My friends Skitz, Kwok, Lorna Jason and Bob. Two of them have been here so they know what it's like. The rest, well, it was always good to be able to unwind with them in the pub at the weekend. They kept me sane, simple as that.

Of all my friends, though, Adam Weir deserves the most credit for keeping me sane. We did our degrees together and though he now lives 3000 miles away, it's really like not much has changed. He's always willing to listen to me bitch

about this and that without so much as a hint of a complaint. When I need it, he'll distract me with something shiny, or inane talk about that one bit in that one song that just *works* for some unquantifiable reason or another. When I need a kick up the arse, he'll do that too. Cheers, man.

Wow, this has dragged on a bit, hasn't it? Well, to everyone mentioned, and anyone I've forgotten to mention: thank you.

Contents

List of Figures

Chapter 1

Introduction

1.1 History of laser cooling

Since the first publications on the possibility of laser cooling atoms [1] and ions [2] in 1975, the science of laser cooling has become one of the most highly studied fields in atomic physics. As of 2012, dozens of research groups all over the world [3] are involved in cold atom research using a variety of atomic species, with a variety of different experimental aims and configurations.

It took some time for these ideas of 1975 to be experimentally realised, however. It wasn't until 1982 that Phillips and Metcalf showed a beam of neutral sodium atoms being slowed by way of a counter propagating laser beam and a spatially varying magnetic field [4]. Following this, in 1985, Steven Chu and his group [5] slowed and cooled a cloud of neutral sodium atoms in the three spatial dimensions by way of three pairs of orthogonal, counter propagating laser beams in a configuration referred to as optical molasses. A temperature of some $240\mu K$ was attained.

Shortly before this was published, Philips and Metcalf published an article [6] in which they showed that neutral atoms could be trapped in a quadrupole magnetic field. By combining this with the 3D optical molasses, the magneto-optic trap (MOT) was born [7].

The lowest temperature achievable via laser cooling alone (Doppler cooling) is known as the Doppler temperature limit. This was well known at the time a surprising result was published in 1988 [8]. Temperatures below the Doppler

temperature limit had been experimentally observed in optical molasses. This soon led to the understanding that Doppler cooling theory could not be applied to multi-level atoms - it was too simple. Dalibard and Cohen-Tannoudji [9] and Steven Chu's group [10, 11] both published articles which expanded laser cooling theory to explain how multi-level atoms could be incorporated in 1989.

Potentially one of the most significant achievements in the field of laser cooling was when Bose-Einstein condensation (BEC) was achieved for the first time [12, 13]. BEC was first predicted in 1924 by Indian physicist Satyendra Bose and Albert Einstein [14, 15]. BEC occurs when an ensemble of atoms with integer spin (bosons) have a suitably high phase space density (PSD) = $n\lambda_{dB}^3$, where n is the atom number density and λ_{dB} is the thermal de Broglie wavelength. A high PSD simply means that a group of atoms have very narrow spatial and velocity distributions. The result is that, below a certain temperature λ_{dB} will be larger than the inter particle spacing of a group of bosons and they become indistinguishable from one another and all occupy the lowest possible energy state of the system. We call this a BEC.

Typically, one cannot obtain BEC with laser cooling alone; the re-absorption and emission of photons stops a MOT from reaching suitable BEC temperatures and PSDs [16]. To obtain a BEC, laser cooled atoms were transferred to magnetic traps where the re-absorption of photons ceased to be a problem [17] and a technique known as evaporative cooling was developed to lower their temperature further [18]. To best explain evaporative cooling, one should imagine a cup of hot coffee. Steam rises from the coffee and the temperature drops steadily until it will no longer burn the roof of your mouth off. Then you drink it. Evaporative cooling follows the same principle by lowering the sides of the magnetic trap such that the atoms closer to the top of the trap (i.e. the hotter atoms) will escape. This then lowers the average temperature of the whole ensemble. This technique was used by two groups in 1995 to produce BECs of rubidium and sodium atoms.

It is also possible to laser cool fermions (i.e. atoms with non-integer spin) to produce a degenerate Fermi gas [19]. Unlike bosons, fermions cannot collapse to the same energy state due to the Pauli exclusion principle, so each atom will inhabit the lowest available energy state.

In the field of laser cooling in atomic physics, two key advances have paved the way for future research to such a degree that they were awarded Nobel prizes. In 1997, Steven Chu, William Phillips and Claude Cohen-Tannoudji shared the Nobel prize in physics for their contributions to the experimental realisation and theoretical description of laser cooling [20, 21, 22]. In 2001 as a result of achieving BEC for the very first time, Carl Wieman, Eric Cornell and Wolfgang Ketterle were awarded the Nobel prize in physics [23, 24].

1.2 Different atomic species

For much of the early period of BEC research it was elements in group I of the periodic table, the so-called alkaline metals, that were almost exclusively used. That is, atoms with a single free electron orbiting the core. This is due to the fact that the type of lasers usually necessary for laser cooling, were readily available in narrow-linewidth near-IR laser diodes, developed in the early 1990s. To date there have been BECs in many group I elements: hydrogen (which doesn't actually involve laser cooling) [25], lithium [26], sodium (which uses a dye laser rather than a diode laser) [13], potassium [27], rubidium [12] and cesium [28]. Progress was not strictly limited to group I elements, however: BECs of metastable helium [29], ytterbium [30], chromium [31] and dysprosium [32] have also been made.

It was only much more recently that more exotic elements from group II, the alkaline earths, were successfully cooled to BEC. In 2009, the PTB group in Germany produced a BEC of calcium [33] and the same year groups in Austria [34] and Texas [35] produced BECs of strontium atoms. A year later, the same two groups produced BECs of two different strontium isotopes [36, 37]

The reasons behind the desire to laser cool the alkaline earths are numerous. The even isotopes have no nuclear spin and so have a singlet ground state with no sublevels. This is ideal for laser cooling as it produces and almost perfect two level system and allows a MOT to be attained without the need for a repump laser, as is the case with the alkaline metals. They also have an additional triplet energy level scheme coupled to the singlet scheme by narrow transitions known as intercombination lines.

These intercombination lines, a type of forbidden transition, are the other main reason that laser cooling of the alkali earths is an attractive prospect. These very narrow transitions offer researchers a means to further increase the precision of one of the most accurately known physical constants: the second. Seconds are currently defined as 'The second is the duration of 9 192 631 770 periods of the radiation corresponding to the transition between the two hyperfine levels of the ground state of the caesium 133 atom' [38]. In the last decade or so, the ${}^1S_0 - {}^3P_1$ transition at 657 nm in calcium has been suggested as a possible future optical frequency standard [39, 40]. A strontium optical clock has recently been demonstrated [41].

In addition to this, the very narrow intercombination line could theoretically be used to cool to BEC entirely optically. That is, without having to rely on the inherently inefficient process of evaporative cooling. [While there has since been another calcium BEC [42], evaporative cooling was still used.] It should be possible to do this because the Doppler temperature limit is related to the linewidth of the transition being driven; the narrower the transition, the lower the Doppler temperature. Compare the main cooling transition of calcium with a linewidth of ~ 35 MHz and $T_D = \sim 1$ mK with the intercombination line with linewidth 370 Hz and T_D is in the tens of nK region.

The obstacle to be overcome for an all optical BEC of calcium is that the transition to be used is so weak that the cooled atoms cannot be supported against gravity by it, unlike in strontium where the transition is much broader. If the atoms were loaded into an optical dipole trap [43], they could be held against gravity and cooled.

Another challenge for this line of research is to develop a laser source with linewidth comparable to or narrower than the transition. This poses a considerable challenge but is possible [44]. Another route that can be taken is to artificially broaden the intercombination line transition by 'quenching' the lifetime of the ${}^3P_1$ state by exciting atoms to higher energy levels which more promptly decay to the ground state [45]. The drawback with this approach is broadening the transition increases the Doppler temperature and thus it could be argued that this would partially defeat the point.

1.3 Experimental goals

The broad goals of the calcium experiment at the University of Strathclyde are simple: attain BEC purely by optical means. By doing so, we will be able to circumvent the extremely lossy process of evaporative cooling, allowing us to attain BECs of far more atoms. By doing so, and by making use of a dipole trap, it should be possible to perform atom interferometry on two entirely separate BECs. The more typical method of using BECs for atom interferometry has involved splitting a single BEC and recombining it. By using two separate BECs, any possible phase relationship between the two BECs being interfered is removed. It should also be possible to perform a measurement of the optical frequency standard on the $4s^2\ ^1S_0 - 4s3d\ ^3P_1$ transition.

While calcium BECs have been achieved by different groups over the past three years [33, 42], most of the work with group II elements has been with strontium [34, 35, 36, 37] due to improvements in cooling techniques allowing those working with strontium to finally attain a high enough phase space density to achieve BEC. However, work presented in this thesis, outlined below, should make calcium seem an attractive prospect once again. The various lasers investigated in this thesis have improved the number of trapped atoms attainable by an order of magnitude and have presented a potential route to calcium BEC that should be much more efficient than has been used previously [33, 42].

1.4 Thesis layout

The work presented in this thesis will be separated into chapters, as follows

- **Chapter 2** will explain the background theory behind laser cooling and explain the specifics behind the laser cooling of calcium in particular. The experimental setup used throughout this work will also be presented and explained.

- **Chapter 3** will explain in detail the work carried out on the first of the repump lasers used in this experiment, the 672 nm $4s3d\ ^1D_2 - 4s4p\ ^1P_1$ transition. The benefits of increased atom number, trap lifetime and loading

rate will be explained and the first iteration of the rate equation model used will be presented. The latter part of the chapter will present our work on measuring the isotope shifts on this transition for several even isotopes. Expected isotope shifts for other isotopes will also be presented.

- **Chapter 4** will present and explain the work on the second repump transition used: the $4s4p\,^3P_2 - 4s3d\,^1D_2$ at 1530 nm. The benefits when used in conjunction with the 672 nm repump laser will be presented and explained, as will the drawbacks of using this laser on its own. The definitive rate equation model will be introduced, explained and rigorously tested. Also in this chapter will be investigations on the effects of the intensity of both repump lasers, particularly that of the 1530 nm laser due to the presence of a fiber amplifier at this wavelength. A measurement of the transition wavelength will also be presented.

- **Chapter 5** will present work on the design, construction and testing of a novel, interference filter based external cavity diode laser for use on the $4s^2\,^1S_0 - 4s4p\,^3P_1$ intercombination line at 657 nm. Preliminary results on the laser's interaction with the transition will be presented, followed by a comparison with the results achieved with the laser locked to a Fabry-Perot cavity.

- **Chapter 6** will consist of a brief summary of the thesis as a whole, together with some suggestions for future work to be carried out on the calcium MOT experiment.

1.5 Note

Some of the work presented in this thesis has already led to publication in scientific journals. These publications form the backbone of Chapters 3 and 4.

Chapter 3 is based on the paper 'Spectroscopy and isotope shifts of the $4s3d\,^1D_2 - 4s5p\,^1P_1$ repumping transition in magneto-optically trapped calcium atoms' (Physical Review A **81**, 023424 (2010)) [46]. My responsibilities for the work carried out which led to this publication were; making the 672 nm laser work

at the desired wavelength and maintaining it there, setting up the experiment such that the laser overlapped with the MOT, helping to make the measurements presented, aligning the laser into the ULE cavity for the isotope shift measurements, making said measurements and the data analysis of the isotope shift data taken.

Chapter 4 is based on the paper 'Laser spectroscopy of the $4s4p\,^3P_2 - 4s3d\,^1D_2$ transition on magnetically trapped calcium atoms' (Physical Review A **83**, 062513 (2011)) [47]. My responsibilities for the work carried out which led to this publication were; making the 1530 nm laser work at the desired wavelength and maintaining it there, co-aligning the 1530 nm laser beam with the 672 nm laser beam, setting up the timing mechanism for creating the laser pulses used, taking the necessary data for the effects of the 1530 nm laser and measuring the lifetime of the $^3P_2$ state atoms.

Chapter 2

The experimental setup and the background theory involved

The experimental apparatus used has previously been described in detail in [48], [49] and [50] but a brief outline is included here.

2.1 Introduction

To properly describe the apparatus used in this experiment and the theory behind its operation it seems best to proceed step by step, starting with the principles and theory of laser cooling and aspects of this which will be used in the experiment. Following this, the physical properties of calcium will be explained, leading to an explanation of the laser systems required for calcium in general and this experimental setup in particular. Finally in this chapter the vacuum system necessary for this experiment is explained.

2.2 Laser Cooling

Before any more is said, it is important to explain the process of laser cooling as so much of what is involved in this work relies critically on the process.

The layman's analogy of laser cooling is to imagine slowing down a charging elephant by firing a stream of tennis balls at it. Using this analogy, the elephant is a moving atom and the tennis balls represent the photons in a counter-propagating laser beam. In order to slow the atom down, the laser in question

must have a wavelength close to that of an atomic transition and will typically be detuned to the red of said transition so the Doppler shift of the approaching atom moves the laser into resonance with the transition in question. With the laser resonant with an atomic transition, the atom will absorb photons, leading to excitation to an excited state, followed by a photon being emitted as the atom decays back to the lower state. The absorption of a photon from the laser will result in a momentum kick anti-parallel to the motion of the atom: the atom will recoil with velocity $\nu_{\mathrm{r}} = \hbar\ k/M$($\hbar$ is the reduced Planck's constant, $k = 2\pi/\lambda$ (with λ the wavelength), M the mass of the atom), which is ∼2.3 cm/s for the $4s^2\ {}^1S_0 - 4s4p\ {}^1P_1$ transition in calcium. The atom will also receive a momentum kick from the emitted photon, but because the direction in which said photon is emitted is isotropic over many absoprtion/emission cycles, these momentum contributions average out to zero. Hence we consider only incoming photons as having an effect on the velocity of the atom. This is shown diagrammatically in Fig. 2.1.

The force exerted on an atom in a cooling laser beam is simply down to Newton's second law of motion

$$F = \frac{\Delta p}{\Delta t} = \frac{\hbar k}{1/\Gamma_p}, \tag{2.1}$$

where $\underline{\Delta p} = \hbar\underline{k}$ is the momentum change and Γ_p is the scattering rate. This simplifies to

$$\underline{F} = \hbar\underline{k}\Gamma_{\mathrm{p}}, \tag{2.2}$$

where Γ_{p} is given by

$$\Gamma_{\mathrm{p}} = \frac{S_0(\Gamma/2)}{1 + S_0 + (2\Delta/\Gamma)^2} \tag{2.3}$$

and

I is the intensity,

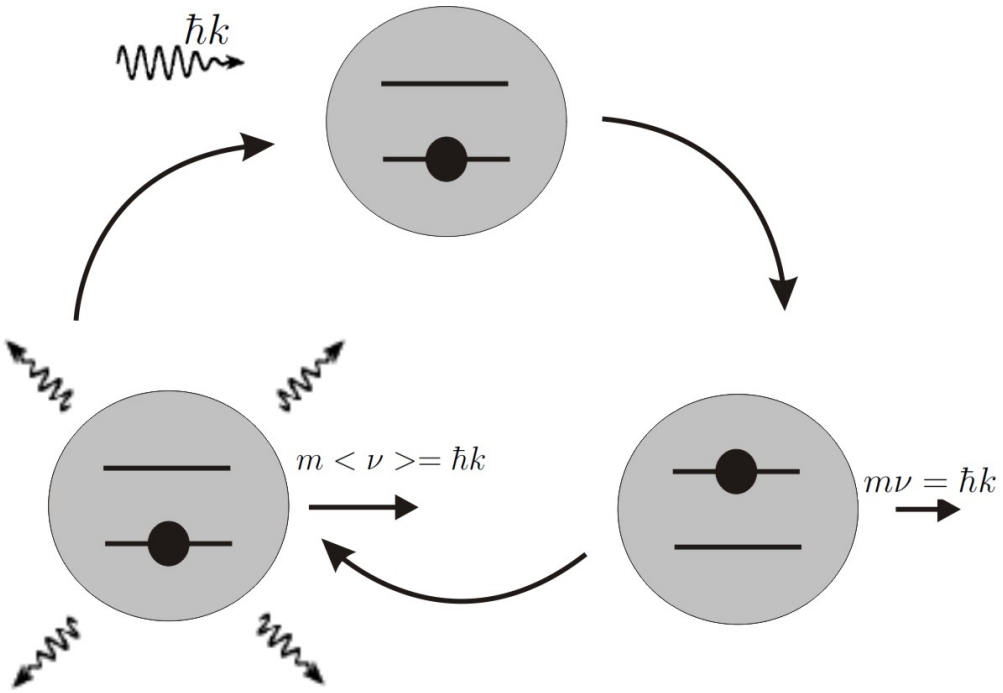

Figure 2.1: A representation of the absorption/emission cycle that takes place during laser cooling. An atom absorbs a photon of momentum $\hbar\ k$ and gets excited up to a higher energy level. This absorption will impart momentum to the atom anti-parallel to the photon's direction of travel, causing the atom to recoil with velocity $\nu_{\mathrm{r}} = \hbar\ k/M$. The atom will then emit a photon of roughly the same wavelength and decay back to the ground state, which will impart the same momentum kick, but in a random direction. As this random emission will be symmetric over many absorption/emission cycles, the average momentum imparted by the emissions will be zero. Thus, the only change in momentum comes from the incoming laser beam [16].

$S_0 = I/I_s$ is the saturation parameter, (saturation being when there are as many atoms in the excited state as there are in the ground state, which cannot be improved upon),

$I_s = \frac{\pi hc}{3\lambda^3\tau}$ is the saturation intensity,

τ is the excited state lifetime,

Γ is the linewidth of the transition and

Δ is the detuning from resonance.

Two properties an element must have for effective laser cooling are that there must be a broad drivable line between the ground and excited states (the linewidth of these transitions is related to their strength due to the fact that the linewidth is simply the inverse of the excited state lifetime and is a measure of how many decays per second take place. The faster the decay rate, the more often the atoms will cycle back and forth allowing for more effective laser cooling) and this transition must be closed, meaning that atoms excited to the upper state must decay to the ground state and not other excited states.

However, all this said, just a laser beam tuned to an atomic resonance will not be enough to effectively laser cool. Due to the changing Doppler shift experienced by a decelerating atom, it will only be in resonance with the laser beam very briefly and so will only briefly experience the slowing effect. In order to slow the atoms down, use is made of the Zeeman effect.

2.2.1 Zeeman Slower

The Zeeman effect is a shifting of atomic energy levels when an atom is placed in a magnetic field. As this means the frequency of a transition also changes, the Zeeman effect can be used to tune an atom into or out of resonance with a laser beam.

The shift in atomic energy levels when in a magnetic field $\mathbf{B} = B(z)$ is given by

$$\Delta E = \mu_\beta g_J m_J B(z), \tag{2.4}$$

where

μ_B is the Bohr magneton,

m_J is the magnetic quantum number, and

g_J is the Landé g-factor for the fine structure level J and is given by, using standard Russel-Saunders notation [51],

$$g_J = \frac{3}{2} + \frac{S(S+1) - L(L+1)}{2J(J+1)}, \tag{2.5}$$

which, for a $^1P_1$ state, for example, is simply 1 and is 3/2 for a $^3P_2$. Using standard Russell-Saunders/LS notation, the atomic state of an atom is described by

$$^{2S+1}L_J \tag{2.6}$$

Where S is the total spin quantum number, L is the orbital quantum number and J is the total angular momentum quantum number. For an ideal, two level atom with ground state J = 0 and excited state J = 1, the Zeeman effect will split the excited state energy level into three magnetic sublevels, $m_J = -1, 0, 1$ which are excited by σ^-, π, σ^+ polarised light, respectively, defined relative to the z-direction in the 1D case.

If the magnetic field applied is spatially varying and carefully chosen then the Zeeman shift will exactly cancel the Doppler shift that pushes the atoms out of resonance with the oncoming laser even as they are slowed by it along the entire length of the slower. The equation for such a magnetic field is given below [52]

$$B(z) = B_\mathrm{b} + B_0\sqrt{1 - \frac{z}{z_0}}, \tag{2.7}$$

where

B_b is the bias field,
$B_0 = \hbar k v_0/\mu_B$,
ν_0 is the maximal initial velocity of the atoms,
z is the distance along the slower,
$z_0 = \frac{Mv_0^2}{\eta\hbar k\Gamma}$ is the length of the slower,
M is the atomic mass for ^{40}Ca),
$\eta = a/a_{\max}$,
a is the acceleration (negative in the case of slowing) and
$a_{\max} = \frac{\hbar k\Gamma}{2M}$

A representation of a Zeeman slower, constructed from a tapered copper solenoid with a separate coil of constant diameter, together with a representation of the shape of the field produced is shown in Fig. 2.2. This shape of field is chosen because as the atoms are slowed down, the distance they move in a set time is reduced. As the atoms undergo a scattering event at the scattering rate Γ_p, the field will be required to change more severely to keep up with this change.

2.2.2 Optical molasses

The principle of laser cooling using a single laser was explained in an earlier part of this chapter. If, instead, two lasers are used and are aligned anti-parallel to one another and both are slightly red detuned from resonance a one dimensional (1D) *optical molasses* can be set up. If we take the Doppler shift into account, the total detuning from resonance will be $\delta - \underline{k} \cdot \underline{v}$. The force exerted on atoms in a 1D optical molasses is then given by:

$$\underline{F}_{\mathrm{OM}} = \hbar\underline{k}\frac{\Gamma}{2}\left[\frac{S_0}{1+S_0+(2(\delta-\underline{k}\ \underline{v})/\Gamma)^2} - \frac{S_0}{1+S_0+(2(\delta+\underline{k}\ \underline{v})/\Gamma)^2}\right] . \quad (2.8)$$

This leads to, if $|kv| << \delta$, [8]

$$\underline{F}_{\mathrm{OM}} = 4\hbar\underline{k}S_0\frac{kv(2\delta/\Gamma)}{[1+S_0+(2\delta/\Gamma)^2]^2} . \quad (2.9)$$

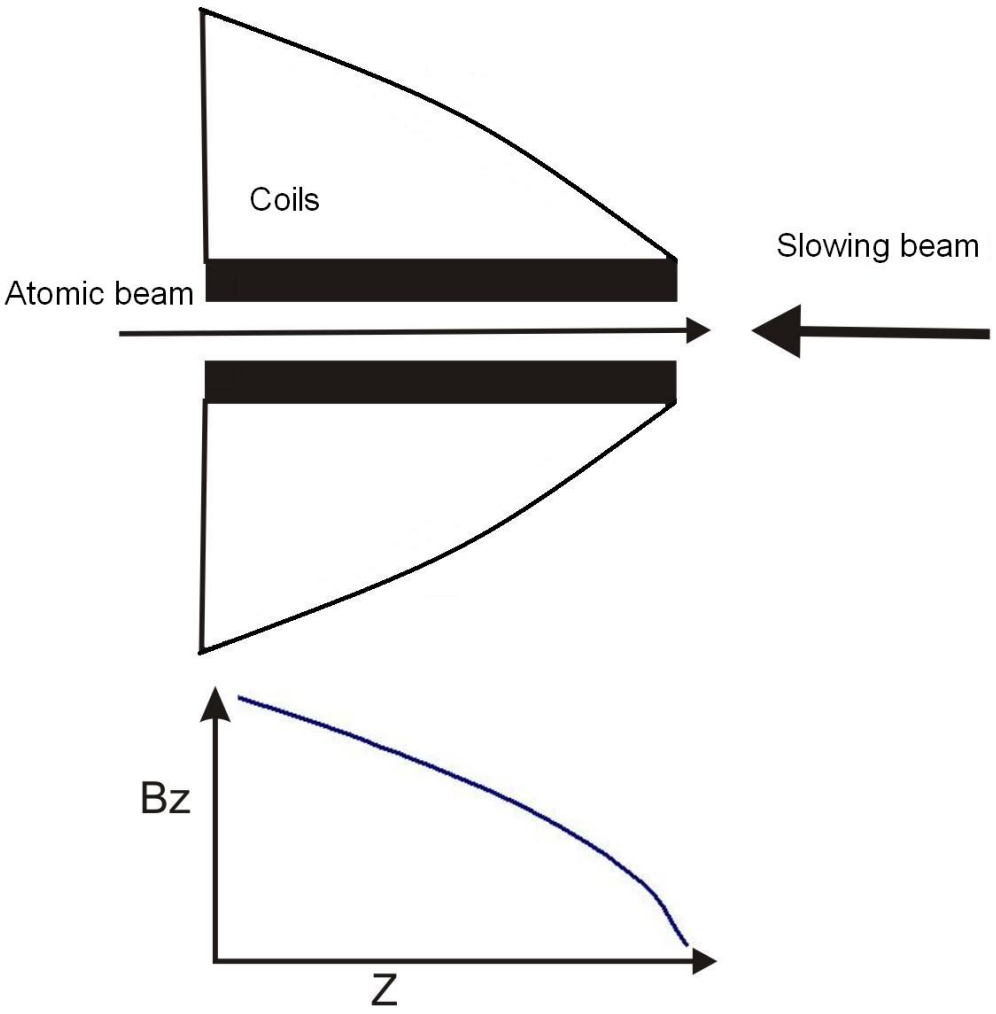

Figure 2.2: Shape of the Zeeman slower and the resulting spatially varying magnetic field.

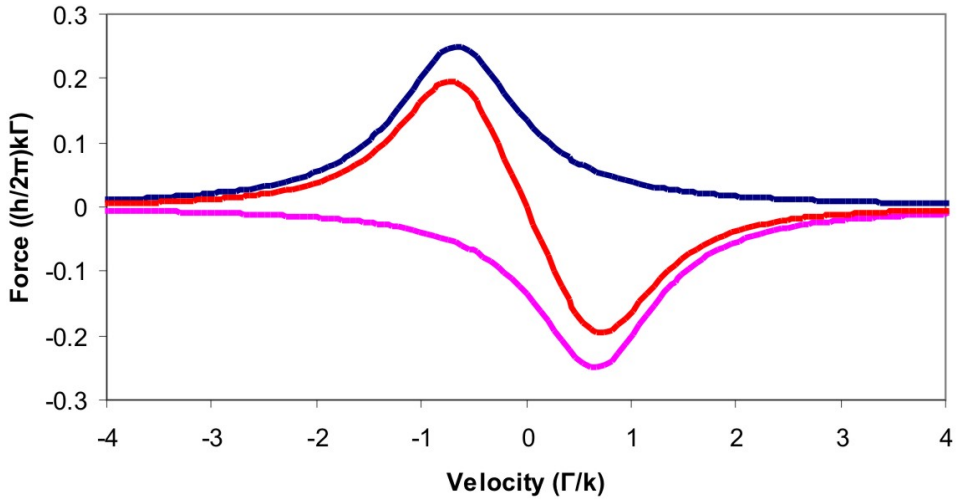

Figure 2.3: Force on atoms as a function of velocity. The top and bottom curves represent the force from each laser while the curve in the middle is the combined result. The 'sweet spot' is with a detuning of half a linewidth. If the detuning was greater, we would see the two curved move further apart and the resulting slope would become shallower, resulting in a smaller force acting on the atoms. Conversely, if the detuning was smaller, the slope would get steeper and eventually disappear as the detuning approached zero.

The result of this is that for $\delta < 0$ the force is damping, for $\delta > 0$ the force is anti-damping and is linear in v if $|kv| << |\delta|$ or $|kv| << |\Gamma|$, as shown in Fig. 2.3.

This can be extended into two and three dimensions, with a 3D molasses being one of the key concepts behind a magneto optic trap (MOT). Optical molasses cannot trap atoms - they will simply diffuse out of the cooling region over time.

The Doppler temperature limit is given by

$$k_{\mathrm{B}} T_{\mathrm{D}} = \frac{\hbar \Gamma}{2}, \tag{2.10}$$

where k_{B} is Boltzmann's constant and T_{D} is the Doppler temperature.

TThe Doppler temperature of the main cooling transition in calcium is $\sim 841 \mu$K,

whereas for the ${}^1S_0 - {}^3P_1$ intercombination line has a Doppler temperature of only ~ 9 nK. The reason for this temperature limit - the reason why this wont just cool to zero is that there is some heating effect taking place here. As stated earlier, the momentum kicks received by the atom from emitted photons is random so averages out to zero over many repetitions. This is not strictly true, as the atom will undergo a random walk due to these kicks and will not return to exactly the same position. This means the atom will always have some velocity and so, some temperature.

In a molasses, the velocity damping time constant - the time taken for at atom in the molasses region to be significantly slowed - is given by [8]

$$\tau_\nu = \frac{M}{\alpha}, \tag{2.11}$$

where M is the atomic mass and α is known as the damping coefficient and is given by [8]

$$\alpha = -4\hbar k^2 \frac{I}{Is} \frac{(2\Delta/\Gamma)}{[1 + (2\Delta/\Gamma)^2]^2}. \tag{2.12}$$

2.2.3 Magneto Optic Trap

By addition of a magnetic gradient to a 3D optical molasses atoms can be slowed and trapped. It is for this reason the setup is known as a **magneto-optical** trap [7].

The quadrupole magnetic field is created by use of two coils in anti-Helmholtz configuration (that is, with current flowing in opposite directions) on either side of the desired trapping region. The quadrupole magnetic field with zero magnetic field at the trap centre serves to impart an increasing Zeeman shift to the magnetic sub-states as the atoms drift away from trap centre.

Consider an atom with ground state $J_g = 0$ and excited state $J_e = 1$ with sub-states $m = -1, 0, +1$. The three possible transitions under these conditions

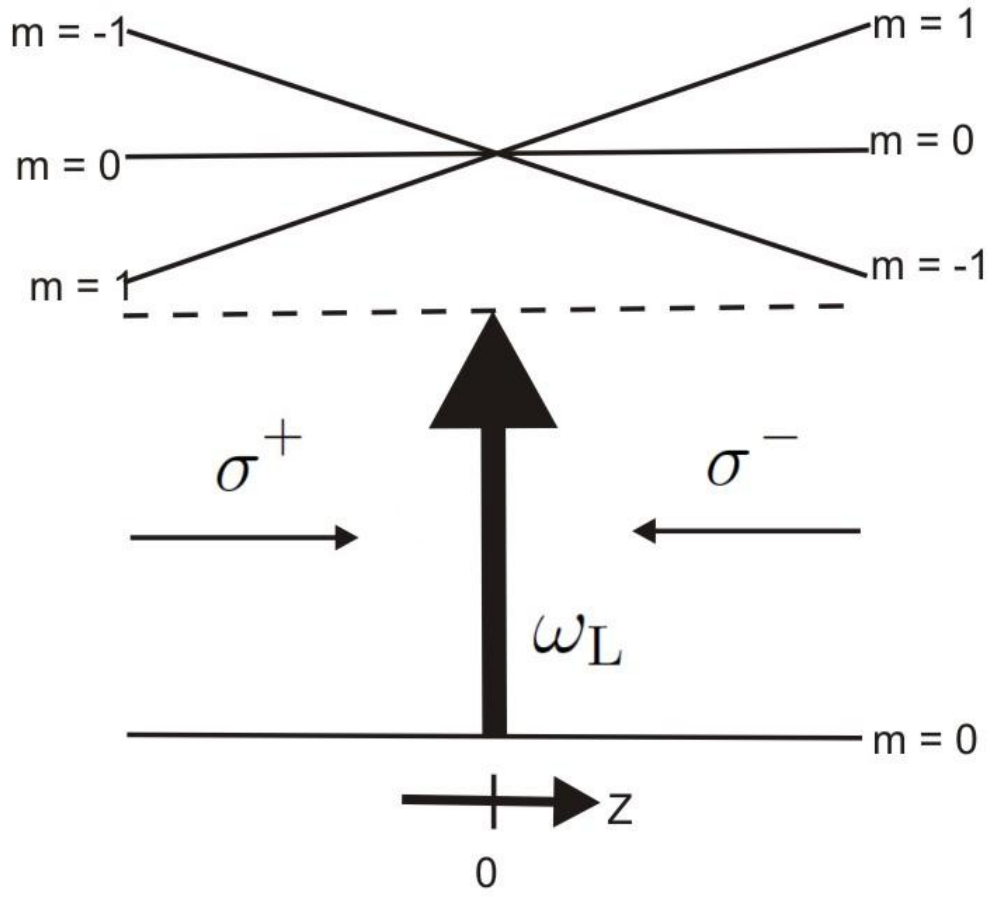

Figure 2.4: A 1D MOT example. The different circular polarisations see different transitions closer to resonance.

are $|J_g = 0, m_g = 0\rangle$ to $|J_e = 1, m_e = -1, 0, +1\rangle$ driven by σ^-, π and σ^+ polarised light respectively (in the lab frame of reference).

The 3 pairs of counter propagating laser beams that form the trapping region are of opposite circular polarisation. As a result, in the spatially varying magnetic field supplied by the anti-Helmholtz coils, for an atom in the +ve z-direction, the σ^- beam sees the $\Delta m = -1$ transition shifted into resonance with it, thus pushing the atom back towards the trap centre. The same is true for an atom in the -ve z-direction, using the σ^+ beam and the $\Delta m = +1$ transition [16]. This result in the atoms experiencing a position dependent force that increases with distance from the trap centre. This can be seen in Fig. 2.4 for the 1D case.

This diagram describes the situation when calcium atoms as laser cooled ex-

actly, due to the fact that there is no ground state splitting. The 3D generalisation can be seen in Fig. 2.5. To control the polarisations of the MOT beams there are quarter waveplates installed both before the MOT chamber and after the MOT chamber, but before the retro-reflecting mirrors. It should be noted that due to the directions of the magnetic field, the polarisations in the 'vertical' direction on this image should always be opposite to those in the 'horizontal' directions.

The result of this setup is that any atom drifting away from the centre of the trapping region is pushed back towards trap center by one of the laser beams. This allows atoms to be confined in all directions and held in the trapping region. This happens as a result of the combination of the damping force of the molasses, which slows the atoms and the spatially dependant force exerted by the combination of the MOT laser beams and the MOT magnetic coils which act as a restoring force, pushing the atoms back into the magnetic field minimum.

2.3 Atomic Structure

Due to the Pauli exclusion principle no two electrons can have identical quantum numbers, resulting in electrons filling up sequential shells. For our purposes, only electrons in the outer, unfilled energy shells are of importance. In the presence of an external magnetic field states with a different magnetic quantum number $\mathrm{m}_J(\mathrm{m}_J = -J, -J+1, ..., J)$ will experience a splitting due to the Zeeman effect, with the magnitude of the splitting between sequential quantum numbered states being given by

$$\Delta E = g_J \mu_B B_0, \tag{2.13}$$

where μ_B is the Bohr magneton.

In LS coupling, there are only certain transitions that are allowed. These dipole transitions are governed by the selection rules, which state $\Delta S = 0$, $\Delta L = \pm 1$, $\Delta J = 0, \pm 1$. This is not *strictly* true, however. Transitions that break the selection rules do happen, but are extremely weak. These transitions are known as

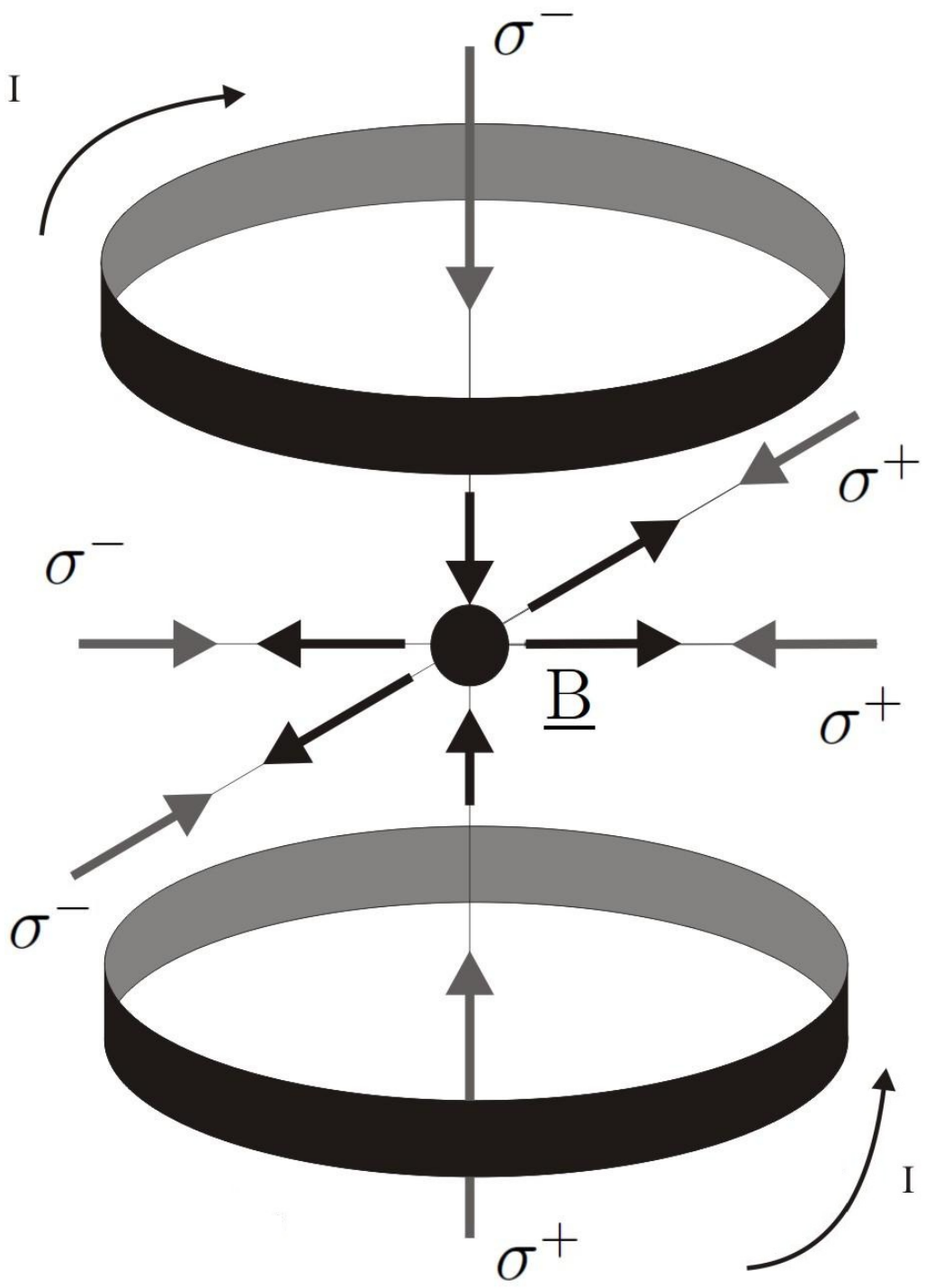

Figure 2.5: 3D generalisation of a MOT with 3 pairs of orthogonal $\sigma^+\sigma^-$ beams and anti-Helmholtz coils. Also shown is the direction of increasing magnetic field.

forbidden transitions. An example of a forbidden transition would be any transition between an S and a D state, which, as S states have a L of 0 and D states have an L of 2 would break the $\Delta L = \pm 1$ selection rule. One type of forbidden transition that is of particular import in this work occurs between singlet and triplet energy levels. These transitions are allowed due to inaccuracies of the LS coupling desription whereby the spin-orbit interactions mixes some singlet and triplet wavefunctions together. This results in the very weak transitions known as *intercombination lines*. Compare, for example, the linewidths of the main cooling transition in calcium and one of the intercombination lines used. The main cooling transition linewidth is $35MHz$ and the corresponding intercombination line linewidth is $\sim 370Hz$. It should be noted that the only difference between the $4s^2\,{}^1S_0 - 4s4p\,{}^1P_1$ transition and the $4s^2\,{}^1S_0 - 4s4p\,{}^3P_1$ transition is that there is a difference in spin between the two. Everything else is identical. In this case, it is the $\Delta S = 0$ selection rule which is being broken.

2.4 Calcium Structure

Calcium is an alkaline-earth element, as opposed to the workhorse element used in laser cooling experiments, rubidium, which is an alkaline-metal element. The alkaline-earths belong in group II of the periodic table and thus are two electron systems: there are two free electrons orbiting the nucleus. The atomic structure is, therefore, more complex than group I elements like rubidium, which feature a single electron orbiting the nucleus. Calcium is a relatively soft and reactive metal with a metallic silver colouration, but readily oxidises when exposed to atmosphere and reacts aggressively when introduced to water [53]. It has a melting point of $1113K$ and boils at $1753K$ [54].

The electronic ground state of calcium is

$$1s^2 2s^2 2p^6 3s^2 3p^6 4s^2 \quad {}^1S_0. \tag{2.14}$$

The main cooling transition of calcium is the $4s^2\,{}^1S_0 - 4s4p\,{}^1P_1$ at 423 nm. This transition is perfect for laser cooling because it has a large linewidth of $\sim$

35 MHz. Also unlike, for example, rubidium, the ground state has no nuclear spin. This lack of nuclear spin has benefits and drawbacks. Due to the lack of hyperfine structure of the ground state (as a result of their being no nuclear spin), a benefit is that only one laser is needed to produce a MOT. With laser cooling elements with ground state hyperfine structure, a second 'repump' laser is required to stop cooled atoms leaking out of the system into one of the hyperfine sublevels. While that particular leak is removed when dealing with an element like calcium, others are introduced. From the main cooling cycle excited state, $4s4p\,^1P_1$, $\sim 1:10^5$ atoms will decay into the $4s3d\,^1D_2$ state [55]. From there, the atoms will then decay into the $4s4p\,^3P_2$ and $4s4p\,^3P_1$ levels with a branching ratio of 1 : 5, respectively [56]. Atoms that decay into the $4s4p\,^3P_1$ level rejoin the cooling cycle in $\sim$400 μs. However, atoms which decay into the $4s4p\,^3P_2$ level, which has a lifetime of $\sim$ 118 minutes [57], are effectively lost from the system as they diffuse out of the trapping region. This represents the main loss from the system.

The main drawback of this lack of nuclear spin is that, due to the same lack of hyperfine sublevels of the ground state that helps us elsewhere, it is not possible to use standard techniques such as magnetic trapping for evaporative cooling [12] or polarisation gradient/Sisyphus cooling [9] to cool beyond the Doppler temperature limit and on to Bose-Einstein condensate (BEC). While other methods exist for attaining sub-Doppler cooling and attaining BEC in calcium [33, 58], these methods do not feature in this work.

For this work, it is important to point out that there are several isotopes (atoms with the same number of protons but differing numbers of neutrons and so slightly different masses) of calcium. The primary isotope used in this work is ^{40}Ca, as it is the most naturally abundant isotope. Other isotopes of interest are ^{41,42,43,44,46,48}Ca. The even isotopes all have no nuclear spin and hence no ground state splitting, but the odd isotopes have spin of 7/2.

The energy levels and transitions relevant to this work, along with state lifetimes and transition wavelengths are shown in Fig. 2.6

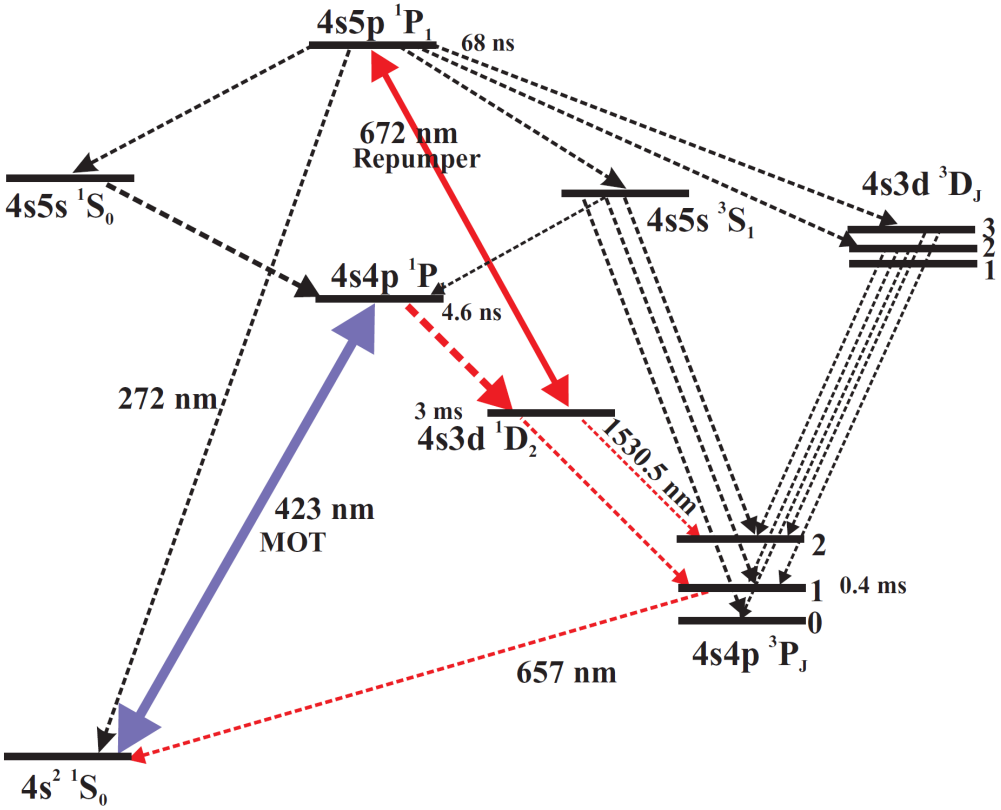

Figure 2.6: Atomic energy level transitions in calcium. Included are vacuum wavelengths and excited state lifetimes for relevant transitions. The main cooling transition is the $4s^2\ ^1S_0 - 4s4p\ ^1P_1$ at 423 nm.

2.5 Lasers required

423 nm is not the easiest wavelength at which to find a laser with sufficient power. Unlike rubidium, for example, this cooling transition is not easily accessible with commercially available laser diodes (the rubidium transitions are at ∼780 nm, very close to the operation wavelength of CD player laser diodes). While it is possible to tune the emission wavelength of a diode by altering the temperature (higher temperatures increase the wavelength, lower temperatures decrease it), a rule of thumb for NIR laser diodes is that it takes a temperature change of ∼ 3°C to produce a wavelength change of 1 nm [59]. This means that if, for example, a Blu-Ray diode with room temperature wavelength of ∼405 nm were to be used, it would need to be heated up to ∼ 74°C to get to the desired wavelength. However,

Blu-Ray diodes actually tune much more slowly, at a rate of $\sim 25°C/nm$ Thus to get to a suitable wavelength would require heating to nearly 500°C. It is possible to buy diodes at 423 nm (Toptica LD-0425-0120-1) claiming 120 mW output power from a free running diode, but only 13 mW from an external cavity diode laser. This is far too little power, as will be highlighted later.

The solution is second harmonic generation (SHG). Before this step, however, a source of a large amount of power at double the required wavelength is needed. The obvious solution is a titanium-sapphire (Ti:S) laser [60]. Ti:S lasers are extremely useful pieces of equipment due a number of reasons. They are wavelength tunable over a very broad range (as much as 650nm to 1100nm if mirror sets are changed, with peak efficiency being at a lasing wavelength of ∼800 nm), they produce a stable TEM00 mode beam (a gaussian beam) of good quality and powers in the Watt regime. Pumped with 7W of 532 nm light from a frequency doubled 1064 nm $Nd : YVO_4$ laser (Coherent Verdi V8), the Ti:S used for this work produced somewhere in the region of 500 - 600 mW (sometimes as much as 750mW) of power at 846nm. In order to generate the second harmonic of this wavelength and thus produce the 423 nm light necessary for the experiment, it was passed through a 10 mm crystal of periodically poled potassium titanial phosphate [61] (ppKTP) (periodic poling is a process which enables quasi-phase matching of nonlinear interactions in a transparent crystal material [62]) with a poling period of 4μm. The reason such a high power is necessary is that the SHG efficiency of such a crystal at this wavelength is on the order of 0.3%/W, leading to ∼1.5 mW of blue light from a single pass through the crystal. This 1.5 mW is used later to lock the laser to the desired atomic transition of calcium and another crystal is used to generate the ∼100 mW in an enhancement cavity, which will be explained in detail later in this chapter.

2.5.1 Locking setup

In order to successfully cool and trap atoms consistently the source of cooling light must be on and stay on resonance with the atomic transition in question. While Ti:S lasers are stable, they are not stable enough, especially when the necessary frequency doubling is taken into account. Any change in the frequency

of the Ti:S laser is doubled for the generated blue light. Fort this reason, it is necessary to 'lock' the laser to the $4s^2\ ^1S_0 - 4s4p\ ^1P_1$ transition at 423nm. This is done by way of a saturated absorption spectroscopy (SAS) setup.

The setup used is described in great detail in [49] and is merely summarised here. About 1.5 mW of 423 nm light, derived from a Ti:S laser emitting 846 nm light on a single pass through a ppKTP SH generating crystal heated to $\sim 70°$C is directed towards an AOM (Crystal Technologies 3080-125, centre frequency 80MHz). The zero and +1 orders from the AOM, which form the pump beams, are directed via independently adjustable mirrors towards and overlapped inside a hollow cathode calcium lamp (Hamamatsu L2783-20NE-Ca). At the same time, a probe beam (which propagates in the opposite direction to the pump beams), picked off before the AOM and with a power of $\sim 150\mu$W is also overlapped with the two pump beams. This probe beam is then picked up on an AC coupled, amplified photodiode. As the AOM is amplitude modulated (on/off) at 55 kHz, phase sensitive detection (using a lock-in amplifier) of the probe beam produces two saturated absorption signals that are 180° out of phase and separated by half the AOM frequency. Adding these two signals together produces a standard error signal with a strong zero crossing approximately a quarter of the AOM frequency below the atomic transition frequency. The setup is shown in Fig. 2.7

The signals from each pump beam separately and the combination are shown in Fig. 2.8. The power of each pump beam was generally between 0.7 mW and 1 mW and the power of the probe beam was $\sim 300\ \mu$W.

It is worthy of note that this setup is sensitive enough to pick up isotopes with $< 0.2\%$ natural abundance (^{48}Ca). ^{40}Ca, the isotope used for this work, has a natural abundance approaching 97%. Again, this is explained in greater detail in [49, 50]. The traces seen above are not always exactly reproducible. Oftentimes one or the other of the individual absorption signals would have a different amplitude to the other. This was acceptable, however, as it was still possible to produce a stable lock in these conditions provided there was a strong zero crossing. The lamp was typically run at 480 V, 8.07 A, but these parameters could be increased or decreased as necessary for the best signal.

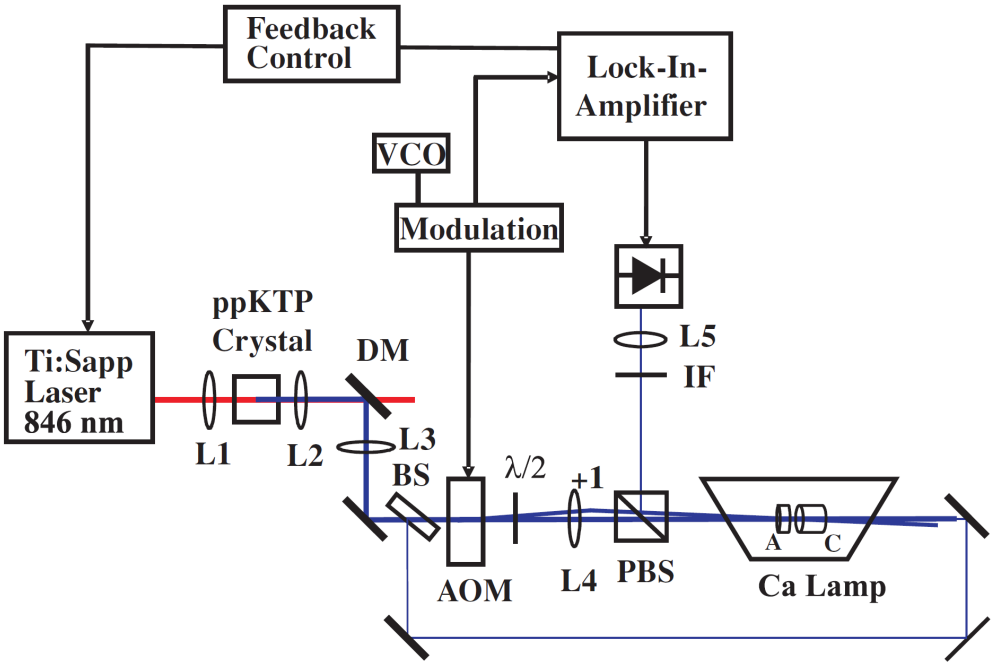

Figure 2.7: Experimental setup for amplitude-modulation saturated absorption spectroscopy of calcium. Linear $\perp$ linear polarization is used for the pump and probe beams. The pump beams are amplitude modulated by an AOM. The signal is detected with a photodiode amplifier. In the setup, dichroic mirror (DM), beam sampler (BS), half-wave plate ($\lambda/2$), polarizing beam splitter (PBS), interference filter (IF), and L1, L2, L3, L4 and L5 are lenses, respectively [49].

2.5.2 Doubling cavity

As stated in an earlier section of this chapter, a minimum of ∼100 mW of light at 423 nm is needed for to run the experiment. To generate this power, the infra-red (IR) light not converted into blue light in the previously mentioned ppKTP crystal is directed through a polarisation maintaining optical fiber to the lab's second laser table, which houses the experiment proper. The $60 - 70\%$ of the light that is successfully coupled through the fiber is directed into an enhancement cavity in bow-tie configuration, which contains an identical ppKTP crystal. The reason ppKTP is used is because, compared to other doubling crystals, the efficiency of 0.3%/W is high. This means factors such as the impedance matching do not need to be perfect for it to work. Other doubling crystals tend to be, at best, half as

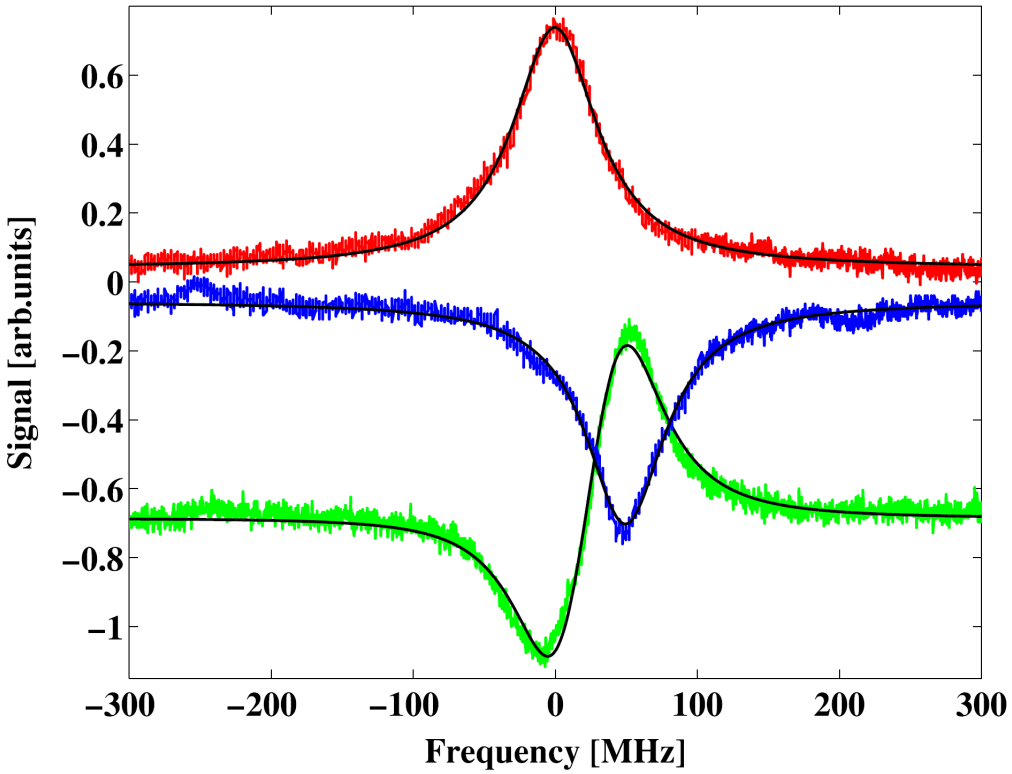

Figure 2.8: The red (top) curve shows the signal due to the zeroth order pump beam, the blue (middle) shows the signal due to the first order pump beam. The locking signal when these are combined is shown by the green (bottom) curve, which is offset for clarity and multiplied by -1. Adapted from [49].

efficient. The cavity design is shown in Fig. 2.9

The mirrors are all HR coated at 846 nm (apart from M1 which has a reflectivity of 0.95) and AR coated for 423 nm and the ppKTP crystal is housed in an oven controlled by a temperature controller (Wavelength electronics MPT-5000) and mounted on a vertical translation stage to allow the position of the crystal at the focus between the two curved mirrors to be optimised.

$\sim 350mW$ of 846 nm light enters the cavity via M1 and, if the cavity is mode matched (where the incoming beam mode matches up with the allowed cavity mode such that only one longitudinal and one transverse mode are excited) and impedance matched (when the losses due to the input coupler and the cavity round trip are matched), circulates in the cavity building up power with each

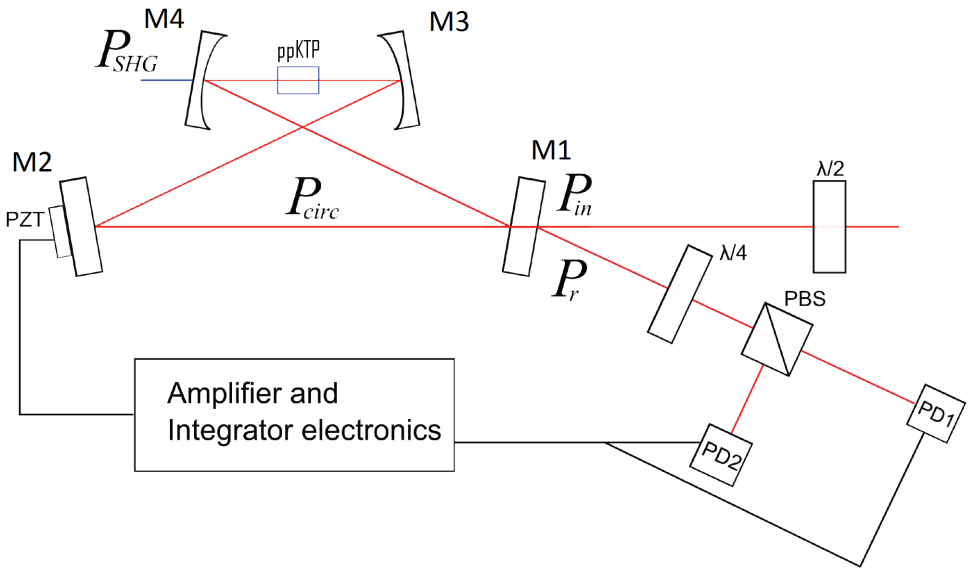

Figure 2.9: The resonant enhancement cavity in bow-tie configuration. M1 and M2 are plane mirrors, M3 and M4 are curved mirrors with radius of curvature (ROC) of $50mm$. P_{in}, P_r, P_{circ} and P_{SHG} are the input, reflected, circulating and SHG powers, respectively. PZT is a piezo electric transducer, $\Lambda/2$ and $\Lambda/4$ are half and quarter wave plates respectively, PBS is a polarising beam splitter cube and PD1 and PD2 are photodiodes.

round trip. More detail can be found in [50].

In order to produce a stable, constant power level, the cavity had to be locked so that the cavity length was always resonant with the desired beam mode. For this, use was made of the Hänsch-Couillaud locking technique [63] whereby the light reflected from the cavity when not on resonance is passed through a quarter wave plate and a polarising beam splitter (PBS). The different polarisations are then directed into separate photodiodes with the signals being added together to give a standard error signal which was then fed to an integrator circuit driving a piezoelectric transducer (PZT) upon which the cavity mirror M2 is mounted. This allows the length of the cavity to be precisely, electronically controlled to always keep the cavity on resonance. This sort of cavity lock, which involves phase sensitive detection, requires the signal be amplitude modulated at a certain frequency with the same frequency used as a reference for a phase sensitive

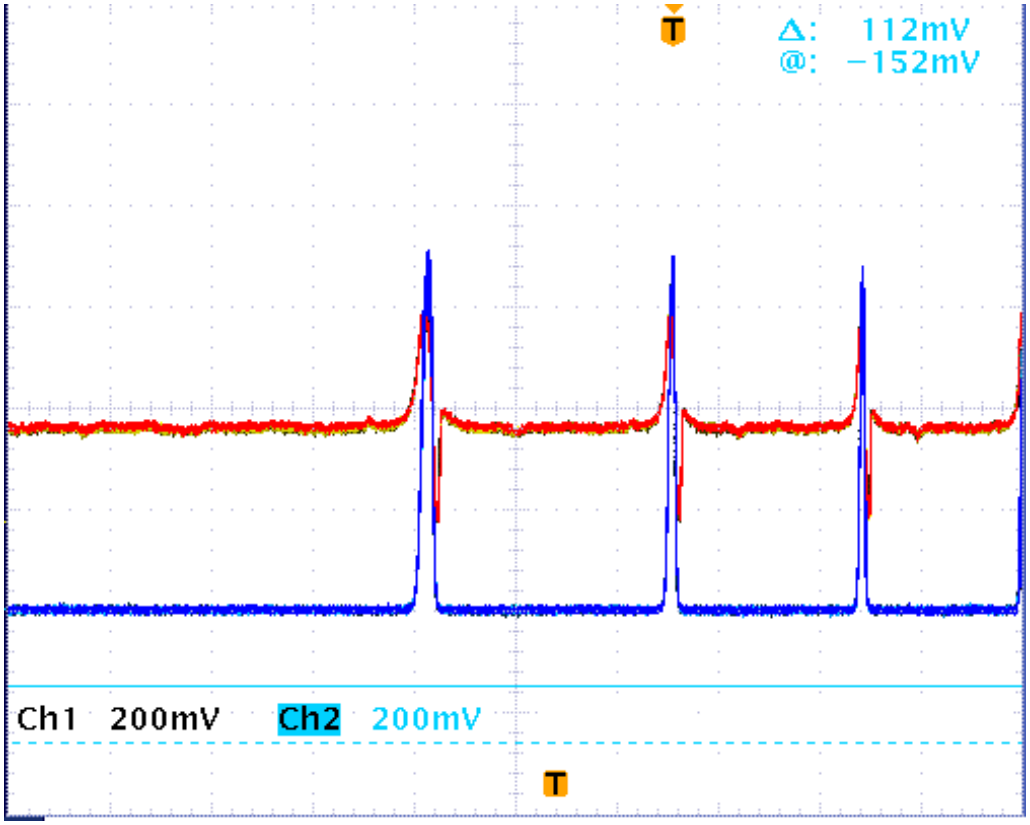

Figure 2.10: The ideal lock signal from the cavity (red) and the blue light generated by the cavity (blue).

detector (like a lock-in amplifier) to enable it to pick out a signal that can be locked to. The beauty of this setup is that the different reflections from the cavity are out of phase with each other and when passed though the PBS, each will hit its photodiode out of phase with the other. When added together, these signals provide a standard dispersion signal which can be locked to simply by using an integrator. This means that the combination of different beam polarisations act as this setups own phase sensitive detector.

Ideally, the lock signals should look those seen in Fig. 2.10

However, it was frequently the case that this signal was unobtainable in practise. Whether due to gradual deterioration in the crystal and/or beam alignment that was nontrivial to correct it is unclear, but the actual locking signal was regularly as shown in Fig. 2.11

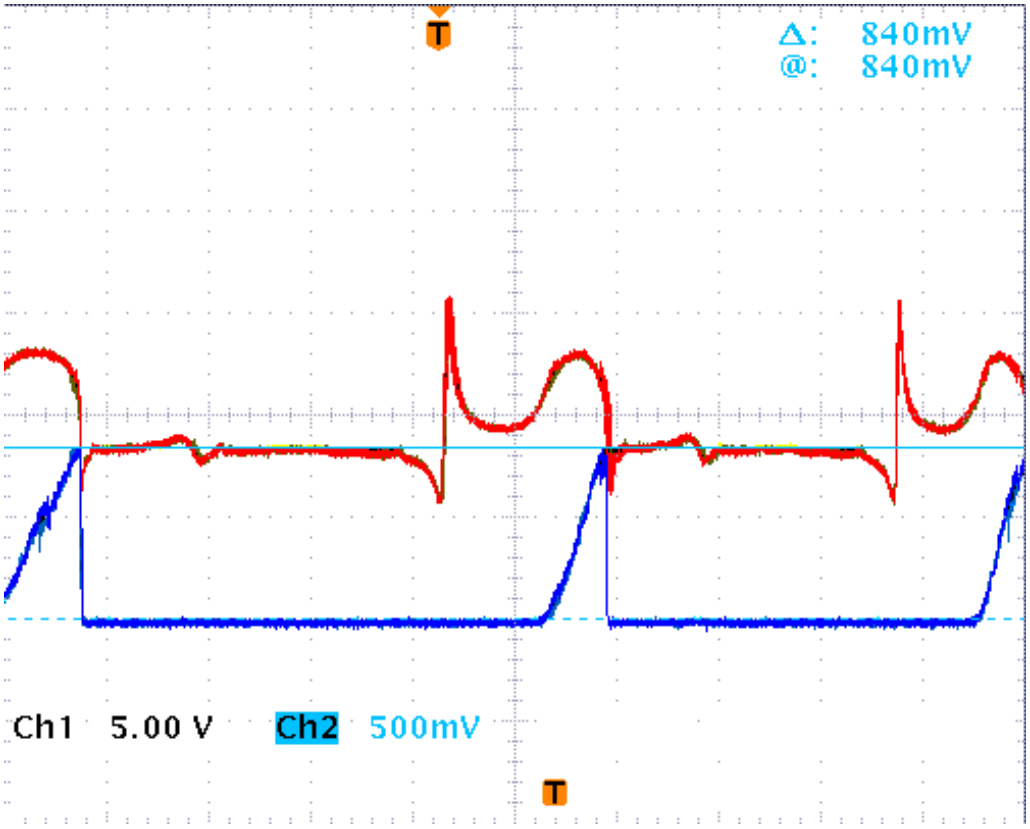

Figure 2.11: The lock signal from the cavity (red) and the blue light generated by the cavity (blue).

While not ideal, it was still possible to lock to this signal with ease. The lopsidedness of the blue light signal (and by extension the right hand side of the double error signal) can be attributed to thermal effects, with the crystal heating up as the second harmonic is generated, the left hand side of the double error signal remains a mystery. It is likely this is simply due to an alignment issue there was not time (nor justification as a lock was still possible) to rectify.

For an input power of ∼350 mW of 846 nm light this cavity, when optimised, produces up to 150 mW (typically 100 - 120 mW) of 423 nm light. Over time this can degrade to less than 100 mW, requiring the cavity be maintained. Of this power, typically 40 - 45 mW was used for the MOT beams (an average of 13.5 mW in each beam) and another 40 - 60 mW were split between the Zeeman slower beam and the 2D molasses beam. The rest of the power is lost in various

optical components along the way (PBSs, AOMs, etc.).

2.6 Hardware

2.6.1 Vacuum setup

In order to produce a MOT worth studying (i.e. with a suitable number of atoms and with sufficient lifetime), the setup needs to be run at a pressure of $\sim 10^{-8}$ mbar. This is achieved in three steps, with a fourth needed only occasionally, as shown in Fig. 2.12. First a standard rotary roughing pump (Edwards model RV12) brings the pressure down to $\sim 10^{-3}$ mbar, followed by a water cooled turbomolecular pump (Edwards model nEXT240D). Both of these pumps are located on the oven side of the pneumatic valve. The nEXT240D is bolted on to a CF100 port on the side of the oven housing with the RV12 attached to the exhaust of the nEXT240D. On the other side of the pneumatic valve and connected to the far side of the MOT chamber an ion pump (Varian VacIon Plus 55 Diode ion pump) was mounted. As a rough means of measuring the system pressure, an ion gauge (Kurt Lesker KJL4500) was mounted to the oven housing opposite nEXT240D. However, for a more precise measure of the pressure inside the MOT chamber (at low pressures) a read out of the current from the ion pump could be compared to a pressure/current graph provided by the manufacturer [64]. This leads to a final pressure of $\sim$ mid 10^{-8} mbar.

Problems arose with this setup, however. Over time calcium would build up on the terminals of the ion pump (the older model used, the Varian VacIon Plus 40 Starcell), leading to erroneous current and, therefore, pressure readings which could not be fixed. This left us with no firm idea of what the pressure in the system was. To remedy this, the ion pump was replaced with a different model (the aforementioned VacIon Plus 55 Diode) which can, theoretically, be fixed should the same problem occur and and extra stage of vacuum technology was implemented between the MOT chamber and the ion pump. A titanium sublimation pump (TSP)(Varian 916-0050) was placed before the ion pump with the ion pump placed out of the direct line of sight of the MOT chamber. When the TSP pump is periodically 'fired', it coats the pipe in which it is placed with

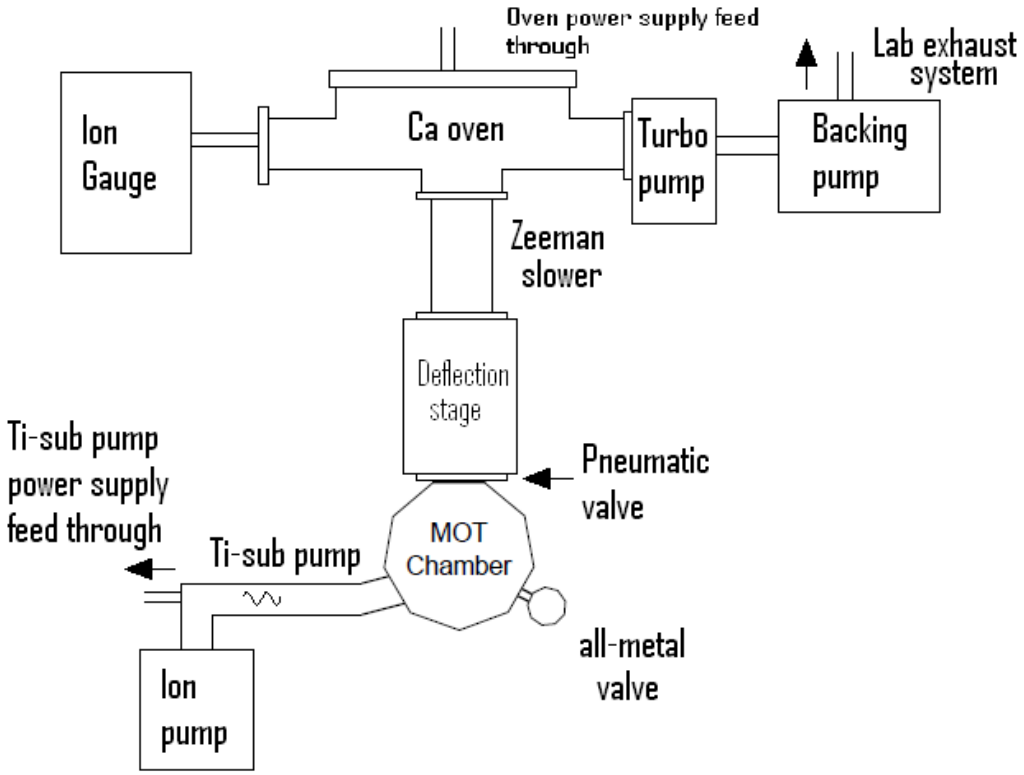

Figure 2.12: The vacuum setup.

titanium, which attracts and traps any stray calcium atoms heading towards the ion pump. The setup is shown in Fig. 2.12 and Fig.2.13

2.6.2 Calcium Oven

Calcium is a solid at room temperature. In order to get a sufficient vapour pressure from a collection of granulated calcium lumps, they must be heated. Vapour pressure is the pressure of a vapour in equilibrium with its solid and liquid phases and is a measure of the number of atoms released from a solid as it is heated [50]. It is given by [65]

$$log_{10}P = 5.006 + a + \frac{b}{T} + (c * log_{10}T), \tag{2.15}$$

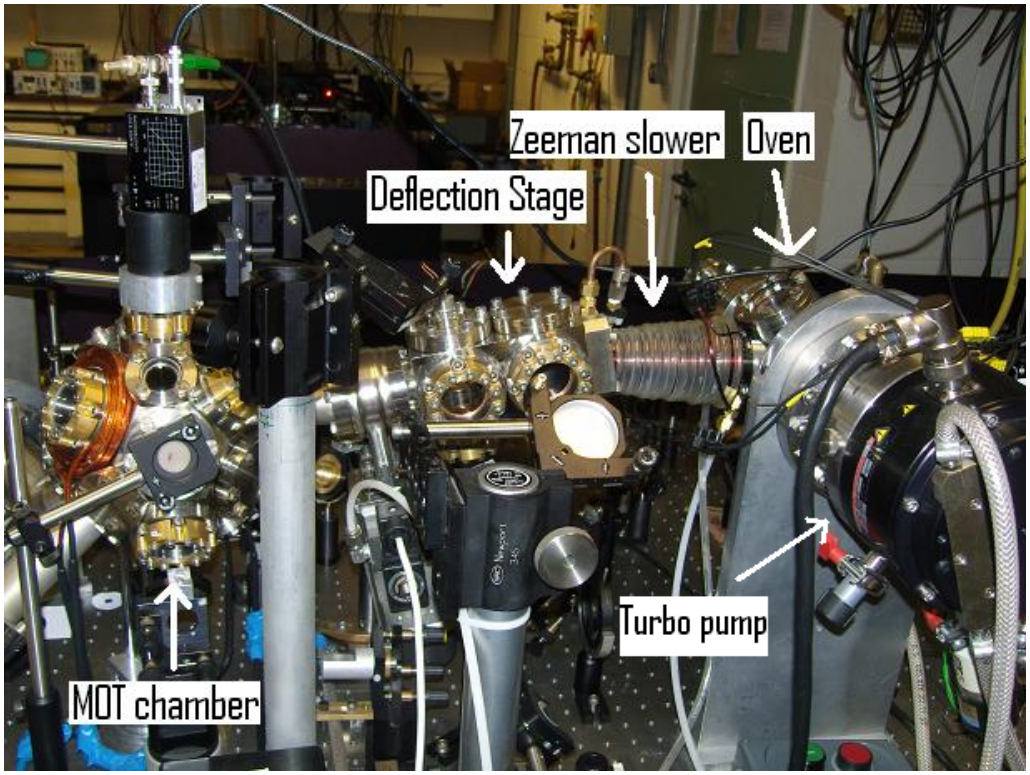

Figure 2.13: A photograph of the vacuum setup. It should be noted that in this picture, the turbo pump is not the nEXT240D, but an older Edwards 250l/s turbomolecular pump that failed around the time the TSP pump was added in late 2009.

where P is the vapour pressure in mPa, $a = 10.127, b = -9517, c = -1.4030$ are constants found in the literature [54] and T is the temperature of the metal in Kelvin.

The temperatures needed for sufficient vapour pressure can be seen in Fig. 2.14

In this case, for the necessary vapour pressure of 10 mPa, a temperature of nearly 800 K is necessary. As a result, one of the main considerations when constructing the oven was that it be made of material capable of withstanding said high temperatures. The other main consideration was that the atomic beam directed towards the eventual trapping region be reasonably well collimated [66]. The design of the oven is shown in Fig. 2.15

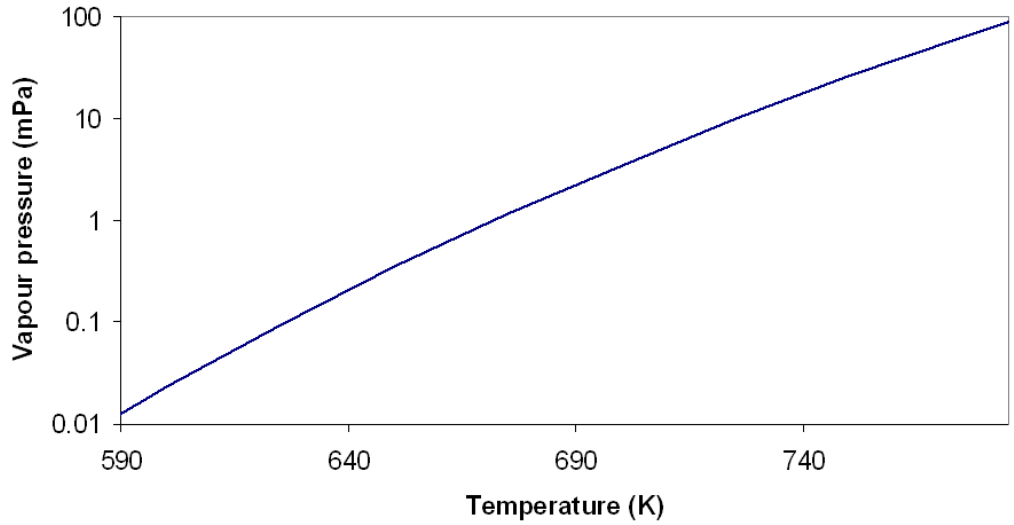

Figure 2.14: The vapour pressure versus temperature curve for calcium.

The oven is made of two stainless steel capsules inside two cylindrical copper mounts with coaxial heater wires (Thermocoax) wound into grooves on the exterior and is designed to carry heat uniformly to the calcium granules within (99.99% pure caclium, Sigma-Aldrich 44187-2). The copper cylinders are held in place by two stainless steel mounting cylinders which make minimal thermal contact with the heater wires. The front and rear ends of the oven are heated independently of one another and the individual temperatures are measured by K-type thermocouples.

If a mean atom velocity of $\bar{\nu}$ with number density per unit volume n is assumed, the number of atoms $dQdt$ emerging into a solid angle $d\omega$ through a cross section A_s in time dt is given by [65]

$$dQdt = \frac{d\omega}{4\pi} n(\bar{\nu} dt A_s cos\theta). \tag{2.16}$$

If these atoms exit into a cylinder of length l and radius r and diameter d, it will collimate the beam of atoms as only atoms that enter the cylinder with a path with angle less than θ_{max} relative to the centre of the cylinder will pass through

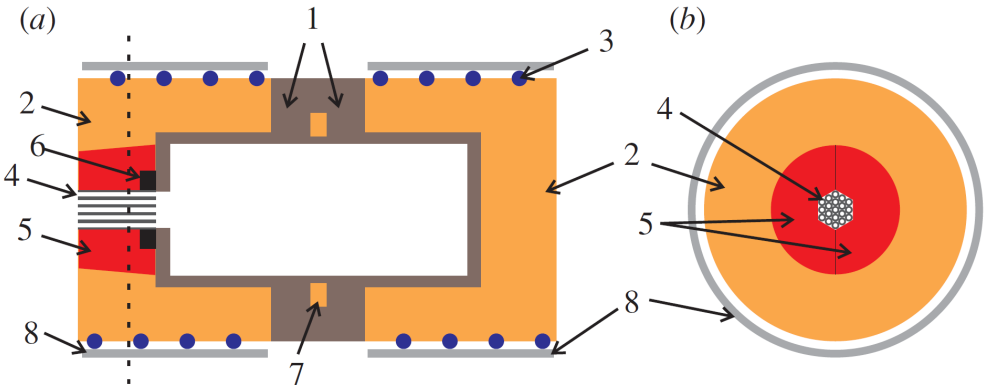

Figure 2.15: Cross-sections of the Ca oven. A stainless steel capsule (1) contains the Ca metal and is surrounded by a copper shell(2) heated by coaxial heaters (3). Nineteen stainless steel capillaries (4) collimate the beam. The capillaries have a $0.5mm$ inner diameter, are $10mm$ long and are held in place by two copper pieces (5) forming a hexagonal hole in the middle and a conical outer surface. Once assembled this unit is pressed into a matching cone formed in one of the copper shells. A stainless steel disk (6) with a hexagonal hole in the middle restricts the access of the hot calcium to the surrounding copper. Similarly, the design of the stainless steel capsules restricts the access of the calcium to the copper gasket (7), which seals the oven. Two stainless steel tubes (8) hold the heaters tightly against the copper shells and provide some insulation of the oven. (a) Longitudinal cross-section. A transverse cross-section through the oven at the dashed line is shown in (b)[48]

.

it, where $\theta_{max} = tan^{-1}(d/l)$. By integrating this from 0 to θ_{max} and substituting $d\omega = 2\Pi sin\theta d\theta$ the total number of atoms per unit time can then be found to be

$$Q \approx \frac{1}{4} n\bar{\nu} A_s (r/l)^2, \tag{2.17}$$

which, for typical parameters produces a flux of 1 x 10^{13} atoms/second.

To ensure the atoms exiting the oven are well collimated the exit channel from the oven is filled with 19 stainless steel capillaries 10 mm in length with and inner diameter of 0.5 mm in the shape of a hexagon, held in place by copper mounts. In order to avoid these capillaries becoming clogged the front end of the oven is

kept constantly between 10° and 20°C hotter than the back of the oven. Normal operating temperatures for this setup are 490°C at the back and 505°C at the front. The beam emerging from the oven is approximately 4 mm in diameter with a full-angle divergence of less than 6° ($2\theta_{max} = 5.7°$). However, as far as the experiment is concerned the collimation is limited to approximately 2° by the slowing laser beam size.

Assuming a point source of atoms from the oven, the solid angle subtended by one of the capillaries is given by

$$\Omega = \pi \left(r/l\right)^2 , \tag{2.18}$$

where r is the radius of each capillary and l is the length of each capillary.

This gives a solid angle, in our case, of 1.96×10^{-3} sr, leading to a transverse velocity of $\approx 1/20$ (using $V_{\mathrm{T}} = V \sin\theta$) of the longitudinal velocity.

For an oven temperature of 490°C the most probable longitudinal atom velocity is 446 m/s (meaning a transverse velocity of ≈22 m/s). This is too fast to be captured (capture velocity of our system = 60 m/s), therefore these atoms need to be slowed. Enter the Zeeman slower.

2.6.3 Zeeman Slower

The slower has been designed to deliver a beam of slow atoms, with a mean speed of approximately 60 m/s. This is chosen so as to approximately match the capture velocity of our MOT setup, which is 70 m/s [48]. Put simply, atoms which travel faster than the capture velocity of the MOT do not spend long enough in the trapping region to fall into the MOT, and so escape. The slower consists of two coils: a tapered solenoid to follow the decreasing Doppler shift of the slowed atoms, and a fixed width coil designed to interrupt the slowing process and decouple the atoms from the magnetic field. This works because the shape of the field suddenly changes too fast for the atoms to follow it. The slower is

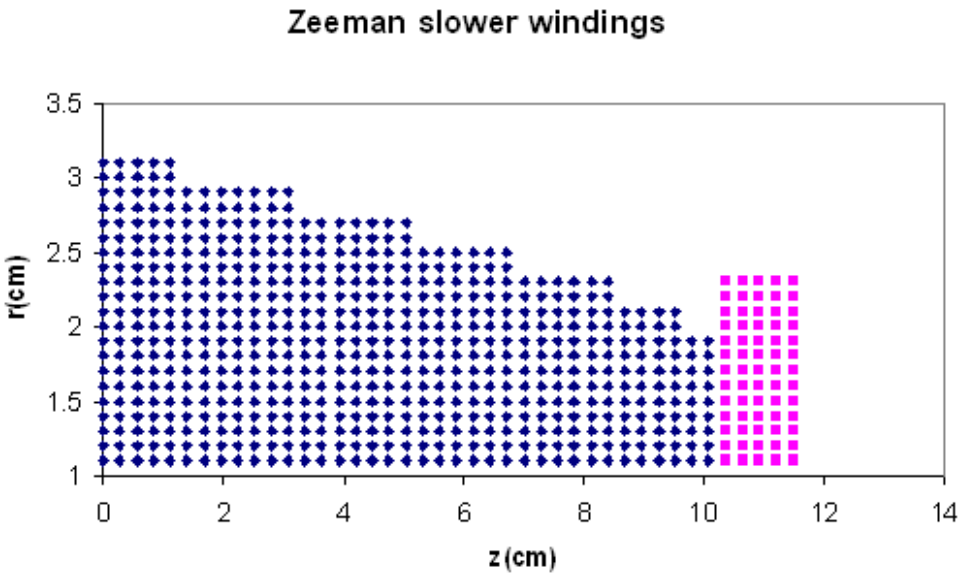

Figure 2.16: A representation of the winding of the magnetic coils for the Zeeman slower. The blue represents the tapered solenoid 'Zeeman coil' and the pink represents the fixed 'end coil'.

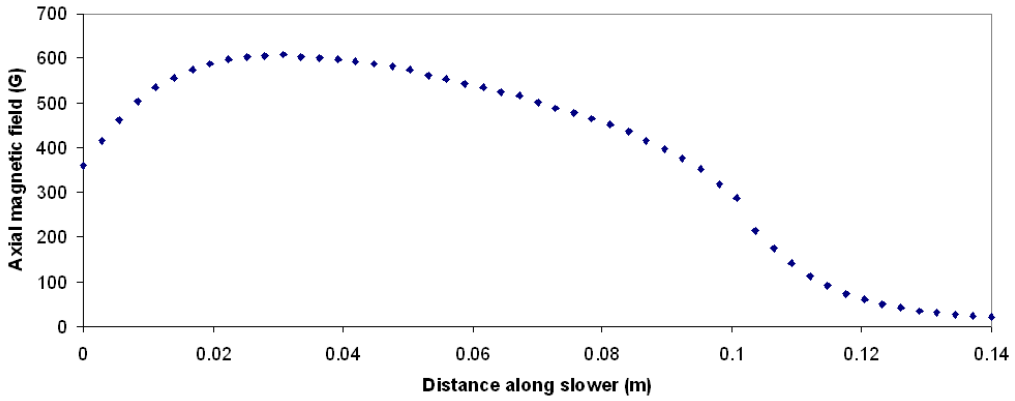

Figure 2.17: The calculated magnetic field produced by the Zeeman coil.

wound from rectangular wire of cross-section 2.8 mm x 1 mm. A representation of the windings is shown in Fig. 2.16

This produces the magnetic field profile shown in Fig. 2.17

The coils are wound around a custom 13 cm long vacuum pipe which is con-

structed to include a channel between the outer and inner diameter for water cooling. Additional water cooling is provided by rubber tubing wrapped around the Zeeman coil. This is necessary as the $\sim 40W$ of power in the coil generates a lot of heat. Without this additional cooling measure, the Zeeman coil would regularly reach temperatures of 50°C.

The total length of the Zeeman slower is $\sim$ 14 cm in length. This is atypically short for a Zeeman slower, as traditional examples can often exceed 1 m in length. The compactness of this design is down to the fact that calcium is much lighter (atomic mass of 40) than, for example, rubidium (atomic mass of 85) and the 423 nm photons are more energetic and so have more momentum to impart than the 780 nm light used for rubidium.

The typical operating parameters of this Zeeman slower are 5V, 9A in the Zeeman coil and 5V, 5A in the end coil. This results in the lower velocity wing of the atoms exiting the oven with a velocity distribution centered around $\sim$ 500m/s being slowed to a mean velocity of $\sim$ 60m/s. If an oven temperature of 490°C is used as an example this corresponds to $\sim$ 19% of the beam flux. The Zeeman slower is typically run with $15 - 20mW$ of power in the slowing beam. The red detuning from resonance was done by extracting the Zeeman slower beam from the +1 order of an acousto-optic modulator (AOM) (Crystal Technologies 3200-120) with center frequency of 200 MHz running at between 180 MHz and 202 MHz.

2.6.4 Deflection stage

As only this 19% of atoms are successfully slowed to $\sim$ 60m/s, it follows that the rest are not adequately slowed. It would be disadvantageous to allow these fast atoms (and the atoms that don't interact with the slowing laser at all) to continue forwards into the rest of the experimental setup. The higher temperature and velocity would reduce the lifetime of the trapped atoms. What is needed is a means of effectively removing them from the experiment. This is done by way of what we have dubbed the deflection stage, which makes use of optical molasses.

In the deflection stage, use is made of a 2D optical molasses. This serves two purposes: first it transversely cools (i.e. collimates) the atoms exiting the Zeeman

slower and it deflects the colder atoms from the Zeeman slower from the path of the remaining hot atoms. The transverse cooling is necessary because the slowing beam from the Zeeman slower only slows the atoms in the longitudinal direction. Only atoms leaving the oven with a transverse velocity low enough such that they can enter the capillary tubes (see the calcium oven section of this chapter). Those atoms will still have some transverse velocity which is of a similar magnitude to the longitudinal velocity, meaning that while we want a steady beam of atoms, what we get is a very diffuse 'spray' of atoms.

The 2D molasses is constructed with a single 14 mm diameter beam with power of up to 20 mW retro-reflected in a figure-of-four mirror configuration placed at an angle of incidence of 22.5° and a retro-reflection mirror. The 14 mm beam diameter is chosen to ensure that the atoms passing through the molasses spend several damping times in the molasses. One damping time, assuming the molasses beams are detuned half a linewidth below resonance and have a power of 10 mW, is $\sim 25\mu s$. From this 25μs damping time, it can be seen that even the fastest atoms of interest (100m/s) spend several damping times in the molasses region. The deflection stage setup is shown in Fig. 2.18

This is known as the deflection stage because it directs the slowed atoms downwards at an angle of 12.9° from the horizontal plane. This happens because, due to the molasses beams intercepting the atoms at an angle, one beam will always interact with the atoms more strongly than the other as the atoms are already heading more towards it than the other.

The deflection stage is constructed from a rectangular stainless steel block of dimensions 70x70x150 mm with 10 conflat ports. Four of these ports house anti-reflection (AR) coated windows (One for the molasses beam, one for the Zeeman slower beam and two left for visual access). One port on the bottom is used for the Zeeman slower beam which is reflected off a silver coated mirror inside the vacuum at and angle of $\sim 40°$. One issue with this design is that, over time, the atoms which are traveling too fast after exiting the Zeeman slower and are thus not deflected by the 2D molasses will carry straight on and start to coat this mirror. This leads to a dramatic drop in the efficiency of the Zeeman slower and thus, the MOT as a whole. To combat this, a resistive heater was built into the mount for the mirror with electrical access via a conflat port on top of the

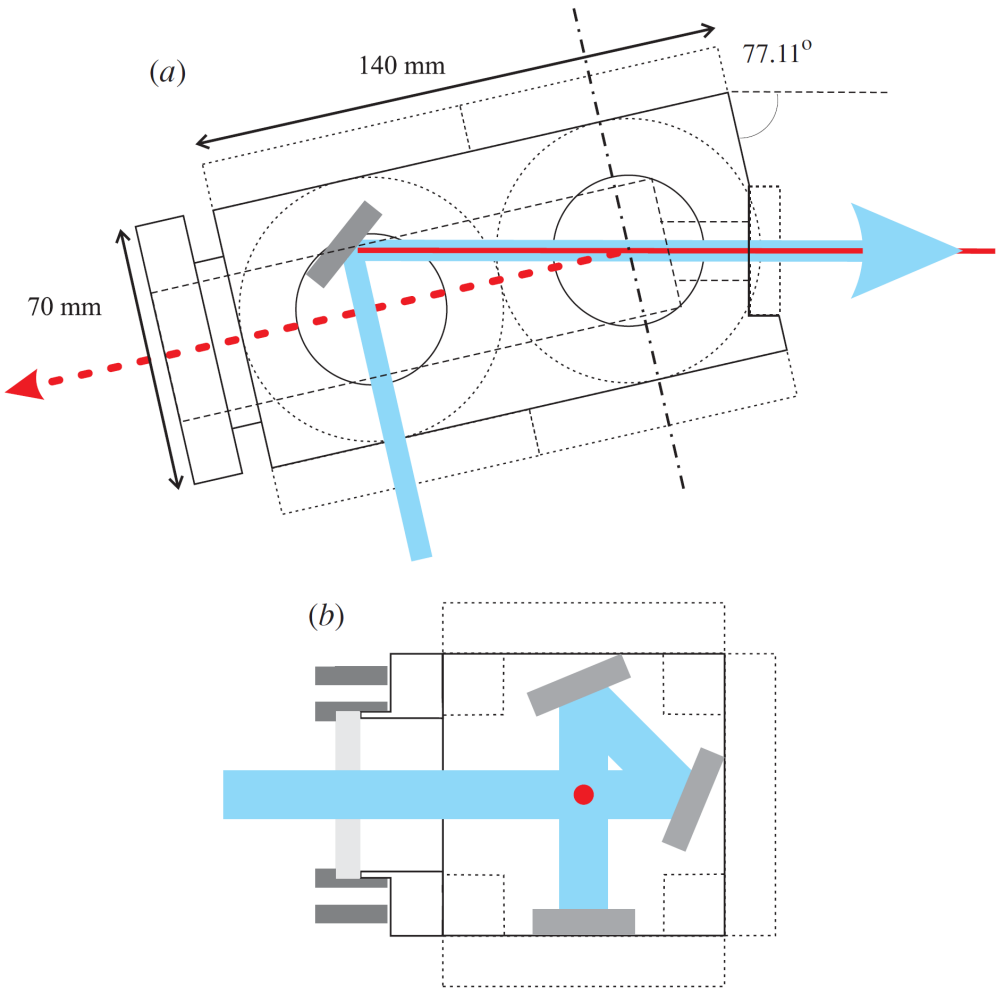

Figure 2.18: Schematic diagram of the deflection stage, which is mounted directly on the end of the Zeeman slower. (a) Longitudinal section. The atomic beam enters from the right and is overlapped with the slowing beam, which enters from the bottom and is reflected off a mirror inside the vacuum. The transverse molasses deflects slowed atoms along the dotted line. It is not shown in this view but implemented in a plane along the dash-dotted line. (b) shows the cross-section along this line and the figure-of-four path, the light follows to provide the two orthogonal standing waves for the transverse cooling. For clarity, the vacuum flanges and windows are only indicated with faint dashed lines apart from the window in (b) showing the lead-seal vacuum viewport design [67].

deflection stage. It was found that running this heater for several hours (> 12) at 12V and 2A initially increased the overall pressure of the system, indicating that the calcium atoms which had accumulated on the mirror were being removed from it. The pressure would return to normal thereafter and the MOT would improve.

The ports on either end of the deflection stage serve as a path for the atom from the Zeeman slower to the MOT chamber. The remaining ports are simply blocked with flanges. It should be noted that immediately after the deflection stage there is a pneumatic valve set up to close in the event of a loss of power to the vacuum pumps. This serves to reduce time lost while pumping back down to low pressure as the volume beyond the valve will remain at high vacuum. It also serves to allow vacuum to be broken on one half of the system without affecting the other, allowing each half of the setup to be separately maintained.

To determine whether there is a good, usable flux of atoms leaving the oven, a 1 cm^2 photodiode can be placed in the path of the 2D molasses beam to observe the fluorescence due to the Zeeman slower beam interacting with the atomic beam from the oven. A signal of 18-24 mV will result in an acceptable MOT of 90-100 mV.

2.7 MOT chamber/coils

For this setup, the MOT chamber, which immediately follows on from the pneumatic valve mentioned earlier, is custom made from a block of 316LN stainless steel. It is machined to be spherical but for 22 flat surfaces with a mixture of DN40 (14) and DN25 (8) conflat flanges, with the windows of the same AR coated, homemade design as in the deflection stage [67].

The magnetic coils required for the necessary quadrupolar field are placed outside the chamber and wound of 12 turns of water cooled, square profile copper pipe with inner diameter of 70 mm and separation of 132 mm. This, when running with the operating current of $\sim$ 210 A, produces a magnetic field gradient of $32G/cm$. A representation of the MOT chamber is shown in Fig. 2.19

The detection system, which detects the fluorescence of the atoms in the MOT, consists of an amplified photodiode (Femto PD Model: LCA-s-400K-SI)

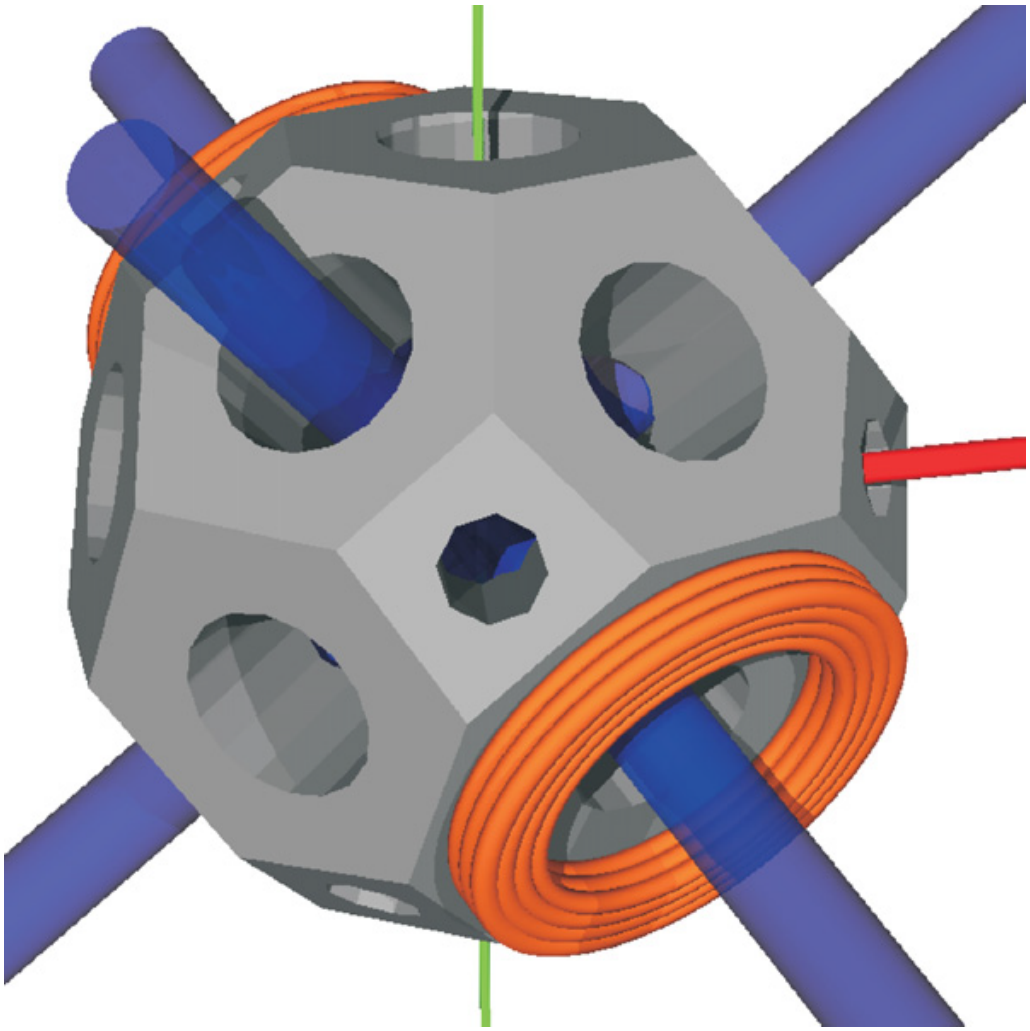

Figure 2.19: The MOT chamber. Blue represents the MOT beams, the red represents the atoms entering the chamber and the green is the optical access for the detection system. The magnetic coils are shown in Orange. The green shows the photodiode access direction [48].

with conversion efficiency at 423 nm of 1.0 x 10^{-6} V/W, and an achromatic lens system of focal length $f = 36$ mm situated 86 mm from the MOT chamber centre. The solid angle of this setup is 0.015. For this setup, a signal of 100 mV corresponds to a good MOT of $\sim 10^6$ atoms.

2.8 Atoms in the MOT

The signal from which the number of cold atoms trapped in a MOT is derived depends on several factors. In our setup, we have to take into account the following things: the signal observed by the photodiode detecting the florescence of the MOT, the response and position of the photodiode and the scattering rate of the transition in question.

The number of cold atoms in the MOT is given by:

$$N = \frac{4\pi V}{\Omega \Gamma_p E R_{PD}}, \tag{2.19}$$

where

V is the voltage read on the oscilloscope from the current measured by the photodiode,

$\Omega = \frac{A_{\text{lens}}}{4\pi d^2}$ is the fractional area observed by the focusing lens between the MOT and the photodiode,

A_{lens} is the area of the lens,

d is the distance from the lens to the MOT,

Γ_p is the scattering rate, as defined in Eqn (2),

$E = \frac{hc}{\lambda}$ is the energy of a single photon and

R_{PD} is the equivalent responsivity of the photodiode.

From the above equation, our typically observed ∼100mV MOT fluorescence signal indicates the presence of $\approx 10^6$ atoms, as seen in Fig. 2.20

If the same area was observed with the MOT coils switched off, as was typical during the day-to-day start up procedure, one should expect to see the (comparatively) diffuse and dull glow of the 3D molasses and a signal from the photodiode

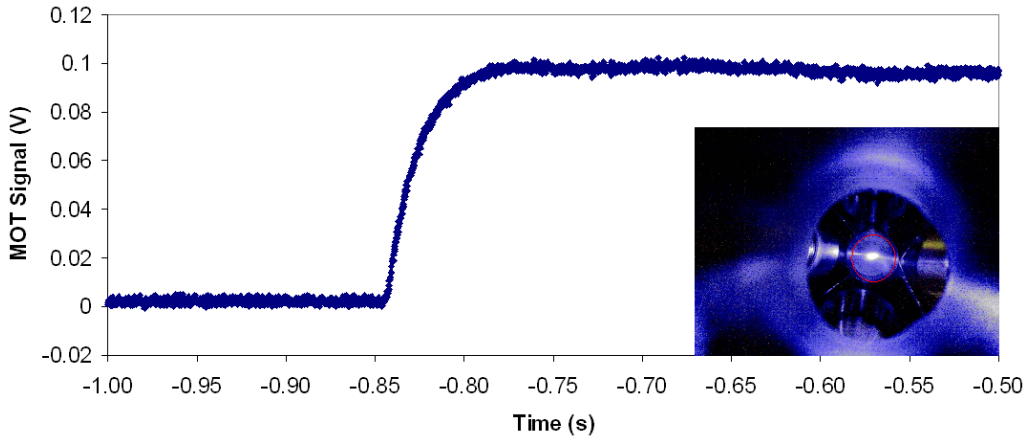

Figure 2.20: A typical 100 mV MOT signal. Inset: a photograph of a typical MOT, circled in red. The photograph was taken through one of the unused optical access ports.

of 5 - 10 mV. In the event of a similar signal with the MOT coils on, a number of parameters should be checked. The Zeeman beam fluorescence should be checked, as in the section of this chapter describing the deflection stage. If the Zeeman slower itself is working as it should, switching it off should reduce whatever MOT signal there is to practically zero, as should the blocking of the 2D Molasses beam. If either has a smaller effect than the other, it is a prime suspect. The issue most likely to be the problem is the Zeeman slower. As described in the deflection stage section of this chapter, the mirror can become coated in a film of calcium. This can be remedied either by running the heater or breaking vacuum and cleaning/replacing it.

Typical operating parameters for daily running of the calcium MOT are as follows. The oven is heated set at 23.5 V, 1.65 A on the front end corresponding to a temperature of 505°C and 20.4 V, 1.43 A on the back end, corresponding to a temperature of 495°C. The Verdi laser is run at 7 W, producing some 600 mW of 846 nm light from the Ti:S laser. Of this, 1.4 mW of blue light is generated in a single pass through one of the pp:KTP crystals and used for the SAS locking setup. ∼350 mW are coupled to the MOT laser table and into the blue enhancement cavity, producing between 100 and 150 mW of 423 nm light for the experiment. This light is then split between the MOT beams and the Zeeman

and molasses beams. At least 40 mW goes to the MOT beams, with the rest being split between the Zeeman and molasses beams. This can generally be relied upon to produce a 100 mV MOT, consisting of some $\approx 10^6$ calcium atoms. This optical setup is shown in Fig. 2.21

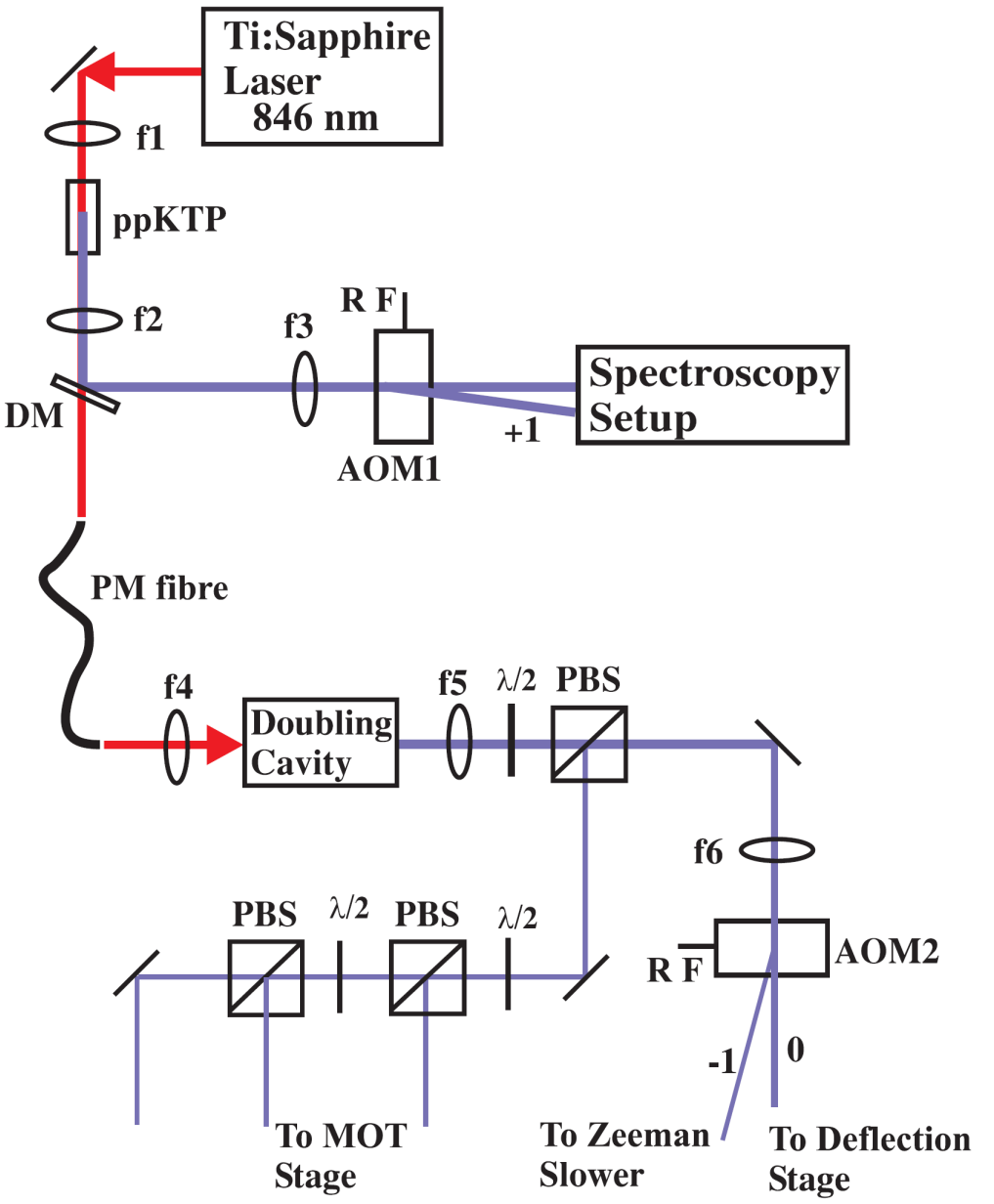

Figure 2.21: Optical layout of the calcium laser cooling and trapping experiment. ppKTP, frequency doubling crystal; DM, dichroic mirror; f1-6, lenses; AOM1 (RF = 80 MHz) and AOM2 (RF = 202 MHz), acousto-optic modulators; PM fibre, polarization maintaining, single-mode fibre; PBS, polarizing beam splitter; $\lambda/2$, half-wave plate [48].

Chapter 3

Effects of the 672 nm repump transition

This chapter is based in part on [46].

3.1 Introduction

As has been stated earlier in this work a closed transition is not 100% necessary for laser cooling, but it is advantageous. It is possible to laser cool without a closed transition, but the effectiveness depends upon the strength of the decay to states other than the ground state. In calcium, the $4s^2\ ^1S_0 - 4s4p\ ^1P_1$ transition is not closed, but the branching ratio for decay into the $4s3d\ ^1D_2$ is sufficiently weak that it is possible to obtain a MOT with a single laser frequency. In calcium, this transition has a branching ratio of 1:100000 [55], meaning that for every 100000 excited atoms, one will decay to the $^1D_2$ state. This compares favourably with other alkaline earths, such as strontium and barium, whose branching ratios for the same transition are 1:51300 [68] and 1:330 [69] respectively. For strontium, this branching ratio is small enough that laser cooling is still possible with only one laser, but in the case of barium, a repump laser is required. A similar atomic species has also been laser cooled (and taken to BEC): ytterbium [30]. Yb is not a group two element, but has a similar atomic structure with similar transition wavelengths.

With calcium, while it is possible to laser cool and obtain a MOT without the need for a repump laser, such an additional laser offers benefits that can't be ignored. Without a repump laser, the decay to and from the $^1D_2$ level effectively

limits the lifetime of the trapped atoms to a few tens of milliseconds. With the rempump laser, the lifetime should improve, as should the number of trapped atoms and the rate at which they load the MOT. This chapter will explore and explain the various effects observed due to the presence of a laser on the 672 nm repump transition $4s3d\,^1D_2 - 4s5p\,^1P_1$.

3.2 Setup

3.2.1 672 nm laser

The 672 nm laser is an external cavity diode laser (ECDL) similar to the Arnold design [70]. A brief description of this laser follows. A high power single mode 660 nm laser diode (Hitatchi HL6545MG) is placed in a collimation tube (Thorlabs LT230P-B) mounted in a commercially available mirror mount. A threaded $f =$ 5mm lens is placed at the output of the collimation tube, adjustment of which allows fine control of the beam collimation. The beam is directed towards a 1800 lines/mm diffraction grating (Thorlabs GH13-18V) mounted at$\sim$37° from the beam direction, ensuring that the 1st order is reflected back on the face of the diode. The grating is mounted on an aluminium block bolted to the front of the mirror mount, upon which another mirror is also mounted. Up to 75% of the light from the diode is reflected off the grating in the zeroth order and exits the ECDL case via the mirror. The case is a simple die cast box with an anti-reflection coated window mounted in a bored hole as the exit channel. This type of ECDL is shown in Fig. 3.1.

This diode is specified to emit at 660 nm at room temperature, which is a substantial distance away from the desired wavelength of 672 nm. As was stated in the previous chapter, these laser diodes are temperature tunable by about 3°C/nm, meaning it is possible to increase the lasing wavelength of the diode to something more suitable by increasing its temperature by $\sim$36°C. Doing so, however reduces the effective lifetime of the diode and lowers the maximum output power due to the increase in the lasing threshold current and the reduced efficiency of the gain curve [71]. The outcome of these effects is that a laser diode specified to emit 120 mW of 660 nm laser light at room temperature actually produces

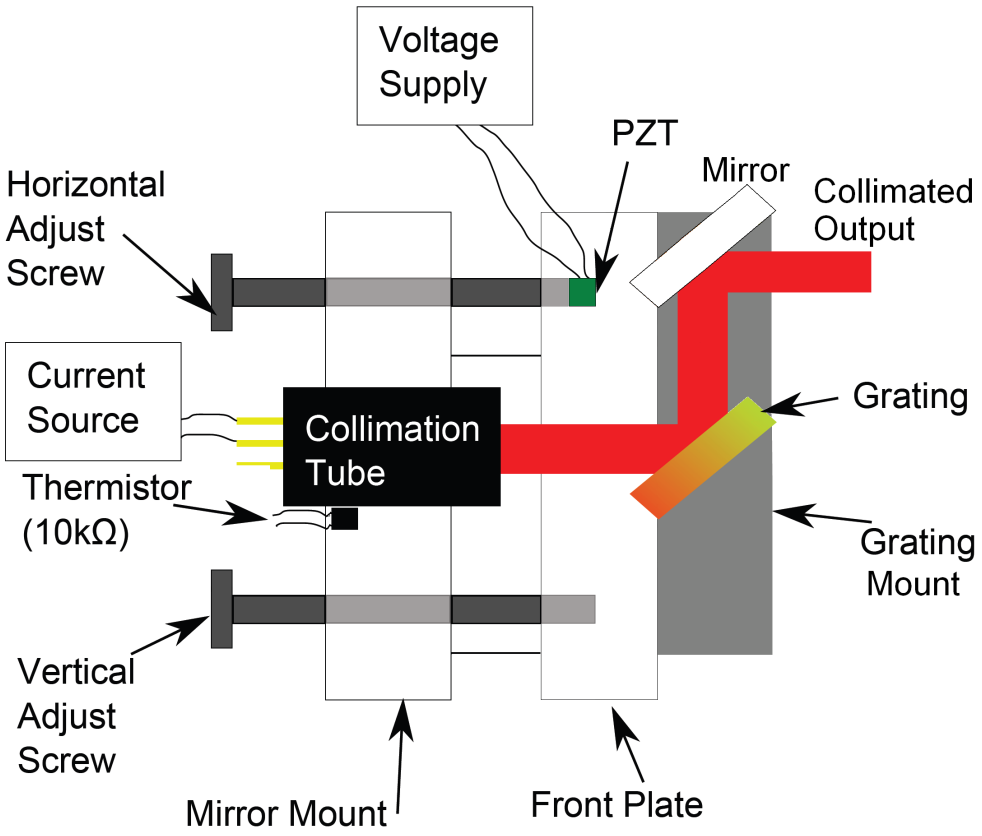

Figure 3.1: A diagram of the Arnold type of ECDL, which is similar to the design used for this part of the experiment. Note this is only a representation. Adapted from [50].

between 20 mW and 40 mW of 672 nm laser light off the grating at $\sim 55°$C. This is acceptable as it is sufficient power for locking the laser and performing any experiments. The laser diode current is driven by a Thorlabs current controller (LD1255R), with additions to allow fine and coarse adjustment of the current and easy access to apply an external modulation to the current. The diode is temperature controlled by resistive heating driven by a temperature controller (Wavelength Electronics MPT-5000). The feedback to the temperature controller is derived from a 10 kΩ thermistor housed in a hole drilled into the mount. However, it was found that in this configuration, the temperature measured in the mount was some $10-15°$C higher than was measured next to the collimation tube so an additional thermocouple was inserted between the collimation tube

and the mount. This ad-hoc fix means the temperature can still be kept stable by the temperature controller, while allowing for more accurate readings of the temperature of the diode. This put to rest fears that the diode was having to be run at too high a temperature.

Once the diode is raised to about the right temperature, the grating orientation is adjusted by the vertical and horizontal adjustment screws on the mount to optimise optical feedback onto the face of the diode. Once this has taken place, fine adjustment of the horizontal screw alters the position of the grating and allows control over the laser frequency. In this way, the laser was brought to a wavelength of 671.953(1) nm [72].

3.2.2 General setup

For the work in this chapter the MOT is run as normal, with a $\sim 10^6$ atoms. The 672 nm beam is directed towards the MOT chamber and passed through the centre of the chamber and thus the centre of the MOT. This is determined by observing the effects of the 672 nm beam on the MOT signal and adjusting its path to optimise this.

For laser stabilisation, a portion of the 672 nm light is directed through a single mode polarisation maintaining optical fiber to another laser table and coupled into a Fabry-Perot cavity with 300 MHz free spectral range (FSR) and finesse of approximately 300. This cavity is itself locked to a stable helium neon (HeNe) laser [73]. If the 672 nm laser were then locked to the cavity as is, it would not, generally speaking, be on resonance with the transition in question. To get around this, we radio frequency modulate the laser by way of a bias-tee and lock one of the resulting sidebands to the cavity by way of a lock-in amplifier (SRS SR510). By varying the modulation frequency with an RF source (Hameg HM 8133-2 with typical parameters being between 50 MHz and 70 MHz, -2 dBm leading to approximately 10% beam power in each first order sideband) applied to the laser, we can vary the offset between the actual laser wavelength and the frequency the laser is locked to. By doing this, we ensure the laser remains locked to the cavity, which itself remains locked to the stable HeNe laser and the 672

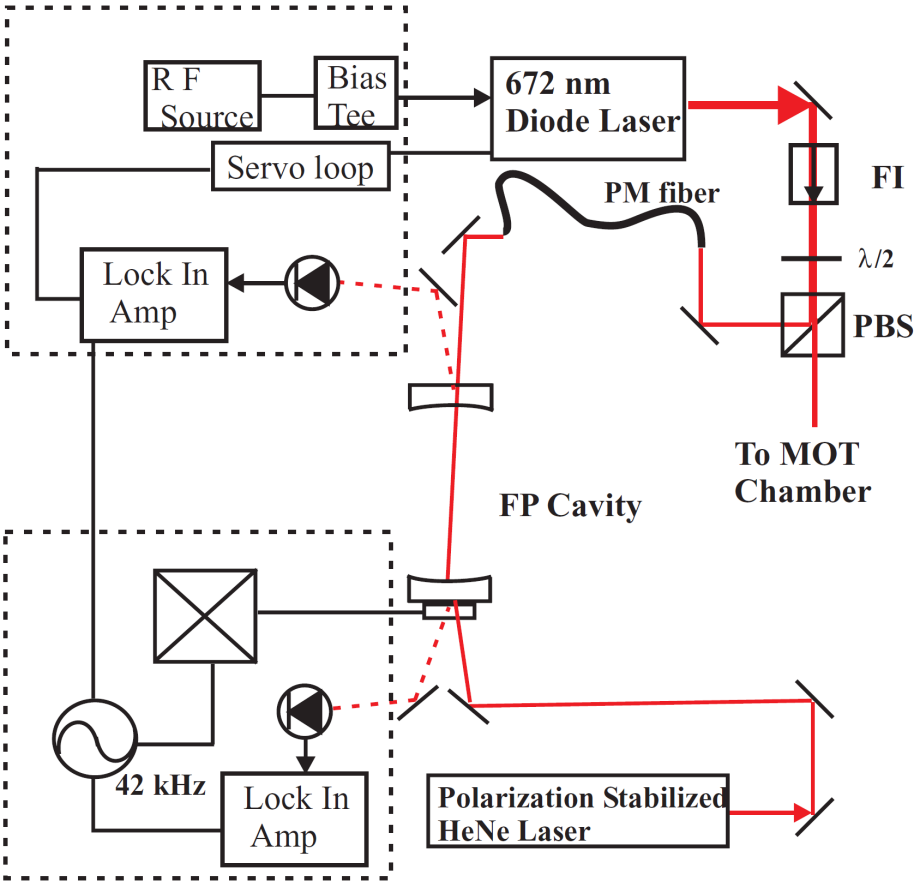

Figure 3.2: The locking setup for the 672 nm laser. FI = Faraday isolator(Linos FI-630-5 SV). PM = polarisation maintaining [46].

nm laser remains on resonance with the desired transition. This is gone into in more detail in [50]. This locking setup is shown in Fig. 3.2.

An example of the typical RF sidebands observed together with an example of the locking signal produced by such sidebands is seen in Fig. 3.3.

The HeNe laser is a standard two-mode internal-mirror-type laser with successive oscillating modes that are linearly polarised but orthogonal to each other. the cavity length is kept stable using thermal feedback to a fixed ratio of the power in the two orthogonal polarisations [74]. The stability of the HeNe laser is better than 10MHz a day. This could be measured by beating two identical systems against each other and observing how the beat note evolves over time.

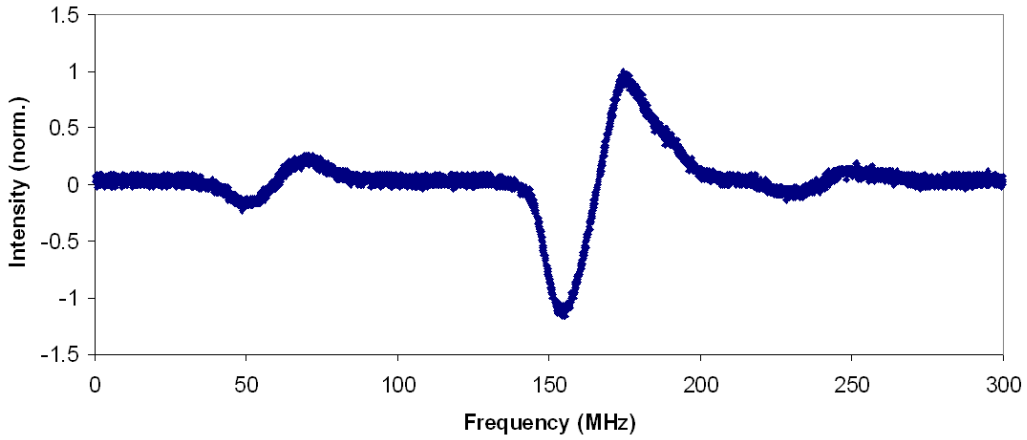

Figure 3.3: Examples of RF sidebands.

3.3 Effects of the 672 nm laser on the MOT

The first and most important reason time and effort was invested in investigating the $4s3d\,^1D_2 - 4s5p\,^1P_1$ repump transition at 672 nm was to 'plug the leak' of atoms out of the system caused by the 1:100000 decay from the $4s4p\,^1P_1$ state to the $4s3d\,^1D_2$ state. This effectively intercepts the leak out of the cooling cycle by pumping atoms into the higher $^1P_1$ level, whereby they can decay back to the ground state a number of different ways (see Fig. 3.4). This results in a increase in the number of trapped atoms in the MOT which, itself, is the result of improved MOT lifetime, capture efficiency and the clearing of a dark state. All of these effects will be explored in the following sections. It should be noted that while it might seem obvious to suggest simply repumping from the $^1D_2$ state to the $4s4p\,^1P_1$ state, but this is impractical due to the wavelength of this transition: some $5.5\mu m$.

3.3.1 Increase in number of trapped atoms

The most obvious improvement the 672 nm laser has is an increase in the detected MOT fluorescence, meaning more atoms are trapped. To get to this stage, however, the line first had to be found. To this end, the laser was directed towards the MOT while the frequency of the laser was scanned back and forth by

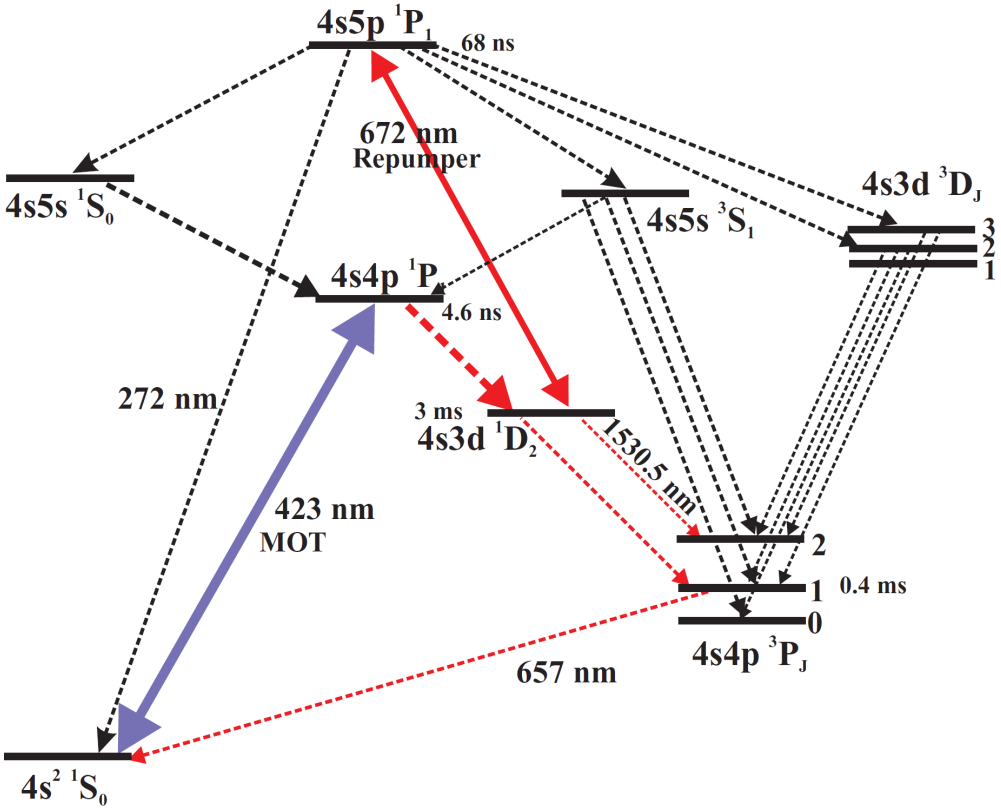

Figure 3.4: The relevant energy levels and transitions for calcium.

the PZT. As the laser frequency was scanned, the MOT fluorescence signal was observed. An early example of this is shown in Fig. 3.5.

To further attempt to improve on this signal, once optimised, a mirror was placed on the far side of the MOT chamber to retro-reflect the 672 nm beam back on to the MOT. When the initial beam is well aligned, this makes little difference to the MOT signal, but was useful as a quicker fix if the initial beam became slightly misaligned, so was kept in the setup. It became apparent why the retro-reflected beam had little positive effect when we took into account that we are exciting a J=2 to J=1 transition, a simple example of which is seen in Fig. 3.6

From Fig. 3.6 it can be seen that with linear polarisation, the $m_J = -2, 2$ sublevels have nowhere to go. Such 'unpumpable' state are referred to as dark states. A dark state could be considered to have infinite saturation intensity.

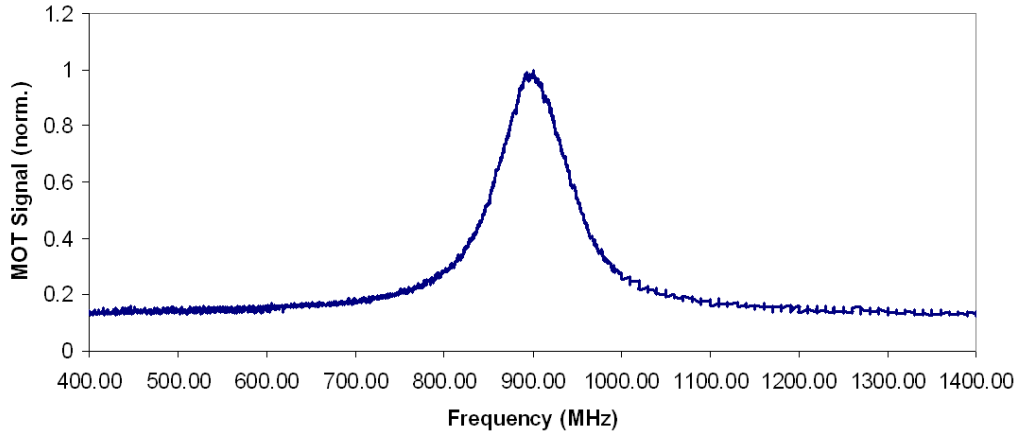

Figure 3.5: The MOT fluorescence signal as the 672 nm laser is scanned with the PZT.

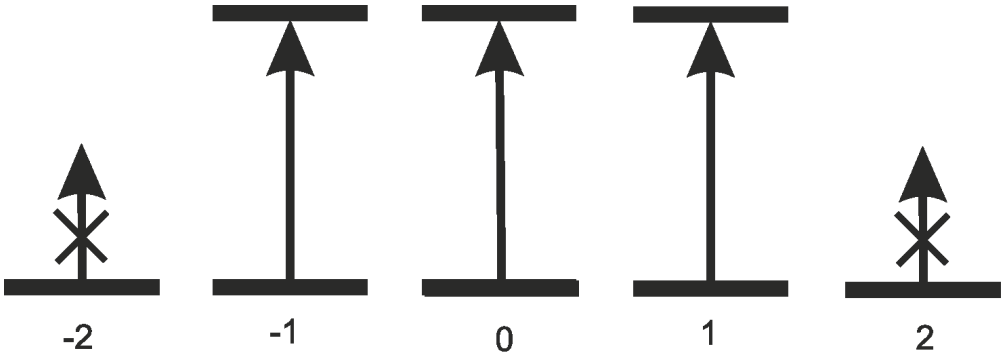

Figure 3.6: How the available states are pumped with linearly polarised light in a J=2 to J=1 transition. In this example, atoms which end up in $m_J = -2, 2$ cannot be interacted with at the same time as the other three.

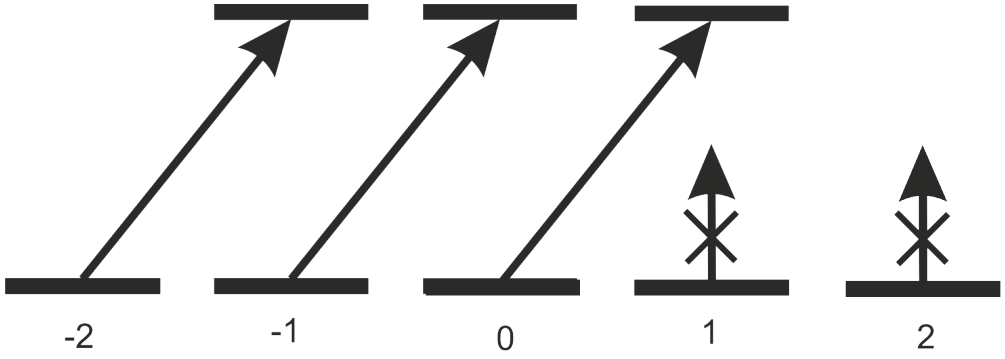

Figure 3.7: How the available states are pumped with circularly polarised light in a J=2 to J=1 transition. In this example, atoms which end up in $m_J = 1, 2$ cannot be interacted with at the same time as the other three.

This leads to the effective saturation intensity being greater than the calculated saturation intensity for such a transition. If the saturation intensity of these transitions were *actually* infinite, there would be no hope of exciting the transition. However, as the atoms change position within the trap region they start to see light of slightly differing polarisations and hence get partially coupled back into the 'bright' states. The result is that, while the saturation intensity is higher than it should ideally be, it isn't actually infinite, as it would be if the atoms were completely stationary. In an attempt to address these dark states, a quarter wave plate (QWP) was placed in the beam path after the MOT chamber, but before the retro-reflecting mirror to attempt to access the unpumped sublevels of the $^1D_2$ state, as shown in Fig. 3.7

On the face of it, it should be expected that using two beams of opposite circular polarisation would allow us to interact with these dark states. Consider Fig. 3.7. If one circular polarisation is used, the $m_J = -2, -1, 0$ are coupled to the excited states above and the $m_J = 1, 2$ are not, as shown. If the opposite circular polarisation was used, the $m_J = -2, -1$ would be uncoupled and the $m_J = 0, 1, 2$ would be coupled. In this way, there should be no dark states as the retro-reflected beam would interact with those states the incoming beam ignored. However, this is not the case. With the two beams overlapping with each other, the two opposing circular polarisations effectively combine to linear polarisation

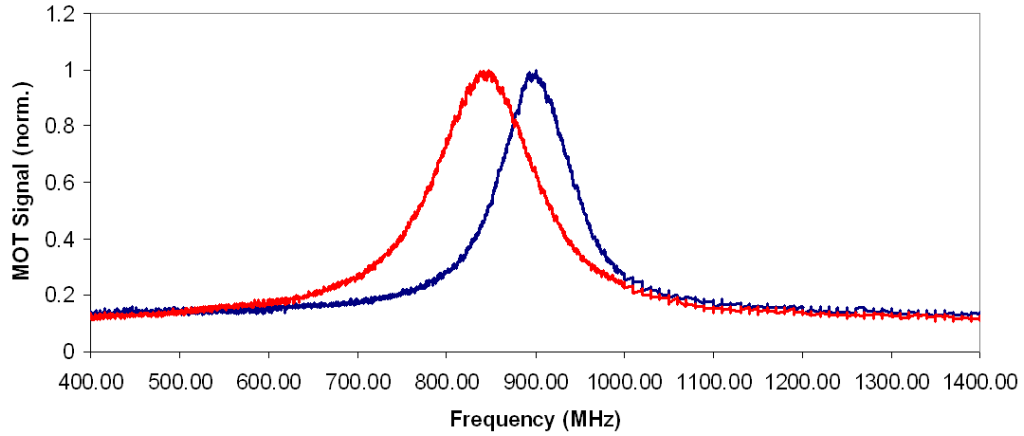

Figure 3.8: The MOT fluorescence signal with no retro-reflected beam (blue) and with a retro-reflected beam and QWP (red). Both signals are normalised to the peak of the non-retro-reflected signal.

at all points in space. This will always leave $m_J = -2, 2$ permanently uncoupled.

As a result, the addition of the QWP shows no increase in MOT signal. The comparison between the MOT signal with no retro-reflected beam and with the retro-reflected beam and a QWP was seen in Fig. 3.8. This was repeated several times with different rotation angles of the QWP, but as all were identical, only one is shown.

The difference in frequency between the two peaks is simply the result of the laser drifting in frequency over time. The difference in linewidths of the two peaks is most likely due to the additional power due to the retro-reflected beam .

It may be possible to 'fix' the dark state problem by 'scrambling' the polarisation by using a Pockels cell to very quickly switch between one polarisation and another and so interact with the dark states on a fast time scale.

With the alignment of the 672 nm laser beam optimised for maximum increase in MOT signal and locked on resonance, the typical improvement in MOT signal seen could be up to a factor of 13, as seen in Fig. 3.9. We expect an increase because of three factors. First we plug the leak from the $4s4p\,{}^1P_1$ level . Secondly, we detect atoms that were previously left in the ${}^1D_2$ level. We also improve the MOT loading rate.

For this experiment, a simple timing sequence was employed whereby the 672

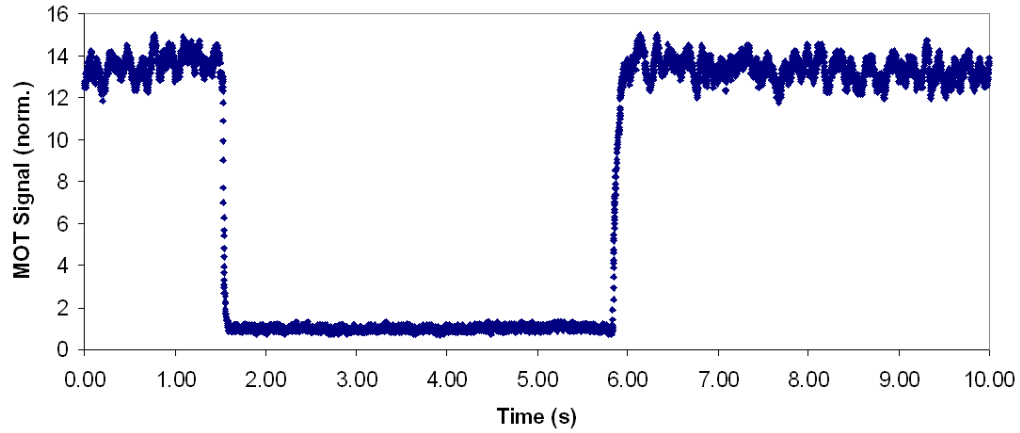

Figure 3.9: An example of how the MOT signal is improved by the presence of the on resonance 672 nm laser.

nm laser was blocked and unblocked for several seconds at a time. The increase of a factor of 13 suggests 13 times more trapped atoms, but it is worth noting that some of these atoms were already in the trap region, our detection system just could not see them until they interacted with the MOT beams as they had been stuck in the $^1D_2$ level.

The effects of the 672 nm laser beam were modeled as part of a system of rate equations which calculate the changes in populations of the various energy levels. To begin with, start with an ideal, two level system. In such a situation, the rate equations would be as follows

$$\dot{N}_1 = R - L(\Delta, I)(N_1 - N_2), \tag{3.1a}$$

$$\dot{N}_2 = L(\Delta, I)(N_1 - N_2) - \gamma N_2, \tag{3.1b}$$

where R represents the trap filling rate, $L(\Delta, I)$ is the laser drive term, $N_{1,2}$ are the populations of the ground state (level 1) and the excited state (level 2) and γ is the rate of decay out of N_2. For $\dot{N}_1$, the population is determined by the rate at which atoms enter the trap, R, less those that laser drives out of state level 1 ($L \times N_1$). The laser simultaneously back couples atoms from state 2 to state 1 ($L \times N_2$). For $\dot{N}_2$ the population is a result of those excited to it from state

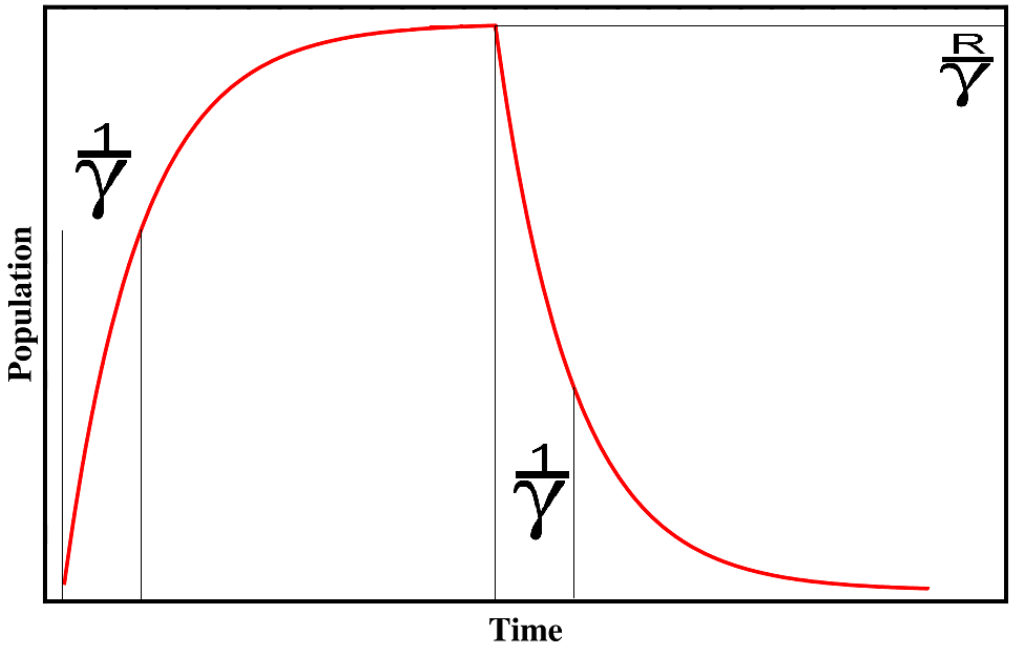

Figure 3.10: How the population of the excited state in a two-level system would evolve over time. Also shown is the lifetime ($1/\gamma$) and the maximum population level (R/γ).

1 ($L \times N_1$), less those that back couple to state 1 again ($L \times N_2$). Additionally, there is a loss based on the decay time from state 2 (γN_2). Solving this for N_2 as a function of time gives the curve seen in Fig. 3.10. It can be seen that once the laser has been on for a certain time characteristic of the system in question, no additional atoms are trapped.

The actual rate equations are then [50]

$$\dot{N}_1 = R - L(\Delta, I)(N_1 - N_2) + \Gamma_{21}N_2 + (1-\varepsilon) \times \Gamma_{31}N_3 + (\Gamma_{51} + \alpha\Gamma_{54})N_5, \tag{3.2a}$$

$$\dot{N}_2 = L(\Delta, I)(N_1 - N_2) - (\Gamma_{21} + \Gamma_{23})N_2 + \Gamma_{52}N_5, \tag{3.2b}$$

$$\dot{N}_3 = \Gamma_{23}N_2 - (\Gamma_{31} - \Gamma_{34} + \Gamma_r)N_3 + (\Gamma_{53} + \Gamma_r)N_5, \tag{3.2c}$$

$$\dot{N}_4 = (\Gamma_{34} + \varepsilon\Gamma_{31})N_3 + (1-\alpha)\Gamma_{54}N_5, \tag{3.2d}$$

$$\dot{N}_5 = \Gamma_r(N_3 - N_5) - (\Gamma_{51} + \Gamma_{52} + \Gamma_{53} + \Gamma_{54})N_5, \tag{3.2e}$$

$$\tag{3.2f}$$

where

$$L(\Delta, I) = \frac{s\Gamma_{21}}{2[1 + s + (2\Delta/\Gamma_{21})^2]} \tag{3.3}$$

is the 423 nm drive term. For these rate equations the levels are labeled as follows: $^1S_0$ is level 1, $4s4P^1P_0$ is level 2, $4s3d^1D_2$ is level 3, $4s4p^3P_2$ is level 4 and $4s5p^1P_1$ is level 5. This is shown in Fig. 3.11.

In the rate equation model $s = \frac{I}{I_{sat}}$ is the saturation intensity of the $^1S_0 - ^1P_1$ transition, and, from the literature [55, 75], $\Gamma_{21} = 2.18 \times 10^8 s^{-1}$, $\Gamma_2 = 2180 s^{-1}$, $\Gamma_{31} = 700 s^{-1}$, $\Gamma_{34} = 96 s^{-1}$, $\Gamma_{51} = 2.61 \times 10^5 s^{-1}$, $\Gamma_{52} = 2.13 \times 10^6 s^{-1}$, $\Gamma_{53} = 1.21 \times 10^7 s^{-1}$ and $\Gamma_{54} = 3.4 \times 10^5 s^{-1}$. Γ_{31} is the sum of the direct decay to state 1 from state 3 and the decay rate from state 3 via the $4s4p\,^3P_1$ state and is based on experimental observations [48, 76]. R is the filling rate, α is the fraction of atoms which decay to the triplet scheme and are lost, Γ_r is the 672 nm laser drive term and ε represents the small fraction of atoms which, while decaying to the $^3P_1$ state which decays to the ground state in $\sim$400 μs, are lost from the cooling cycle. The atoms which do decay to the ground state from the $^3P_1$ state are represented by a direct decay from level 3 to level 1. A slight modification to and more complete explanation and rigorous testing of the rate equation model appears in the following chapter.

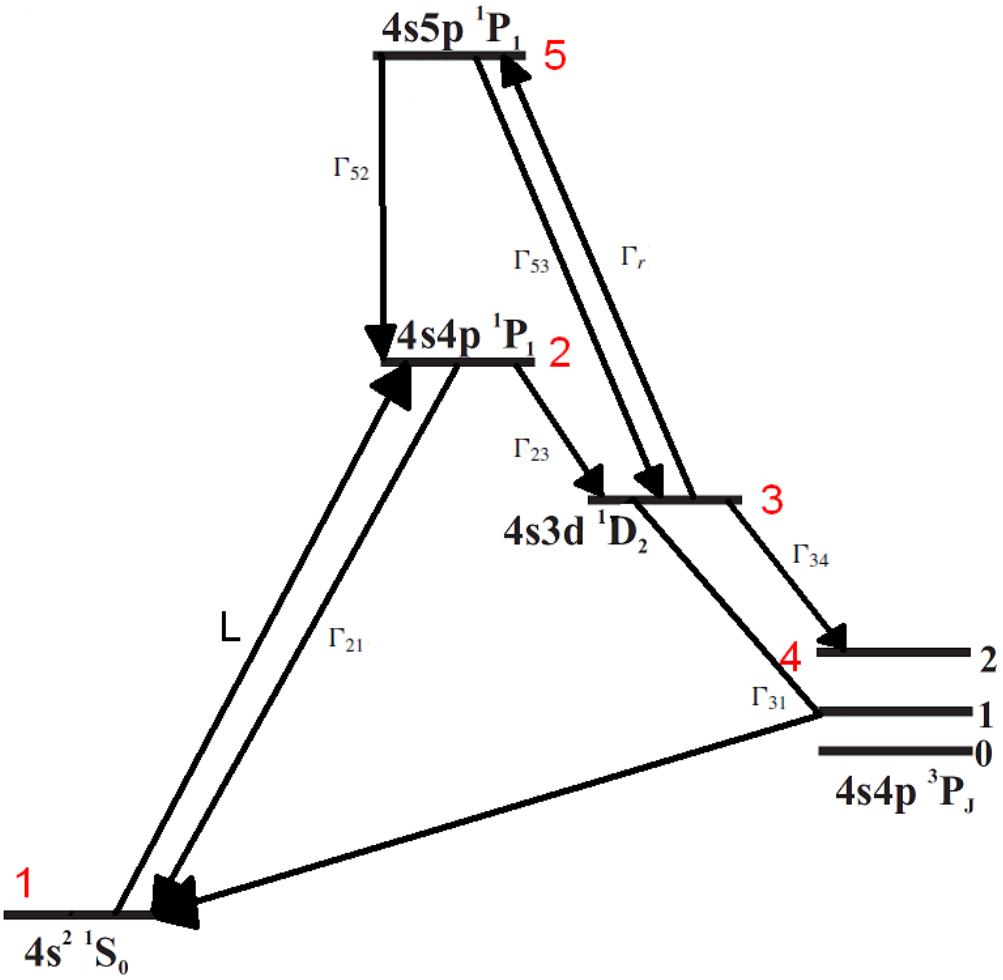

Figure 3.11: The levels and decay rates as referred to in the rate equation model. there are two additional decays from level 5 (Γ_{54}, Γ_{51}) which are left out for the sake of clarity.

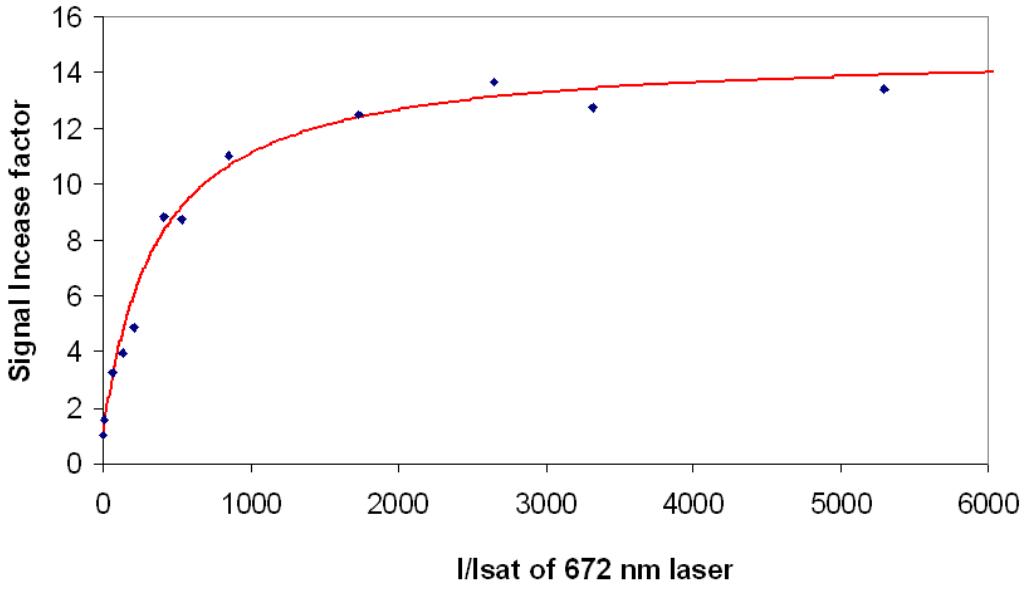

Figure 3.12: The MOT improvement factor with increasing 672 nm beam intensity. The blue points are the experimental data and the red curve is obtained from the rate equation model.

In order to observe how the improvement in MOT signal as a result of the 672 nm laser varied with the intensity of the 672 nm laser, the same data was taken for various different 672 nm beam powers. This is seen in Fig. 3.12. The blue points are the experimental data, the curve is the simulation derived from the rate equation model.

This shows that beyond a certain intensity of the 672 nm laser, there is no improvement in the number of trapped atoms. This corresponds to a beam power of 3-4 mW (I/Isat $\simeq$ 300). For the saturation intensity, a value of 1 mW/cm^2 is calculated using $I_{sat} = \frac{\pi hc}{3\lambda^3\tau}$. This is probably significantly lower than the effective saturation intensity due to the aforementioned dark states. This also explains why such a large saturation parameter is necessary before the maximum improvement in trapped atom number is reached.

It is worth noting that there is a more 'complete' alternative to rate equations for this application: density matrix equations, which describe quantum systems in mixed states. However, for two-level systems, rate equations are adequate. While we are not strictly dealing with a two level system, there are factors working in

our favour that allow us to treat it as a collection of such. This is explained in the next chapter.

3.3.1.1 Improvements in MOT lifetime

Part of the reason for the increase in the number of trapped atoms seen is down to an increase in the MOT lifetime, which is due to our plugging the leak into the $^1D_2$ level, as was our original intention. With the 672 nm laser on resonance, the lifetime of the MOT increases by up to a factor of ~ 3. As atoms therefore spend longer in the MOT before being lost, it follows that at any given time, more atoms are trapped. This increase in lifetime will be explained in this section.

Shown in Fig. 3.13 is the difference in both MOT fluorescence signal and loading rate/lifetime due to the presence of the on resonance 672 nm repump laser. The difference in lifetime can be seen simply from the difference in the slopes of the two curves.

To further test this a gating system (Fig. 3.14) was implemented whereby different beams were turned off and on with specific timings and the results measured. To begin with, the MOT is loaded for 400 ms with no 672 nm light present followed by the 2D molasses used for the deflection of the slower Zeeman slower atoms being switched off. This stops new atoms being introduced to the MOT region. After the 20 ms, the 672 nm laser is switched on for 400 ms. This results in the data shown in Fig. 3.15.

From Fig. 3.13 and Fig. 3.15 it can be seen that in the presence of the 672 nm repump laser the MOT lifetime increases by a factor of ~ 3 from 16 ms to 47 ms from the comparison between the loading curve and the second decay curve. This is still shorter than would be expected due to background gas collisions and inelastic two-body collisions between the cold calcium atoms [33]. The initial jump (seen at time 0s in Fig. 3.15) represents the atoms that get pumped out of the $^1D_2$ level.

The reason for the lower than expected lifetime is that the 672 nm transition is not an ideal repump transition. 81.5% of the atoms excited by the laser decay back on the same transition. This arises from the A coefficients listed in Table 3.1. It can easily be seen that the decay rate from $4s5p\,^1P_1$ to $4s3d\,^1D_2$ is considerably

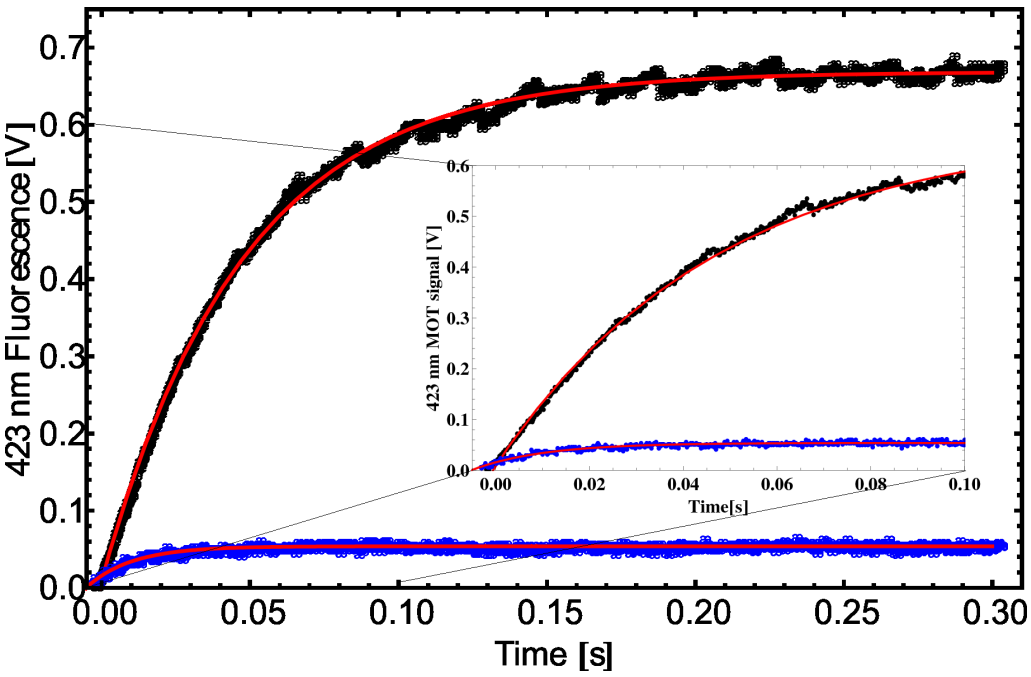

Figure 3.13: The MOT signal without (blue) and with (black) the 672 nm repump laser. The solid curves are exponential fits to the data. The change in signal due to the 672 nm laser is clearly visible. Also apparent is the increase in MOT loading rate. Inset: close up of both signals, more clearly showing difference in loading rate. The initial slope is given by the loading rate, R.

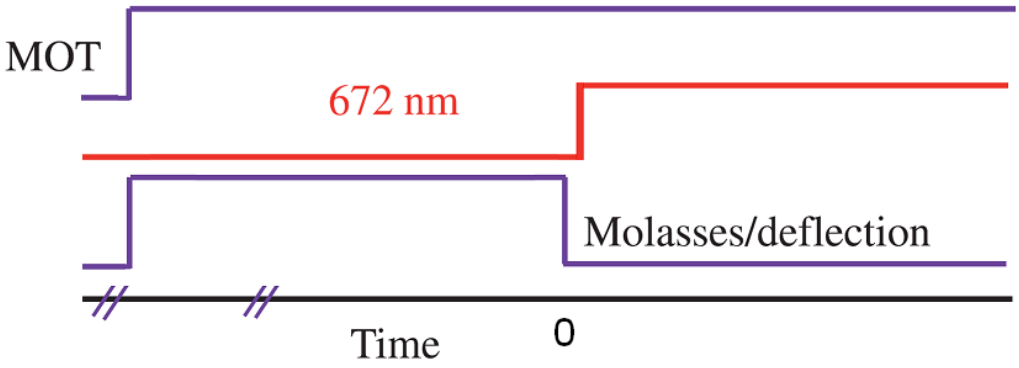

Figure 3.14: The timing of the gating system used to obtain Fig 3.15.

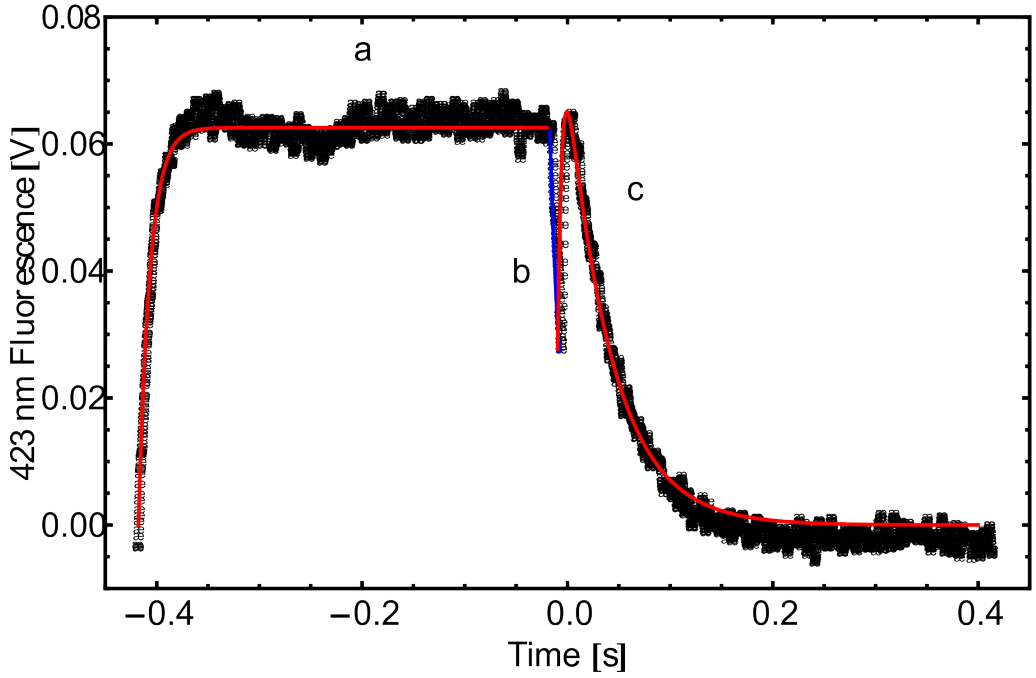

Figure 3.15: 423-nm MOT fluorescence in the absence and subsequent presence of the 672-nm repumper. (a) The MOT (lifetime 16 ms) is loaded for 400 ms after which filling is terminated by extinguishing the deflection laser beams after the Zeeman slower. (b) Decay of the 423-nm MOT (lifetime 16 ms) is allowed for 20 ms, which is larger than the transit time from the deflection region to the MOT. This ensures no further atoms are being loaded. (c) The 672-nm laser is switched on for 400 ms. The initial rise (with a time constant of 400 μs) is due to the atoms previously shelved in the $^1D_2$ state. The subsequent decay shows the increased lifetime of 43 ms for the repumped MOT.

larger than any of the other decays from this excited state. Apart from its tendency to increase the rate of pumping into dark states this in itself is not a problem for the actual repumping but merely results in an increased laser power requirement. Most of the rest of the atoms return to the ground state via the $4s5s^1S_0$ and $4s4p^1P_1$ levels providing the desired repumping. However, a small fraction decays to the triplet scheme, where approximately 50% end up in the long-lived $^3P_2$ and $^3P_0$ states and are lost from the cooling cycle. This also arises from the A coefficients in Table 3.1 from which it can be seen that of those atoms that decay to the triplet scheme, roughly half end up in the long lived states. This represents an overall loss of about 1.2% from the repumping cycle compared

Upper level	Lower level	$A_{ik}(10^7 s^{-1})$	$\lambda(nm)$
$4s5p\,^1P_1$	$4s5s\,^1S_0$	0.2126	2928.81^a
	$4s5s\,^3S_1$	0.01399	1926.00^a
	$4s3d\,^3D_1$	0.01053	609.89^a)
	$4s3d\,^3D_2$	0.009349	610.41^a
	$4s3d\,^1D_2$	1.209	671.954^b
	$4s^2\,^1S_0$	0.02674	272.2^b
$4s5s\,^1S_0$	$4s4p\,^1P_1$	2.435	1034.66^a
$4s5s\,^3S_1$	$4s4p\,^1P_1$	0.00001465	1267.8^a
	$4s4p\,^3P_0$	0.96	610.441^b
	$4s4p\,^3P_1$	2.87	612.391^b
	$4s4p\,^3P_2$	4.77	616.388^b
$4s3d\,^3D_1$	$4s4p\,^3P_0$	0.02149	1931.4494^a
	$4s4p\,^3P_1$	0.01565	1951.1064^a
	$4s4p\,^3P_2$	0.0009779	1992.2632
$4s3d\,^3D_2$	$4s4p\,^3P_1$	0.02838	1945.2893^a
	$4s4p\,^3P_2$	0.008869	1986.7614^a

Table 3.1: Transition rates (A_{ik}) and vacuum wavelengths (λ) from low-lying states in calcium. Data marked^{a,b} are from reference [72, 75] respectively.

with 17.3% being successfully repumped. Thus, given the ratio of atoms lost to those repumped, only 7% of atoms are lost from the system as opposed to the 22% lost without the presence of the repump laser due to the $4s3d^1D_2$ branching ratio to the $^3P_2$ state.

The 423 nm MOT fluorescence increases in the presence of the repump laser as atoms shelved in the $^1D_2$ state are brought back into the cooling cycle. As seen in Fig. 3.13 we have recorded the 423 nm fluorescence as the repump laser is switched on and in the absence of further loading of the MOT. For the typical operating conditions for the experiment we see an approximate doubling of the fluorescence on a timescale of 0.4 ms. The data shown in Fig. 3.15 are fitted with the three functions given below.

$$N(t) = N_0[1 - exp(-t/\tau_1)], \qquad t < t_0, \tag{3.4}$$

and

$$N(t) = N_0 exp[-(t/t_0)\tau_1)], \qquad t_0 < t < t_r \tag{3.5}$$

give curves (a) and (b) in Fig. 3.15, where t_1 is the loading and decay time for the 423 nm MOT. The loading takes place between $t = 0$ and $t = t_0$. The repumping laser is switched on at $t = t_r$ slightly after the filling has stopped to ensure that no new atoms are captured. The fluorescence signal now follows a more complicated expression so curve (c) in Fig. 3.15 is given by the solution to the differential equation

$$\dot{N}(t) = N_d exp[-(t/t_r)\tau_r]/\tau_r - N(t)/\tau_2, \qquad t > \tau_r \tag{3.6}$$

where the first term represents atoms previously in the $^1D_2$ state and brought into the cooling cycle by the repump laser and the second represents the decay (time constant t_2) of the MOT in the presence of the 672 nm repump laser. N_d is the initial number of atoms in the $^1D_2$ state and $1/t_r$ is the repump rate.

3.3.1.2 Improved efficiency in MOT loading

The beneficial effect of the 672 nm repump laser on the filling rate was not expected. Repumping is generally seen as unnecessary for the Zeeman slower as the 1:100 000 loss into the $^1D_2$ state is insignificant as an atom scatters of order 20×10^3 photons to slow from an initial velocity of order 500 m/s to near rest. However, the strongly over-damped nature of the MOT means that an atom spends much longer than the time taken for 20×10^3 photons to be scattered being fully captured into the centre of the MOT. For a hypothetical closed cooling transition using our experimental conditions, most atoms would scatter between 5×10^4 and 1×10^5 photons in this final stage of the trapping. Thus, for the real atomic system, there is now a significant probability of decaying into the $^1D_2$ state. About three quarters of these atoms will return to the ground state after approximately 3.5 ms. For atoms near the MOT centre this is not a problem as they are slow enough not to travel outside the MOT region in this time [58].

However, due to the strong damping of the cooling beams, atoms approaching the MOT center travel with a velocity such that the Doppler shift approximately equals the local Zeeman shift. This corresponds to 0.6 m s^{-1}/G, so atoms decaying to the $^1D_2$ state outside a 5-G contour will escape the MOT region before returning to the ground state. Thus, with the experimental 32-G/cm field gradient the majority of the region is outside this contour and atoms decaying to the $^1D_2$ state here will in general not be given a second chance of getting trapped.

The increase in signal due to previously shelved atoms being pumped out of the $^1D_2$ state is simply due to the fact that without the repump laser, approximately a third of the atoms in the whole system reside in this state. This follows from steady state (i.e. time independent) solutions of the rate equation model.

It should be noted, however, that these factors (the 3 times increase in lifetime, two times increase in detected atoms and two times increase in loading rate) could not be predicted by the rate equation model due to the fact that the decay rates used are not known to a great degree of accuracy. The rate equation model could only account for an improvement in lifetime of a factor of 1.8 and an increase in previously shelved $^1D_2$ atoms of a factor of 1.4. The model then suggests that there is an increase in loading rate of a factor of 5. These are simply not seen experimentally.

The net result of these factors is that we improve the MOT lifetime by a factor of three and gain more than an order of magnitude in the number of trapped atoms detected. It is this increase that led to the next part of this chapter: the isotope shift measurements.

3.4 Isotope shift measurements

In addition to investigating the effects the 672 nm laser on the MOT population, it was decided that an additional experiment would be performed. When an atom has the same atomic number, but a different number of neutrons, it is called an isotope of the element in question. As a result, the isotope will also have a different mass, volume and mean square charge radius to the 'standard' atom. This results in a difference in the transition frequencies between energy levels for each different isotope. this is known as the isotope shift (IS). The main isotope

used for laser cooling experiments in calcium, ^{40}Ca, has a natural abundance of ∼97%. While the isotope shifts for various isotopes are known on the 423 nm main cooling transition [77], until this work, they were not known on the 672 nm repump transition. Gaining an increase in the number of trapped atoms of an order of magnitude will be an attractive prospect for anyone working with some of the even isotopes [78] (natural abundances of 0.647%, 2.086%, 0.004%, 0.187% for ^{42,44,46,48}Ca, respectively [54]) and especially those attempting to use ^{41}Ca for radio calcium dating given its half-life of 1.02 x 10^5 years [54] or for the treatment of osteoporosis [79, 80] given the extremely low natural abundance ratio (^{41}Ca/Ca) of $10^{-14} - 10^{-15}$ [81, 82]. In this work, we were able to determine the isotope shifts between the four most abundant isotopes and from this we were able to estimate the isotope shifts for three additional low abundance isotopes, including ^{41}Ca.

3.4.1 Background theory

The isotope shifts of a transition in an element have contributions from three components [83, 84], which can be written as:

$$\delta\nu^{AA'} = M\frac{A' - A}{A'A} + F \cdot \delta\langle r^2\rangle^{AA'}, \tag{3.7}$$

where:

$\delta\nu^{AA'}$ is the shift between isotope of atomic mass A and isotope of atomic mass A',

M is the mass shift coefficient,

F is the field shift (sometimes known as the volume shift) coefficient and

$\delta\langle r^2\rangle^{AA'}$ is the change in mean square charge radii between isotope A and isotope A'.

The mass shift coefficient can be split into the normal mass shift(M_{NMS}) and the specific mass shift (M_{SMS}). M_{NMS} is given by

$$M_{\mathrm{NMS}} = \nu_0 \frac{m_{\mathrm{e}}}{m_{\mathrm{u}}}, \tag{3.8}$$

where:

ν_0 is the transition frequency,
m_{e} is the electron mass and
m_{u} is the atomic mass unit.

If M_{NMS} is subtracted from the total IS, what is left is the residual isotope shift (RIS), $\delta\nu_{\mathrm{RIS}}^{AA'}$. With this in mind, and multiplying by the mass factor $AA'/(A'-A)$, equation (3.7) becomes

$$\delta\nu_{\mathrm{RIS}}^{AA'} \cdot \frac{A \cdot A'}{A - A'} = M_{\mathrm{SMS}} + F \cdot \delta\langle r^2 \rangle^{AA'} \cdot \frac{A \cdot A'}{A - A'}. \tag{3.9}$$

Values for M_{SMS} and F can be obtained from a plot of the modified RIS against the modified $\delta\langle r^2 \rangle^{AA'}$.

3.4.2 Experimental setup and method

The experimental setup for the isotope shift measurements was broadly the same as for the rest of this chapter. The main difference was that, instead of locking the 672 nm laser to a reference cavity, the same portion of light was instead coupled into a high finesse Fabry Perot cavity. We can get away with the laser being unlocked as we do not need an absolute frequency reference for this experiment, a relative frequency reference is sufficient. This cavity is made of ultra low expansion (ULE) glass (length change of 0.025nm/year [85]), is $\sim$ 100 mm in length and comprises one flat mirror and one mirror with a radius of curvature (RoC) of 500 mm. The cavity has a free spectral range (FSR) of $\sim$ 1.5 GHz (1498.9 MHz) , a finesse of approximately 300000 and is housed inside a temperature stabilised vacuum chamber maintained at a pressure of 3.9×10^{-9}mbar. Transmission through the cavity as the 672 nm laser is scanned is observed via

a photodiode and the transmission peaks are used in this case as a frequency reference.

It is common knowledge that if a single mode laser is perfectly aligned into such a cavity, there will be single mode transmission peak separated by the cavity FSR. If, however, the laser is not perfectly aligned into the cavity, higher order laser modes will appear at set, well defined frequencies, as given by [86]

$$\Delta\nu \simeq \frac{c}{2\pi z_0}, \tag{3.10}$$

where:

c is the speed of light,
$z_0 = \sqrt{(d \cdot ROC) - d^2}$ is the confocal parameter of the cavity and
d is the length of the cavity.

A nice feature of this particular cavity is that, given $FSR = c/2L$ and the fact that $z_0 = 2d$, then

$$\Delta\nu \simeq \frac{FSR}{2\pi}. \tag{3.11}$$

Given that the spacing of these modes is known, they can be used as frequency markers, which is precisely what we have used them as. In our case, each higher order mode is separated from the next by 238.6 MHz. Knowing this provides us with a finer scale for calibrating the frequency. A sample of the high finesse cavity transmission peaks is shown in Fig. 3.16

However, it is not quite as simple as that. It is also well known that the scan of a PZT is not 100% linear in nature. This has to be taken into account. Luckily, as the position of each higher order transmission peak relative to the next is exactly known, we can use this to eliminate this scan nonlinearity from our data. Simply by calculating where, in frequency, a peak appears against where it *should* appear

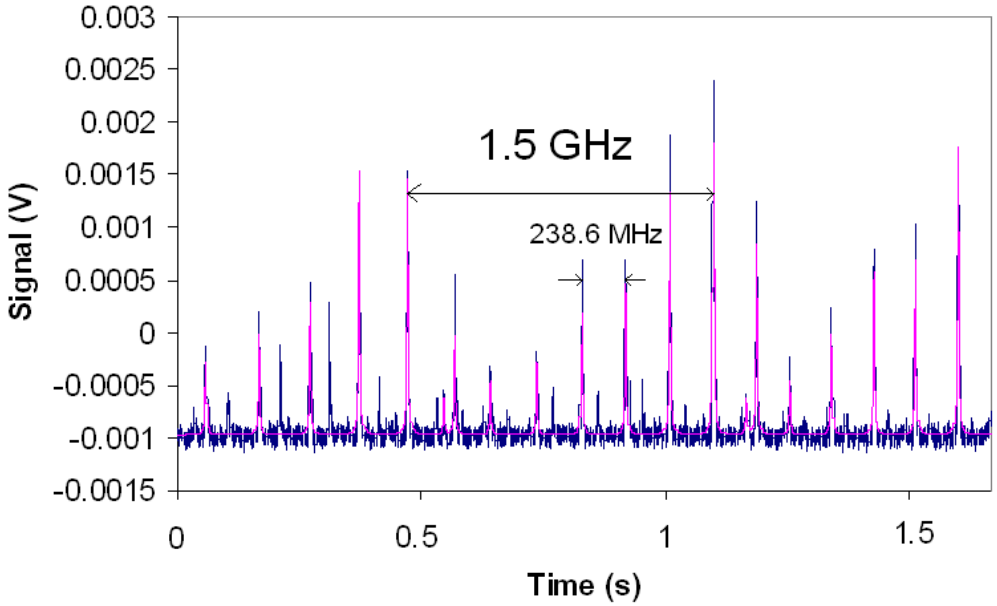

Figure 3.16: The high finesse cavity transmission peaks and the Lorentzian fits to them as the laser frequency is scanned.

and performing a polynomial fit to the results, we can obtain a frequency axis that can be trusted and thus used as a reference.

The mode spacing with a polynomial fit to it is shown in Fig. 3.17. The equation for this polynomial fit is then applied to the mode spacings from the experimental data and the difference between the experimental data and the result is plotted. As the data is clearly not linear in nature, we apply the lowest order polynomial we can and note the result for this second order polynomial still shows a definite trend, as seen in the blue trace in Fig. 3.18. We then try a third order and note that the trend largely vanishes, as shown by the green trace. As the 4th order polynomial shows no further improvement (red trace), we conclude that we need go no further. The settled upon polynomial fit is then applied to the experimental data itself, which enables us to produce a frequency axis, as shown in Fig. 3.19.

With this frequency reference in hand, it is now possible to begin to determine the relative frequencies of the different isotopes. The frequency of the main cooling laser was adjusted to where each specific isotope was expected to be found. To ensure we were at the right frequency, a CCD camera was aimed directly at

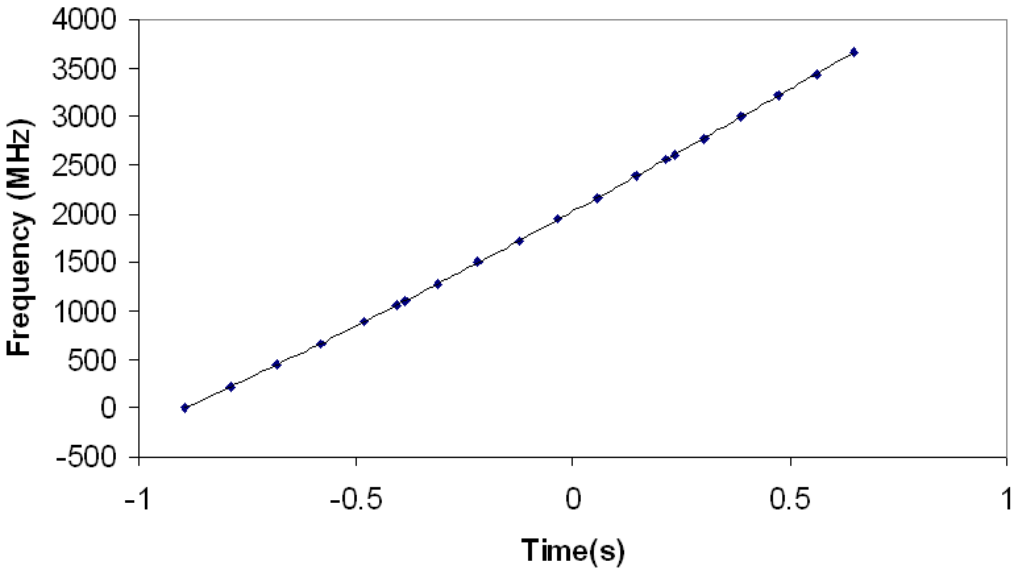

Figure 3.17: The mode spacing through the high finesse cavity and the polynomial fit to the data points.

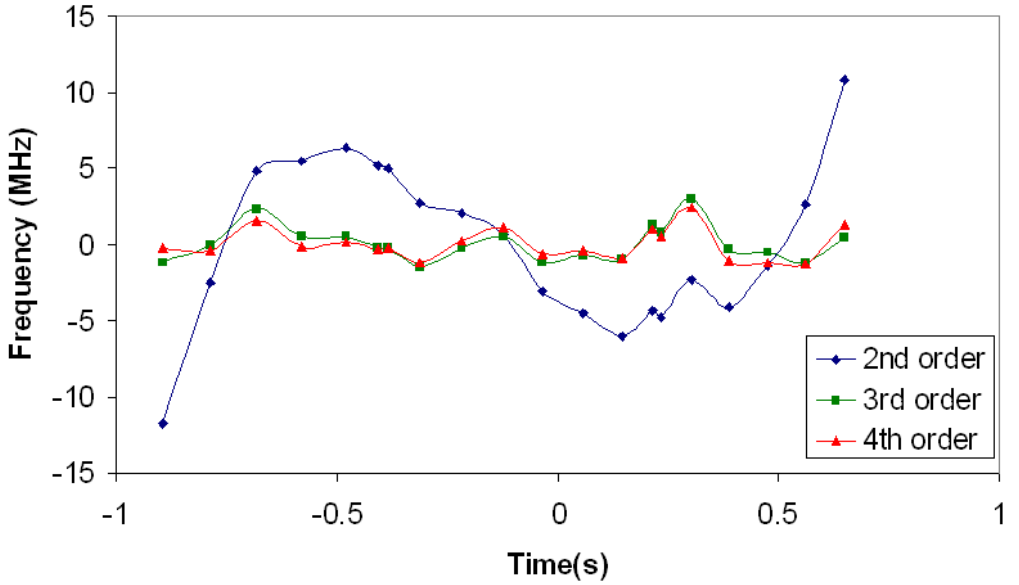

Figure 3.18: The difference between the mode spacings observed and those calculated by each of the different order polynomial fits.

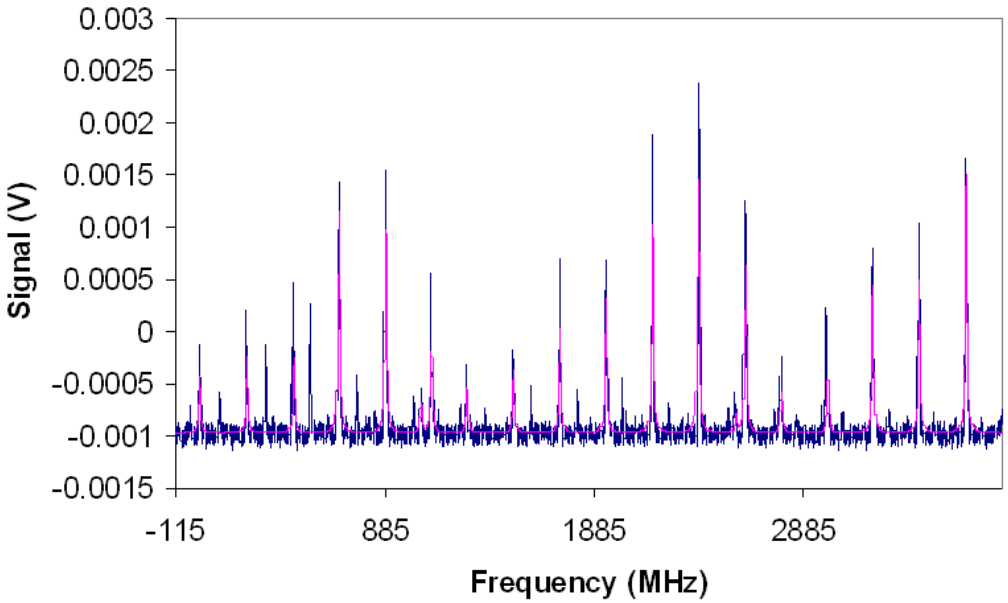

Figure 3.19: The high finesse cavity transmission peaks and the Lorentzian fits to them as the laser frequency is scanned, with frequency axis.

the MOT cloud through an unused viewport in the MOT chamber, allowing the MOT to be directly observed as the laser frequency was adjusted. When the laser became resonant with a specific isotope and the MOT became visible to the CCD camera, the scan of the 672 nm laser was started. As the 672 nm laser was scanned (typically up to 3.5 GHz with no mode hops), the MOT as seen by the CCD camera would 'flash' as the 672 nm laser swept over resonance with the isotope in question. This was done without altering the starting frequency of the 672 nm laser in any way for ^{40,42,44}Ca, but to detect ^{48}Ca, the starting frequency had to be adjusted such that ^{44}Ca and ^{48}Ca could be detected in a single scan. This is important as detecting a single isotope per scan is meaningless. For anything meaningful to be taken from a measurement, at least two isotopes must be visible on the same scan. This is simply because the value we are looking for is the difference between set isotopes.

The centres of each MOT signal peak are then determined by fitting a Lorentzian lineshape to each one. These are then compared to each other and to the frequency calibration axis obtained from the high finesse cavity transmission peaks to determine the difference in frequency between each isotope. A sample result

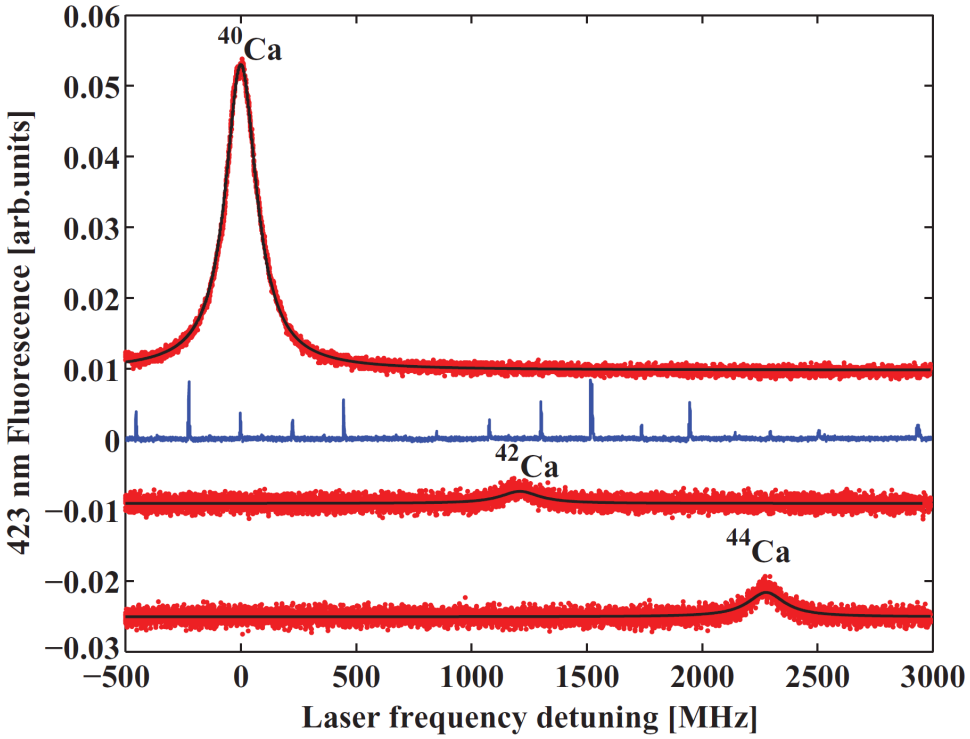

Figure 3.20: Sample isotope shift data for ^{40,42,44}Ca. ^{48}Ca is not shown. The black curves are Lorentzian fits with 80-90 MHz linewidths. Also shown is a typical set of the high finesse cavity transmission peaks. The isotope data sets are all offset from each other for the sake of clarity.

of this is shown in Fig. 3.20.

3.4.3 Results

Some values for the ^{40}Ca - ^{42}Ca IS are shown in Table 3.2 along with the average result. The values obtained for the isotope shifts on the $4s3d\,^1D_2 - 4s5p\,^1P_1$ transition at 672 nm are shown in Table 3.3. The values for ^{41,43,46}Ca are estimates based upon the measured values for the other isotopes.

As a simple means of proving that our values are consistent with expectation, it is possible to plot the values of the isotope shifts on one transition, with well known values [77], against the values we have obtained for the isotope shifts on the $4s3d\,^1D_2 - 4s5p\,^1P_1$ transition. As we are simply measuring the same thing

Isotope Shift (MHz)
1172
1173
1190
1181
1182
1190
1183(3)

Table 3.2: Isotope shift values for ^{40}Ca - ^{42}Ca and the resulting average.

Isotope Pair	Isotope Shift (MHz)
40-42	1181(3)
40-44	2268(3)
40-48	4239(9)
42-44	1087(4)
44-48	1971(9)
40-41	620(1)
40-43	1755(2)
40-46	3298(3)

Table 3.3: Isotope shift values for ^{40}Ca-^{42}Ca, ^{40}Ca-^{44}Ca, ^{40}Ca-^{48}Ca, ^{42}Ca-^{44} and ^{44}Ca-^{48}. Values for ^{40}Ca-^{41,43,46} are estimated values based on the measured values of the others.

on two different transitions, the values should vary proportionally. This can be seen in Fig. 3.21.

For a more thorough proof, we make a King plot [83] whereby the modified isotope shifts are plotted against the modified change in the root mean square (RMS) charge radii from one isotope to another. This is shown in Fig. 3.22. From the linear fit to the data we obtain a specific mass shift of $M_{SMS} = 774.0(0.7)$ GHz a.m.u. from the point at which the fit crosses the x-axis zero and field shift component $F_{FS} = -149.3(7.1)$ MHz/fm^2 from the slope of the fit. The values for the difference in RMS charge radii are obtained from [87].

While it was not possible to observe some of the other isotopes such as ^{43}Ca with natural abundance of 0.135% or ^{46}Ca with natural abundance of 0.004%, their isotope shifts, as well as for that of ^{41}Ca could be estimated based on the values obtained from the other isotopes. The relatively abundant ^{43}Ca isotope

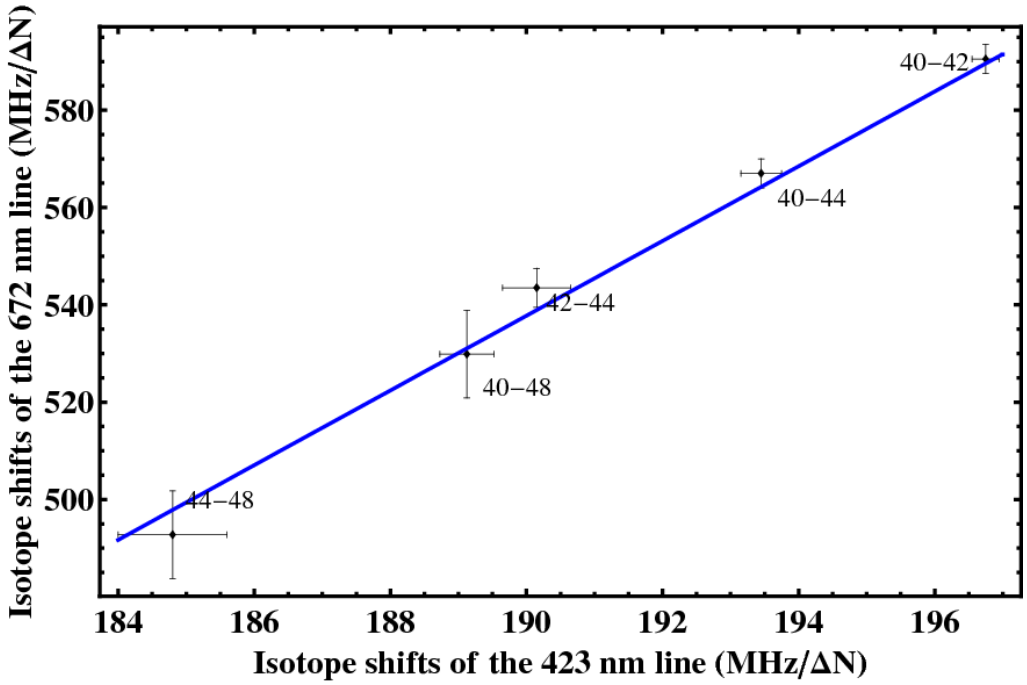

Figure 3.21: Simple plot of the IS values on the 423 nm transition against the 672 nm transition. Errors and values for the x-axis from [77], errors on the y-axis from this work.

could not be observed because, owing to having a nuclear spin of $I = 7/2$, there are a number of hyperfine structure levels to pump, meaning that the laser cannot interact with all 0.135% of the atoms which are ^{43}Ca at once [81]. ^{46}Ca could not be observed simply because its natural abundance is too low. Consider that its abundance is almost a factor of 50 lower than that of the next least abundant isotope detected in this work, ^{48}Ca. Consider Fig. 3.16. The lowest abundance isotope in this figure is ^{42}Ca, with abundance 0.647%. We can successfully detect ^{48}Ca, which has less than 1/3 of this natural abundance, with 0.187% of all calcium atoms being ^{48}Ca. Trying to see something 50 times less abundant than this and more than 150 times less abundant than ^{42}Ca is just not possible with the current setup. Perhaps more success could be had here if there were more atoms trapped in an average MOT to begin with.

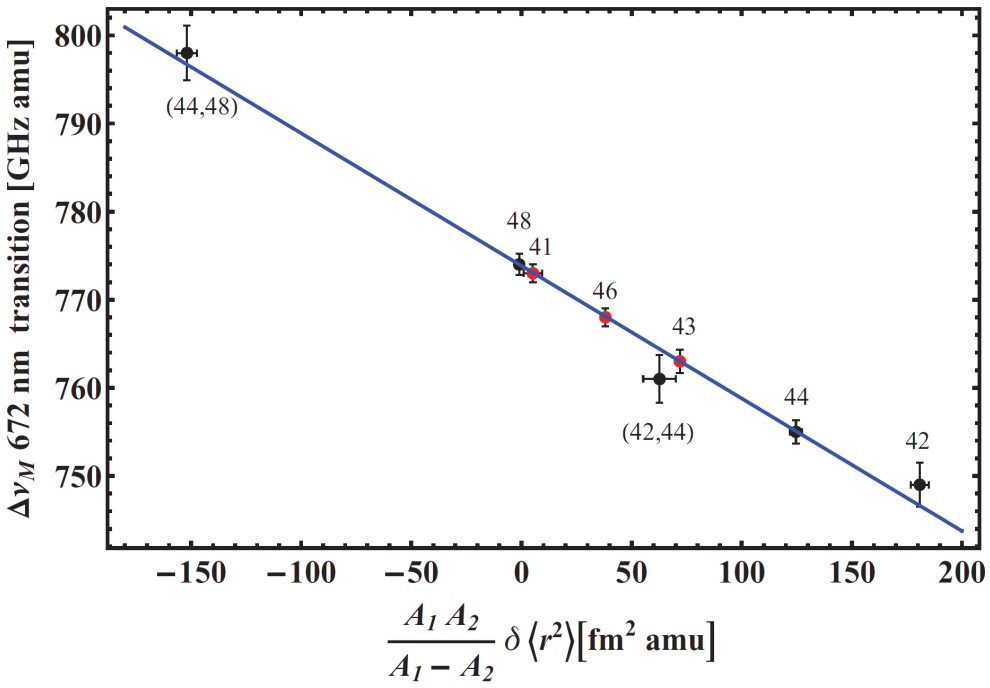

Figure 3.22: King plot for the 672 nm repump transition. The modified isotope shifts ($\Delta\nu_M^{A_1A_2}$) are plotted against the modified difference in root mean square (RMS) nuclear charge radii ($\frac{A_1A_2}{A_1-A_2}\delta\langle r^2\rangle^{A_1A_2}$) of the calcium isotopes. The specific mass shift MSMS and the field shift FFS of the $4s3d\,{}^1D_2 4s5p\,{}^1P_1$ transition at 672 nm are determined from a linear regression analysis, which is shown as a solid line. The points relating to the 42, 44, and 48 are the experimental data while those relating to isotopes 41, 43, and 46 are the estimated centres of gravity.

3.5 Conclusions

As a summary, in this chapter I have explained the 672 nm repump transition in magneto optically trapped calcium, including measurements made on several isotope shifts. The 672 nm repump laser provides more than an order of magnitude increase in the number of detected trapped atoms as a combination of three things. These are the improvements in MOT lifetime, extra atoms pumped out of the ${}^1D_2$ level and an improvement in the MOT loading rate. The rate equation model used to describe this system, however, cannot account for the experimentally derived values for these factors due to poorly known transition strengths.

However, one need simply look at the experimental data, e.g. Fig. 3.15, to determine that the experimentally derived parameters reflect the MOT characteristics.

Isotope shifts for three even isotopes have been presented, along with expected values for three other isotopes. An order of magnitude increase in the number of trapped atoms will be of great use to those groups attempting to detect, capture and make use of ^{41}Ca.

Chapter 4

Effects of the 1530 nm repump transition

This chapter is based in part on [47] *and extends the work.*

4.1 Introduction

One of the prime areas of research in the calcium MOT experiment has been to investigate the effects of various repump transitions to improve various characteristics of the MOT, be they the number of trapped atoms, the trap lifetime, or simply to 'plug' any leaks from the cooling cycle. The effects of the repump transition $4s3d\,^1D_2 - 4s5p\,^1P_1$ at approximately 672 nm were explained in the previous chapter. It is the repump transition $4s4p\,^3P_2 - 4s3d\,^1D_2$ at 1530 nm that is of primary interest in this chapter. More specifically, what effects power has on various aspects, investigable due to the acquisition of a fiber amplifier specifically designed for this wavelength.

The expected effects are similar to those seen in the previous chapter: an increase in the number of trapped atoms when the 1530 nm laser is on resonance with the $4s4p\,^3P_2 - 4s3d\,^1D_2$ transition.

4.2 Effects of the 1530 nm repump laser on MOT population

4.2.1 1530 nm laser only

As explained in Chapter 2, the main cooling transition used in this experiment, the $4s^2\,{}^1S_0 - 4s4p\,{}^1P_1$ at 423 nm, is not a completely closed transition. About $1:10^5$ atoms decay to the $4s3d\,{}^1D_2$ state. From there, atoms can then decay to the upper two fine structure levels of the $4s4p\ {}^3P$ state with a branching ratio of 1:5 in favour of the $4s4p\ {}^3P_1$ state [43]. Atoms that decay to the ${}^3P_1$ state then decay back to the ground state and rejoin the cooling cycle in approximately $0.4\,ms$. However, those which decay into the ${}^3P_2$ state, which has a lifetime of 118 minutes [57], are effectively lost from the cooling cycle.

For this experiment the laser source is a commercially available butterfly configuration 1530 nm distributed feedback (DFB) laser (QPhotonics QDFBLD-1530-20) which emits a maximum of 20 mW out of a single mode fiber. The laser is temperature tuneable (0.1 nm/K) over a few nanometers without any mode hops. When observed with a Fabry-Pérot cavity and driven by a suitably quiet power supply has a linewidth of 10(1) MHz and a frequency drift of less than 20 MHz per hour. The laser current is driven by a Thorlabs current controller (LD1255R) in the same configuration as in Chapter 3 and the temperature is controlled by a temperature controller (Wavelength Electronics FPT-4000).

This laser is directed towards the MOT and aligned by co-propagating it with the 672 nm repump laser. When it is resonant with the $4s4p\,{}^3P_2 - 4s3d\,{}^1D_2$ transition and the 672 nm laser is blocked, an increase in the number of trapped atoms was expected as this should have the same effect on the leak into the ${}^3P_2$ state as the 672 nm laser had on the leak into the ${}^1D_2$ state. The expected increase in MOT population is not detected, however. Instead, a reduction of the MOT population of $\sim 20-30\%$ is observed with a 1530 nm beam power of 12-13 mW.

Why should this be the case? Ideally, if the 1530 nm laser is on resonance with the ${}^3P_2 - {}^1D_2$ transition, an increase in the 423-nm fluorescence is (perhaps naively) expected as the leak out of the system is plugged. Instead, about a 30%

decrease in the 423 nm MOT fluorescence is observed. This is due to the fact that, in the central region of the MOT addressed by the 1530 nm laser, the density of atoms in the $^1D_2$ state is significantly higher than in the $^3P_2$ state and hence stimulated emission to the lower state becomes the dominant effect. This density difference is a consequence of how the atoms behave in the the different states. When the atoms decay to the $^1D_2$ state from the $^1S_0 - ^1P_1$ MOT, they are loaded into a volume comparable to the size of the MOT. The $^1D_2$ atoms are immediately addressed by the 1530 nm laser and will only expand a few millimeters in the lifetime of that state. However, once atoms enter the metastable $^3P_2$ state, they are not confined to the MOT region but expand according to the MOT quadrupole magnetic field. One magnetic sublevel ($m_J = 0$) is unaffected by this potential, while two are antitrapped and two are trapped. This is important later, when the rate equations used to model this system are introduced.

To best explain the populations of the relative levels, a rate equation model was designed around a five level system, with the levels labeled as follows: $^1S_0$ is level 1, $4s4P^1P_0$ is level 2, $4s3d^1D_2$ is level 3, $4s4p^3P_2$ is level 4 and $4s5p^1P_1$ is level 5. The rate equations that follow describe the spontaneous and driven transitions between them and decays out of the system.

The rate equations are as in Chapter 3, but with extra parameters in order to take the 1530 nm laser into account:

$$\dot{N}_1 = R - L(\Delta, I)(N_1 - N_2) + \Gamma_{21}N_2(1-\varepsilon) \times \Gamma_{31}N_3 + (\Gamma_{51} + \alpha\Gamma_{54})N_5, \quad (4.1a)$$

$$\dot{N}_2 = L(\Delta, I)(N_1 - N_2) - (\Gamma_{21} + \alpha\Gamma_{23})N_2 + \Gamma_{52}N_5, \quad (4.1b)$$

$$\dot{N}_3 = \Gamma_{23}N_2 - (\Gamma_{31} - \Gamma_{34})N_3 + \Gamma_{53}N_5 - \Gamma_{r1}(N_3 - N_5) - \Gamma_{r2}\gamma(t)(N_3 - \beta_1 N_4), \quad (4.1c)$$

$$\dot{N}_4 = \beta_2[\Gamma_{34}N_3 + \Gamma_{53}N_5(1-\alpha)] + \Gamma_{r2}\gamma(t)(\beta_2 N_3 - \beta_1 N_4), \quad (4.1d)$$

$$\dot{N}_5 = \Gamma_{r1}(N_3 - N_5) - (\Gamma_{51} + \Gamma_{52} + \Gamma_{53} + \Gamma_{54})N_5, \quad (4.1e)$$

$$(4.1f)$$

where

$$L(\Delta, I) = \frac{s\Gamma_{21}}{2[1 + s + (2\Delta/\Gamma_{21})^2]} \tag{4.2}$$

is the drive term of the 423 nm main cooling transition, Γ_{r1} and Γ_{r2} are the drive terms for the 672 nm and 1530 nm transitions, respectively, $\gamma(t)$ is a top hat function representing the temporal structure of the 1530 nm laser pulse in relation to the MOT, β_1 accounts for the fact that only a fraction of the $^3P_2$ atoms interact with the 1530 nm laser at any given time and is typically $\sim 1\%$. This arises from an analysis of the volume of the trapped atoms and the proportion of this that the laser interacts with. If the radius of the cloud is obtained by solving $\frac{1}{2}k_BT = \Delta z \frac{dB}{dz} g_J m \mu_B$ for δz and using the MOT field gradient 32 G/cm for $\frac{dB}{dz}$, and compared with the expected volume covered by the laser beam, a value of $\beta_1 \approx 1\%$ is obtained. β_2 accounts for the fact that only a fraction of the $^1D_2$ atoms decay to a trapped sublevel of the $^3P_2$ state. Assuming an equal population of each of the five sublevels, we can assume this to be ~ 0.4. This is an oversimplification, however as atoms pumped into the $^1D_2$ from the $^3P_2$ have varying probabilities of pumping into a trapped state depending on their own initial sublevel. $s = \frac{I}{I_{sat}}$ is the saturation intensity of the $^1S_0 - ^1P_1$ transition. From the literature [47], $\Gamma_{21} = 2.18 \times 10^8 s^{-1}$, $\Gamma_2 = 2180 s^{-1}$, $\Gamma_{31} = 700 s^{-1}$, $\Gamma_{34} = 96 s^{-1}$, $\Gamma_{51} = 2.61 \times 10^5 s^{-1}$, $\Gamma_{52} = 2.13 \times 10^6 s^{-1}$, $\Gamma_{53} = 1.21 \times 10^7 s^{-1}$ and $\Gamma_{54} = 3.4 \times 10^5 s^{-1}$. See Fig. 2.1 in Chapter 2 for the relevant calcium energy levels. It is worth pointing out that a steady state analysis of these rate equations shows that at any given time, there are roughly one third of the total number of atoms in the system in the $^1D_2$ when only the 423 nm beams are on.

Taking Equation 4.1a as an example, it can be seen that the change in population of the level depends upon the rate at which atoms are loaded into the MOT (R), the initial populations of state 1, 2, 3 and 5 ($N_{1,2,3,5}$), the decay rates from state two, three and five to various other states ($\Gamma_{21,31,51,54}$), any small fraction that decays to the $^3P_1$ state but is lost before decaying to the ground state (ε) and those atoms which decay to the ground state from the $4s5p\,^1P_1$ via a higher

lying triplet scheme (α). It should be fairly obvious that any term in an equation that refers to state 5, be they excitations to or decays from, can be set to zero when the 672 nm laser is off.

It should be noted, however, that some of these decay rates - particularly the smaller ones - are not known accurately. For example, the value used here for Γ_{31} is $\sim$ 2 times larger than appears in the literature, but is based upon experimental lifetime of the $^1D_2$ state reported in [76] and the 423 nm MOT lifetime measurements [48].

It should also be noted that these rate equations are not perfect. For one thing, they only consider 5 levels when there are obviously more. Another thing is that coherences relating to 3 level systems (such as a two photon transitions directly from level 4 to level 5 are not included and the model is run with any three level systems treated as two separate two level systems. However for a three level system the contribution of a coherence goes as [88]

$$\frac{\gamma_2}{\gamma_{31}} = \frac{\mathrm{life-time of coherence}\rho_{31}}{\mathrm{life-time of population}\rho_{22}}. \tag{4.3}$$

As the lifetime of the intermediate state (ρ_{22}) is long compared to the lifetime of the coherence, this will be negligible and is excluded from our model for this reason.

In the presence of the 1530 nm laser alone, a decrease in the 423 nm MOT fluorescence is observed. To fit the experimental data using the rate equation model, the parameter sets used are $L(\Gamma, I) = \Gamma_{21}/5.2$ (obtained from the MOT beam intensity and detuning and in agreement with the MOT lifetime data. At saturation intensity where s = 1 and with a detuning of half a linewidth, this should be $\Gamma_{21}/6$), $\beta_1 = 0.0074$, $\beta_2 = 0.4$, and $\Gamma_{r2} = 1.35\Gamma_{34}$ (value derived from the fit), respectively. The loading rate, R, is the scaling factor matching the signal amplitudes.

This loss from the MOT when the 1530 nm laser is resonant with the transition is shown in Fig. 4.1.

The following figures show how the rate equation model reacts to changes in various parameters, all of which serve to demonstrate the legitimacy of the actual

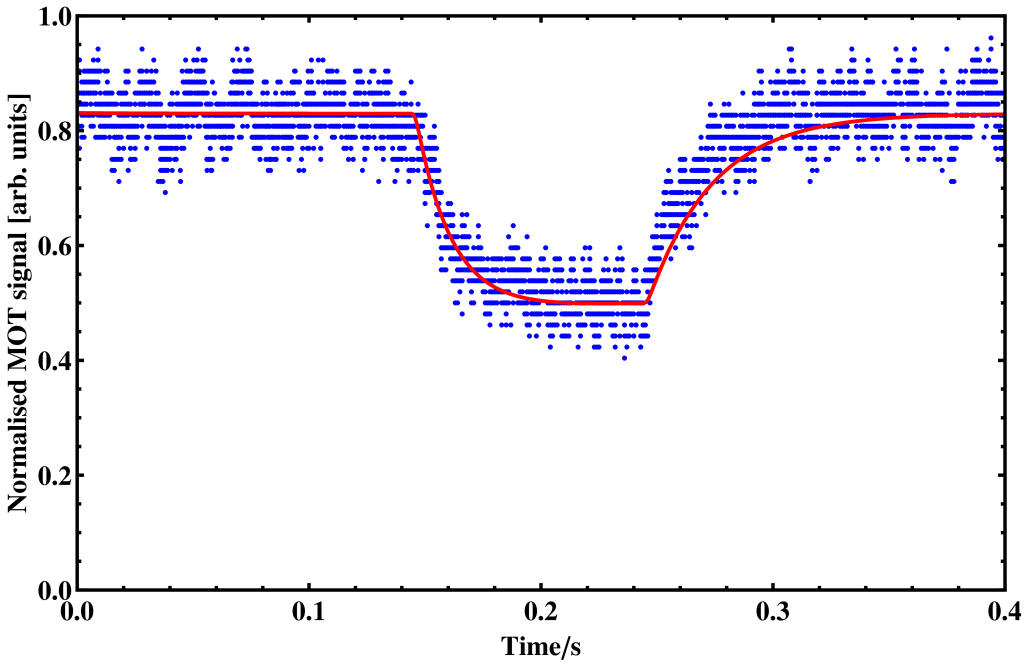

Figure 4.1: Resonance of the $4s4p^3P_2 4s3d^1D_2$ transition at 1530 nm observed as a decrease in the 423 nm MOT fluorescence (blue). The 423 nm MOT is operated continuously, while the 1530 nm is switched on only for 100 ms. The red curve is obtained from the rate equation model fit. The dip represents the 1530 nm laser being ON.

values used. Fig. 4.2 shows different values of β_1, showing that if we interact with more atoms (purple), we see less of a loss because more atoms are pumped out of the $^3P_2$ level. If we interact with less atoms, we see only marginally more loss from the system.

Fig. 4.3 shows differing values of β_2, showing that there is very little sensitivity to this parameter, as β_1 is dominant here, being only $\sim 1\%$. Any more atoms that would be pumped out due to a higher β_2 (green) are negated by the low β_1.

Fig. 4.4 shows different values of ε, the parameter which represents the fraction of atoms which decay to the $^3P_1$ state, but which do not decay to the ground state.

This is something of a curiosity as one would expect a higher value of ε, as used in the purple trace, would result in less atoms overall, and vice versa for a smaller value, as used for the green trace. In order to match levels, the filling rate, R, is varied in this instance, which leads to this seemingly odd result. the

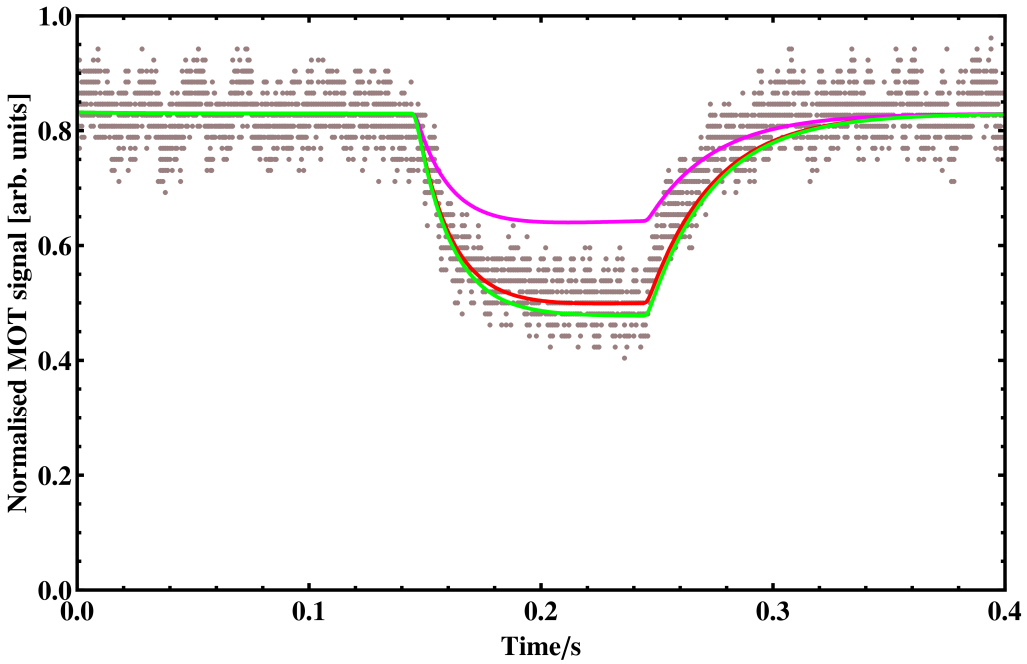

Figure 4.2: Using values of β_1 of 0.0078 (red), 0.078 (purple) and 0.00078 (green). It can be seen that if there is a greater overlap between the laser and the atoms, less atoms are lost due to the presence of the 1530 nm laser. It can also be seen that there is very little difference when interacting with fewer atoms.

interpretation of this, however, is quite simple: with a larger value for ε, more atoms are lost before the 1530 nm laser is turned on, meaning there are simple less atoms for the 1530 nm laser to interact with which results in there appearing to be less of an effect. The opposite is true of using a smaller value for ε.

Fig. 4.5 shows different values for the not particularly well known $^3P_2 - ^1D_2$ decay rate. For a higher decay rate, represented by the purple trace, the decay of the curve is faster, as expected. The same is true of the rate at which the trap repopulates after the laser is switched back off. The same holds for the green trace, which represents a lower decay rate and has a slower decay and refilling rate. This goes some way to vindicating the value of 96 s^{-1} from [55]

Fig. 4.6 shows the effects of different values of the 1530 nm laser drive term, Γ_{r2}. This shows that for a higher drive term, far more atoms are lost from the system as shown by the purple trace. Note also the fact that, while the decay rate

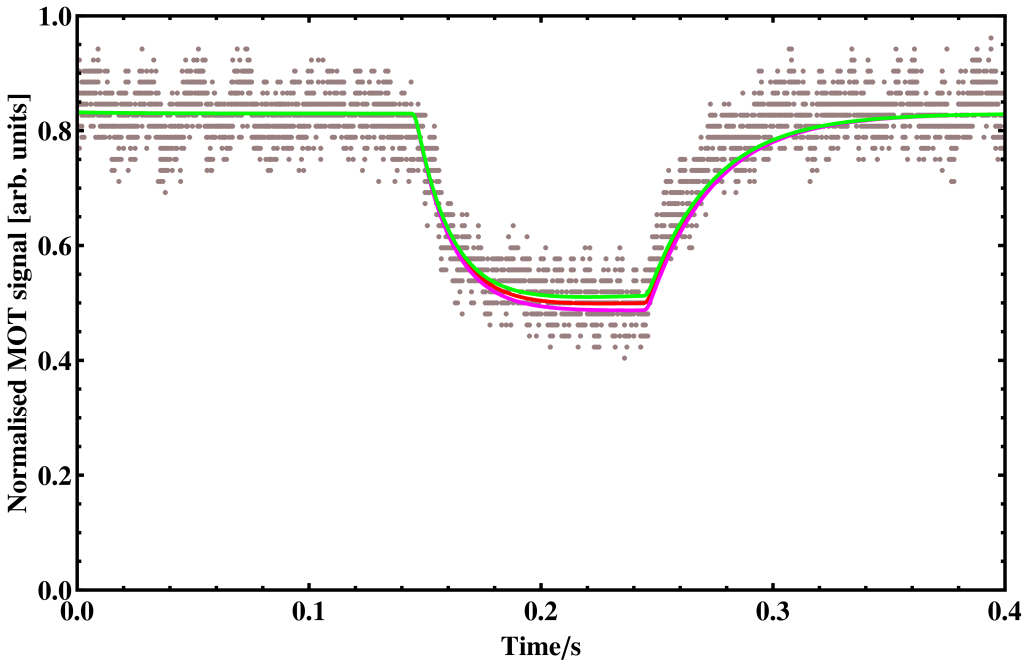

Figure 4.3: Using values of β_2 of 0.4 (red), 0.2 (purple) and 0.6 (green). Values are chosen to reflect different possibilities for sublevel filling.

is much faster than before, the rate at which the trap is repopulated is the same. This is obviously because the higher drive of the laser ceases to have any influence once it is switched off, leaving only the natural decay rate of the transition as the limiting factor. For a lower decay rate, fewer atoms are lost and the initial decay time is longer, as shown by the green trace. Again, note that the lifetime for the trap being repopulated is still the same as before. Figures 4.2 - 4.6 all serve to highlight the appropriateness of our chosen values for the constants. This graph does, however, highlight a shortcoming of the rate equation model. The purple trace in Fig. 4.6 suggests that applying more 1530 nm power results in losing a great deal more atoms from the trap, which is simply not borne out experimentally.

This loss of atoms is not what was expected or desired. The desired effect is to drive those atoms lost from the cooling cycle by way of entering the $^3P_2$ level back into the cooling cycle. To observe this, the $^1D_2$ state must be emptied so that the 1530 nm laser pumps atoms out of the $^3P_2$ rather than, effectively, the

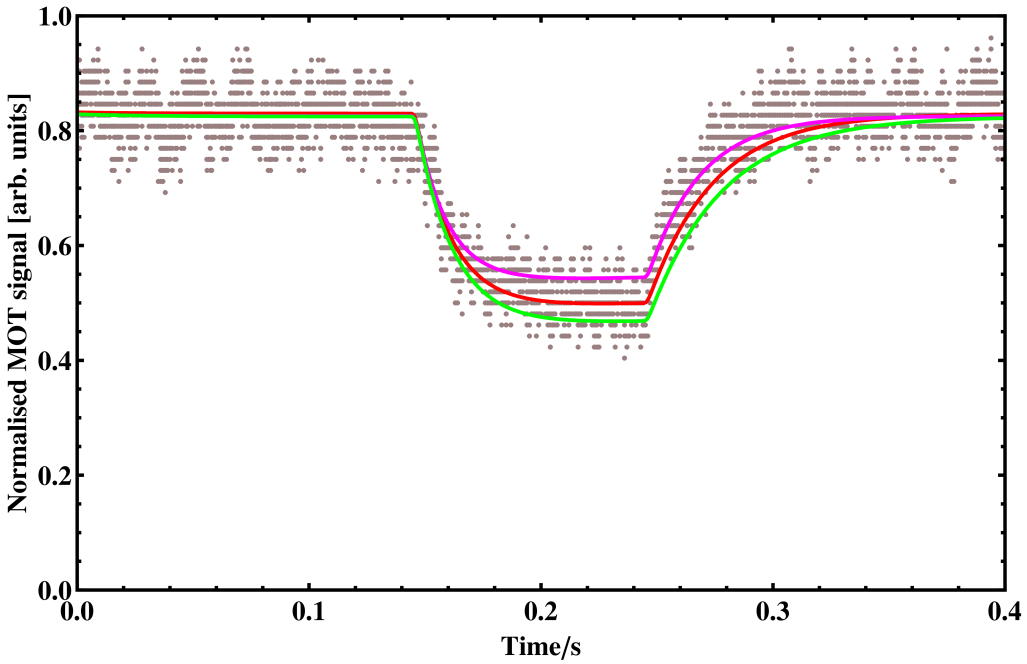

Figure 4.4: Using values of ε of 0.042 (red), 0.084 (purple) and 0.021 (green).

other way around. To this end the MOT beams are briefly extinguished to allow the $^1D_2$ atoms to spontaneously decay. This is done by way of gating various beams on and off to a specific timing which is shown in Fig. 4.7

For this procedure, the MOT was first loaded for 500 ms, followed by the beam providing the molasses being extinguished to prevent any additional atoms being introduced to the system. After this, the MOT beams are blocked for 20 ms to allow the $^1D_2$ state to empty. After this 20 ms window, the MOT beams are unblocked at the same time as the 1530 nm laser is introduced to the MOT region. The result of this is that with the $^1D_2$ state emptied before the 1530 nm laser is switched on, the only atoms which contribute to the fluorescence from the MOT are those which are pumped out of the $^3P_2$ state, shown in Fig. 4.8.

4.2.2 1530 nm and 672 nm lasers together

However, if the 1530 nm laser is used in conjunction with the 672 nm laser discussed in depth in the previous chapter, the $\dot{N}_5$ rate equation governing the

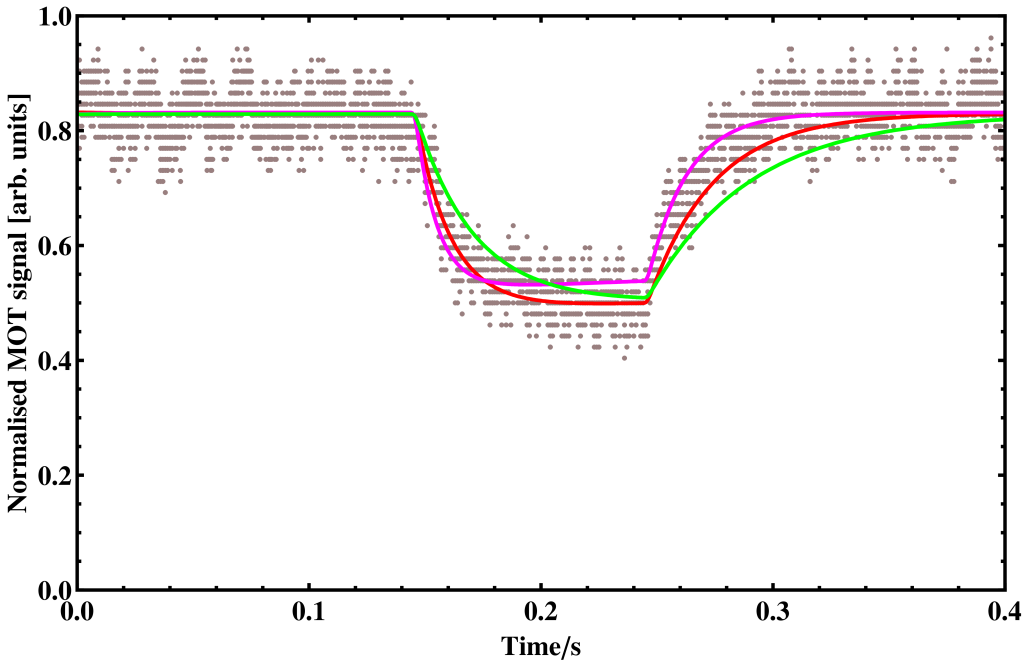

Figure 4.5: Using values of Γ_{34} of 96 s^{-1} (red), 192 s^{-1} (purple) and 48 s^{-1} (green).

$4s5p\,^1P_1$ level becomes important. This is obviously due to this level becoming part of the cooling cycle when the 672 nm repump laser is on resonance with the $4s3d\,^1D_2 - 4s5p\,^1P_1$ transition. As a result, the population of the $^1D_2$ state is effectively eliminated and the state lifetime becomes infinitesimally short. In this situation, the increase in detected MOT fluorescence, which was expected with the 1530 nm laser alone, is observed as seen in Fig. 4.9

This demonstrates the effectiveness of the dual repumping method. In Fig. 4.9, the signal before the presence of the 1530 nm laser is the magnitude of the MOT fluorescence signal in the presence of the 423 nm MOT beams and the 672 nm repump laser. This increase in the number of trapped atoms happens because the 672 nm repump laser effectively quenches the lifetime of the $^1D_2$ level and ensures that it remains empty of atoms. This being the case, atoms in the $^3P_2$ level can be pumped into it and them immediately on to the higher lying $4s5p^1P_1$ state, from which they promptly decay to the ground state via other excited states, as shown in Fig. 3.14 in the previous chapter. The net result of this is an increase

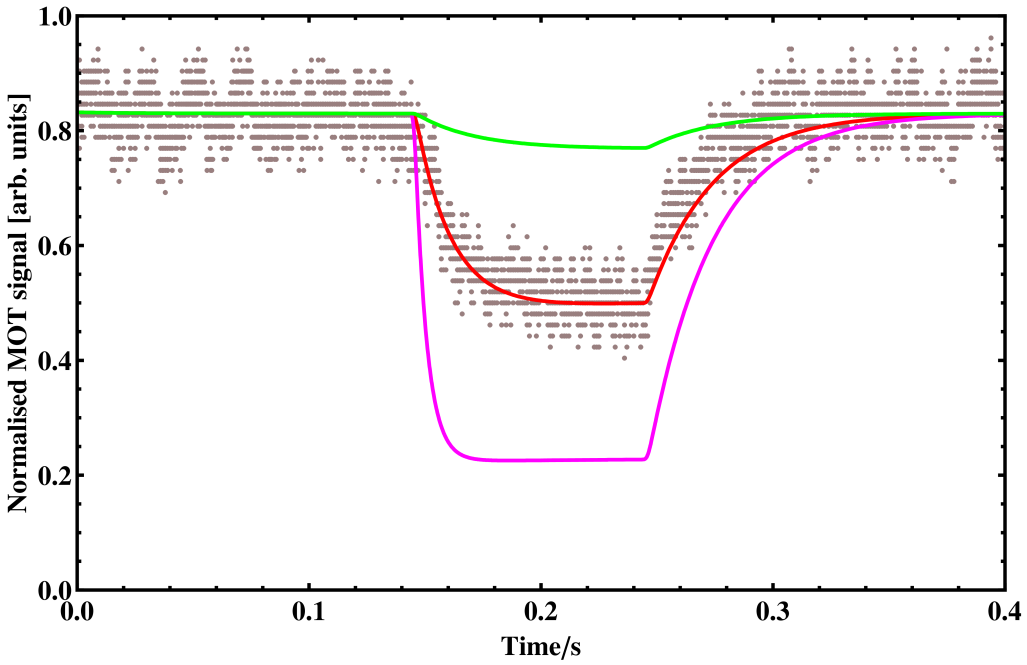

Figure 4.6: Using values of Γ_{r1} of 1.35 X Γ_{34} (red), 13.5 X Γ_{34} (purple) and 0.135 X Γ_{34} (green).

to about 10^7 atoms trapped in the MOT with both repump lasers on resonance.

As an added check, the rate equation model was once again tested using a number of different values for several constants and variables. Fig. 4.10 shows how the model is affected by differing values of β_1. Again, this makes sense as if more atoms are interacted with by the 672 nm laser (the purple trace in Fig. 4.10), we would expect to trap more atoms. The same is also true of a smaller interaction fraction providing less trapped atoms, as in the green trace. Fig. 4.10 also shows a marked increase in the number of initially detected atoms in the trap followed by a slow decay. This represents the fact that the atoms in the $^3P_2$ level are very quickly pumped into the cooling cycle then decay out, with no more 'extra' atoms being trapped.

Fig. 4.11 shows how the model reacts to different values of β_2. Fewer atoms are pumped out of the $^3P_2$ level due to a decreased sublevel (purple) while more are pumped out due to higher sublevel filling.

Fig. 4.12 shows how the rate equation model reacts to differing values of the

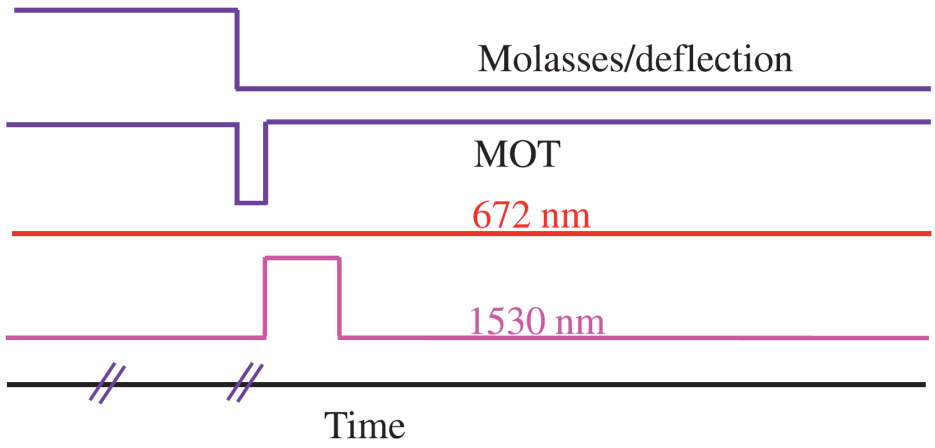

Figure 4.7: Pulse sequence of laser beams used for spectroscopy and for lifetime measurement of the magnetically trapped calcium atoms in the 3P2 state. The 423-nm MOT is loaded with the molasses laser beams switched on for 500 ms. The MOT beams are then gated off for a hold time varied from 100 to 1000 ms. The 1530-nm laser beam is switched on for 100 ms at the end of this hold time, enabling detection of the remaining metastable 3P2 atoms trapped in the magnetic quadrupole field of the MOT. The 672-nm laser remains off throughout this sequence.

$^3P_2 - ^1D_2$ decay rate, Γ_{34}. A higher decay rate sees a much steeper initial slope, but results in the atoms decaying from the trap much faster as well. A lower decay rate sees the opposite. This exact figure can also be produced by instead changing the 1530 nm drive term, Γ_{r2}, by the same magnitude as Γ_{34}. This is simply due to the fact that the stronger the decay rate, the higher the drive term has to be for the same effect.

Fig. 4.13 displays the changes in the rate equation fit due to different values used for the 672 nm laser drive term, Γ_{r1}. Once again, this makes sense as one would expect a higher drive term for the 672 nm transition (purple) would result in more atoms in the trap, and vice versa for a lower drive term, as seen in the green trace. While the 672 nm drive term has little effect on the time constant of the growth curve, the higher the drive term, the longer the decay time once the 1530 nm laser is switched off. Again, this is expected, as described in Chapter 3. It should be noted, however, that due to there being a finite number of atoms in

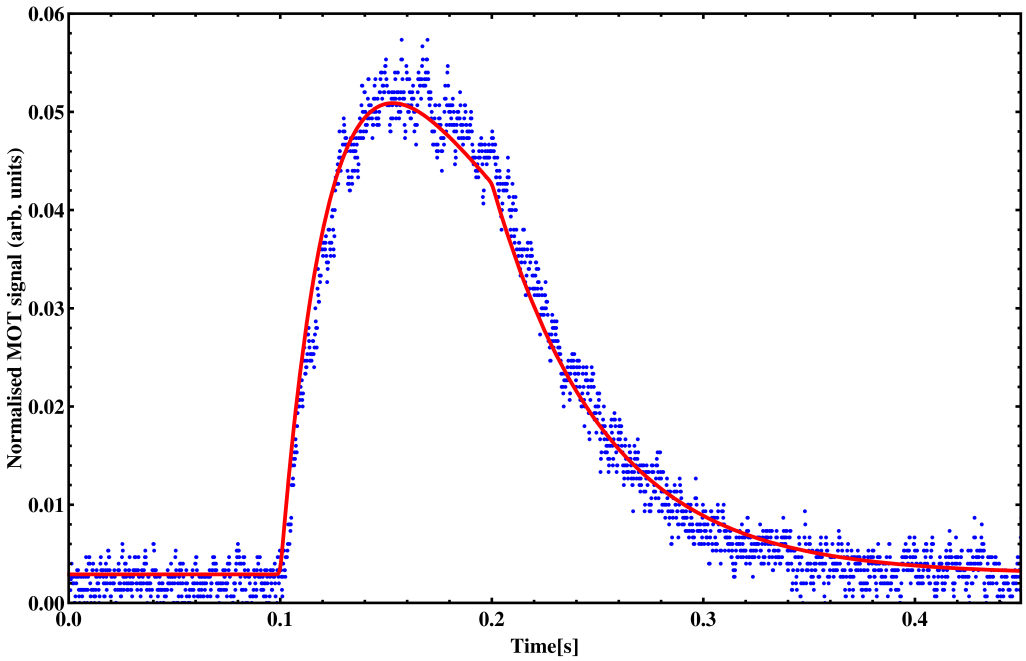

Figure 4.8: Detection fluorescence of atoms pumped out of the $^3P_2$ state during the gating in Fig. 4.7. The blue points are the experimental data, the red curve is a fit from the rate equation model. The y-axis is normalised to the peak MOT signal before the MOT beams are extinguished.

the trap and transitions saturate, simply putting in exceedingly high powers will not automatically result in more trapped atoms.

Again, figures 4.10 - 4.13 suggest that our regular values for the constants and some variables used in the rate equation model are consistent with what the experiment shows.

4.2.3 $^3P_2$ state lifetime

In order to measure the lifetime of atoms magnetically trapped in the in the $^3P_2$ state, the same timing sequence as before was used. The time between the MOT beams being extinguished and then turned on again in conjunction with the 1530 nm laser was increased sequentially up to 1 second. Following this, the 423 nm MOT fluorescence signal is integrated over the 1530 nm laser on-time after

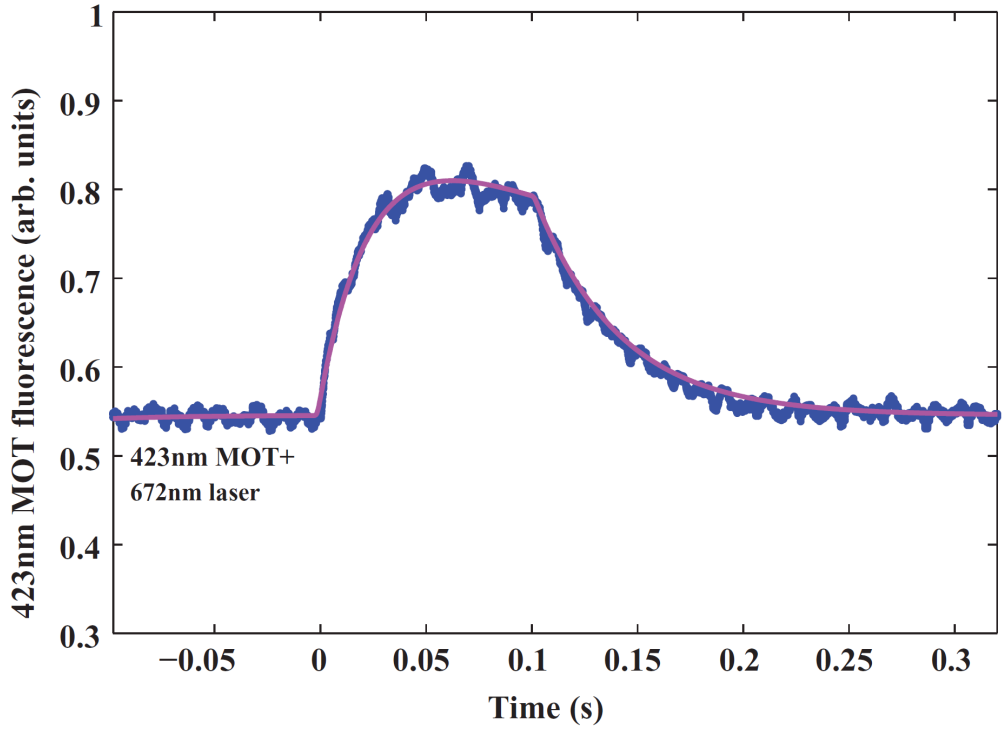

Figure 4.9: Increase in the 423-nm MOT fluorescence with a frequency stabilized 672-nm laser on resonance and with the 1530-nm laser pulse on.

subtraction of the effects of background light. The number of trapped $^3P_2$ atoms as a function of the delay between the MOT being extinguished and resumed, is shown in Fig. 4.14.

Fig. 4.14 shows a lifetime for the magnetically trapped atoms to be 928(78) ms. The variations in between individual data points are attributed to fluctuations in the MOT population due to the same in the 423 nm light used to generate it and drifts in the 1530 nm laser wavelength over time, which was not stabilised in any way. This figure also demonstrates that we successfully detected approximately 4.5 x 10^4 trapped $^3P_2$ atoms.

4.2.4 Wavelength measurement

It is worth noting briefly here that a precision measurement of the wavelength of the $4s4p^3P_2 - 4s3d^1D_2$ transition was made using a near-IR capable wavelength

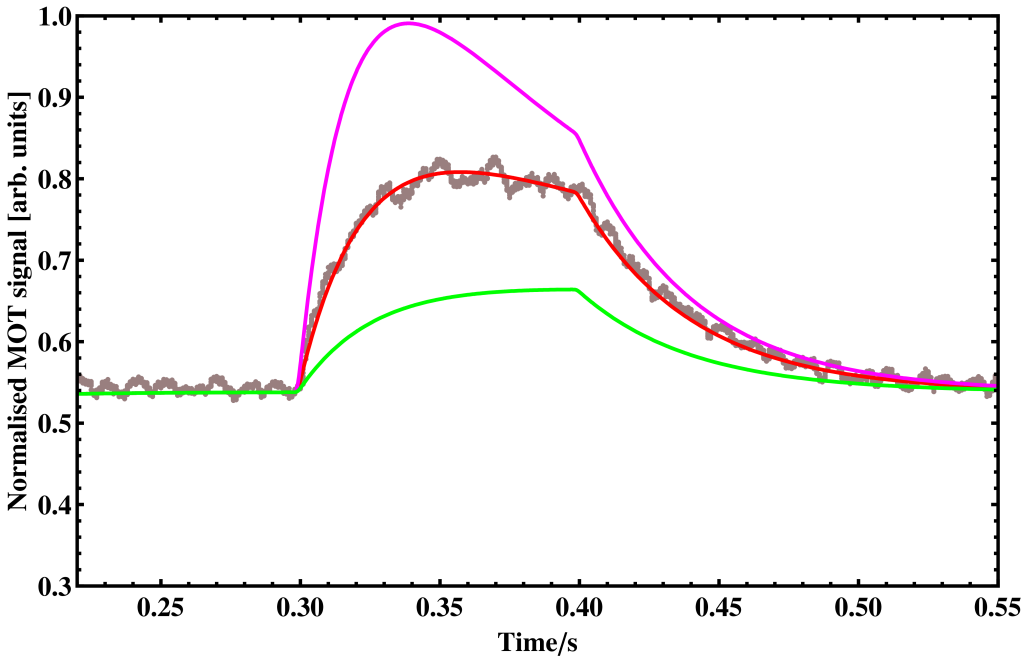

Figure 4.10: Using values for β_1 of 0.0074 (red), 0.148 (purple) and 0.0037 (green).

meter. The vacuum wavelength was found to be 1530.5298(6) nm, which is consistent with the value calculated from the known transition energies of the $^1D_2$ and $^3P_2$ states from the NIST database, 1530.53 nm [75].

However, in order to do this, the line had to first be located, which proved to be a laborious task. The laser temperature was adjusted to a temperature at which the line was expected to be found at a given current and then the current was slowly scanned back and forth over 100 seconds with a function generator producing a triangular wave.

The scan of the 1530 nm laser and the resulting dip in the MOT fluorescence signal can be seen in Fig. 4.15 along with the transmission through a Fabry-Pérot interferometer (FPI). This last step was included to ensure there were no mode-hops as the laser was scanned.

The fact that the feature representing the resonance with the transition is so much broader than either what was expected or the laser linewidth itself is attributed to several factors. First of all, the laser intensity for this particular

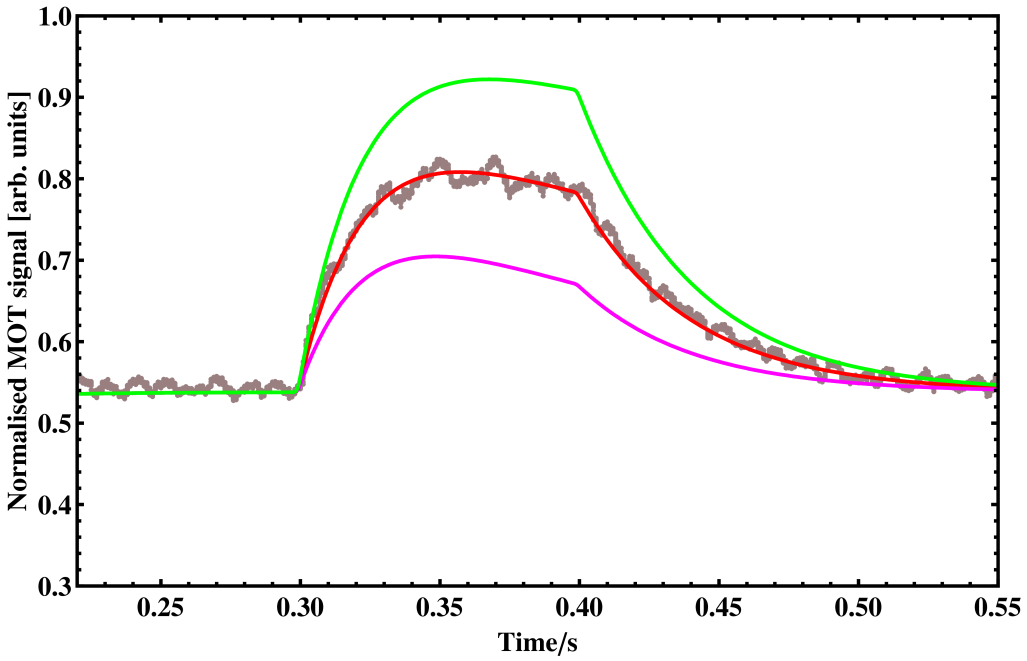

Figure 4.11: Using values for β_2 of 0.4 (red), 0.3 (purple) and 0.5 (green).

measurement (several kW/m^2) was several times greater than the saturation intensity of the transition ($5.5\mu W/m^2$). This causes power broadening, whereby [89]

$$\Gamma_{FWHM} = \Gamma(1 + \frac{I}{I_{Sat}})^{1/2}, \tag{4.4}$$

where Γ_{FWHM} is the power broadened full width at half maximum. It can be seen from Fig. 4.15 that the FWHM linewidth of the feature on the MOT signal due to the presence of the 1530 nm laser is approximately 30 MHz for the settings used (300 mW beam power). This seems rather large and will be discussed in greater detail later in this chapter.

As stated in Chapter 2, atomic energy levels shift in frequency in the presence of a magnetic field. When both levels contain magnetic sublevels as is the case with the $4s4p^3P_2$ and $4s3d^1D_2$, this manifests as a Zeeman broadening of the

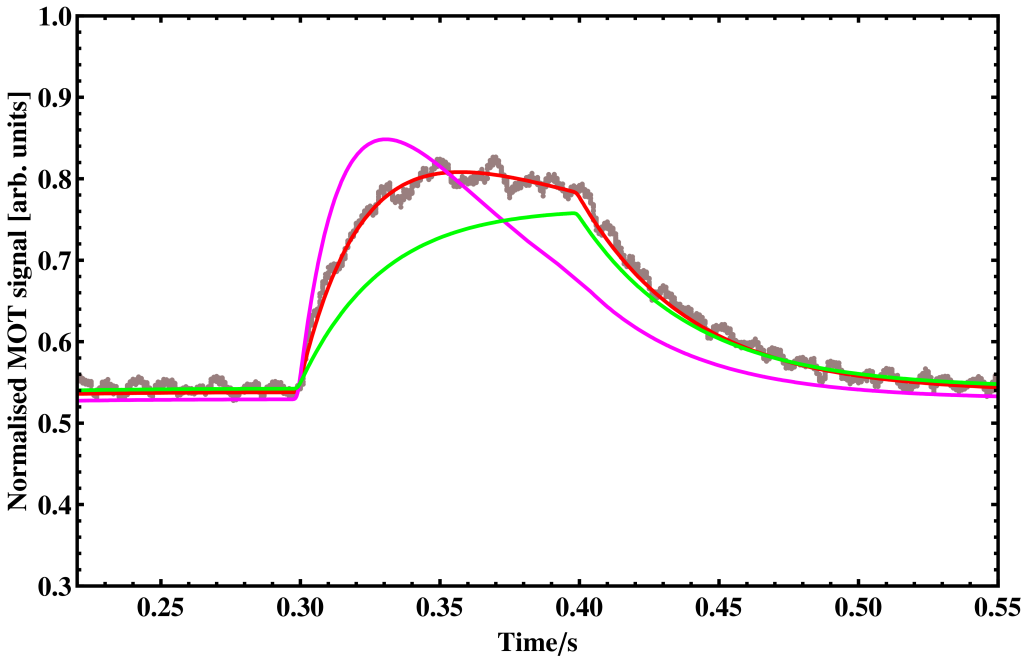

Figure 4.12: Using values for Γ_{34} of 96 s^{-1} (red), 192 s^{-1} (purple) and 48 s^{-1} (green).

transition in proportion to the magnitude of the magnetic field, on the order of 1.4 MHz/G.

A sample data set obtained when measuring the wavelength of the transition once it had been found is shown in Fig. 4.16

4.3 Effects of 1530 nm laser beam power

Following these measurements experiments were undertaken to determine the effects of 1530 nm beam power would have on the repump transition. To this end, use was made of a fibre amplifier (Keopsys KPS-CUS-BT-C-37-SLM-PM-111-FA-FA) capable of amplifying the output of the DFB to ∼4.5 W.

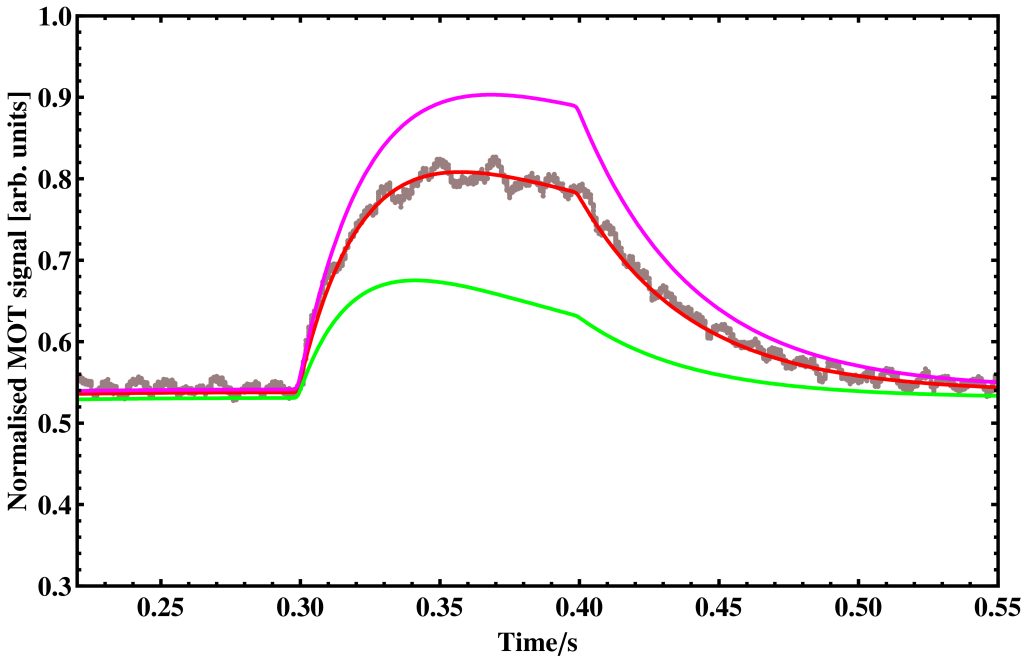

Figure 4.13: Using values for Γ_{r1} of $\Gamma_{53}/25$ (red), $\Gamma_{53}/12.5$ (purple) and $\Gamma_{53}/50$ (green).

4.3.1 1530 nm laser only

To begin with, the effects of the 1530 nm beam power on the 423 nm MOT alone were measured. That is, without the presence of the 672 nm repump laser on the $4s3d^1D_2 - 4s5p^1P_1$ transition. As stated before, with just the 1530 nm repump laser on, a loss of atoms in the MOT is detected. The purpose of this experiment was to determine what effect beam power has on the magnitude of this loss. For this experiment, the MOT was run as normal without the 672 nm repump laser and the 1530 nm laser power was increased incrementally. For each step, the MOT signal was recorded. Fig. 4.17 shows the size of the dip as a percentage of the original MOT signal as a function of beam power in the 1530 nm laser.

As can be seen, beyond a certain level, the power in the 1530 nm beam has little effect on the relative magnitude of the change in the MOT when it is on resonance. However, For these same measurements, the linewidth of the feature was also measured, resulting in Fig. 4.18

This shows that there is a clear effect of the power on the linewidth of the

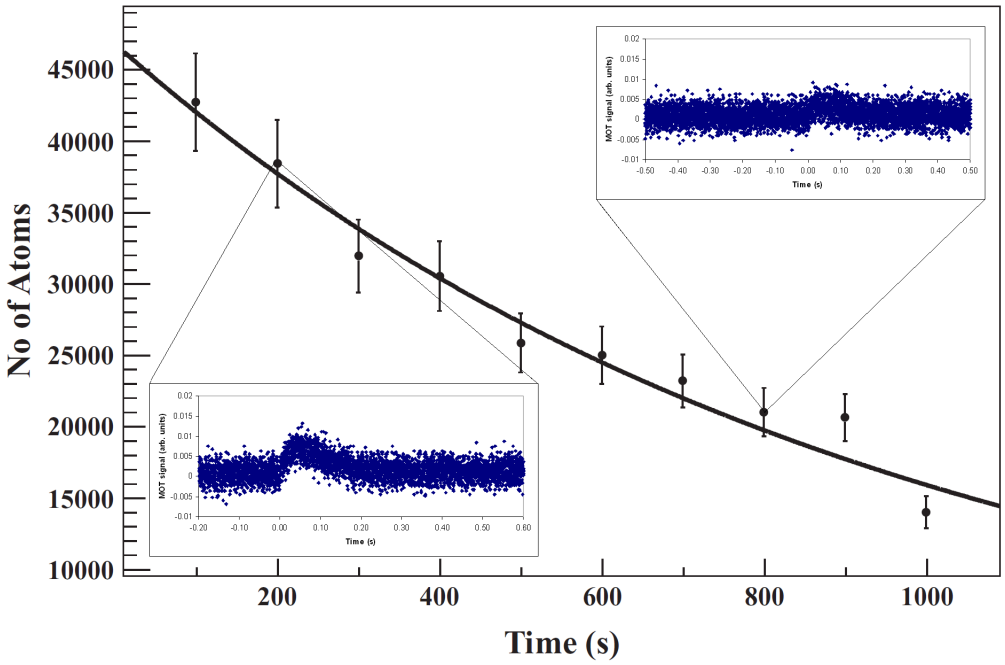

Figure 4.14: The number of atoms detected being pumped out of the $^3P_2$ level as a function of the time between the MOT being extinguished and resumed alongside the 1530 nm repumper. The solid line is the exponential fit to the data.

transition. However, it also shows linewidths which are orders of magnitude greater than would be expected for a typical intercombination line transition. This can be partly explained by Zeeman broadening of the transition, again on the order of 1.4 MHz/G. If the atoms in question were to inhabit an area around the trap centre that is 1 cm across, they would see a magnetic field of 32 G, leading to a broadening of approximately 45 MHz. However, as the laser beam size is less than this, only atoms which interact with the laser contribute to the broadening leading to the initial linewidth, approximately 30 MHz.

The discrepancy between the Lorentzian profile obtained from the rate equation model and the experimental data can be partially explained by this. At lower beam powers, the Gaussian profile of this Zeeman broadening is expected to dominate the linewidth, while at higher powers, the profile should more closely resemble a Lorentzian. A Voigt profile [90] is a mixture of Gaussian and Lorentzian lineshapes. A detailed description is unnecessary here, but it suffices to say that

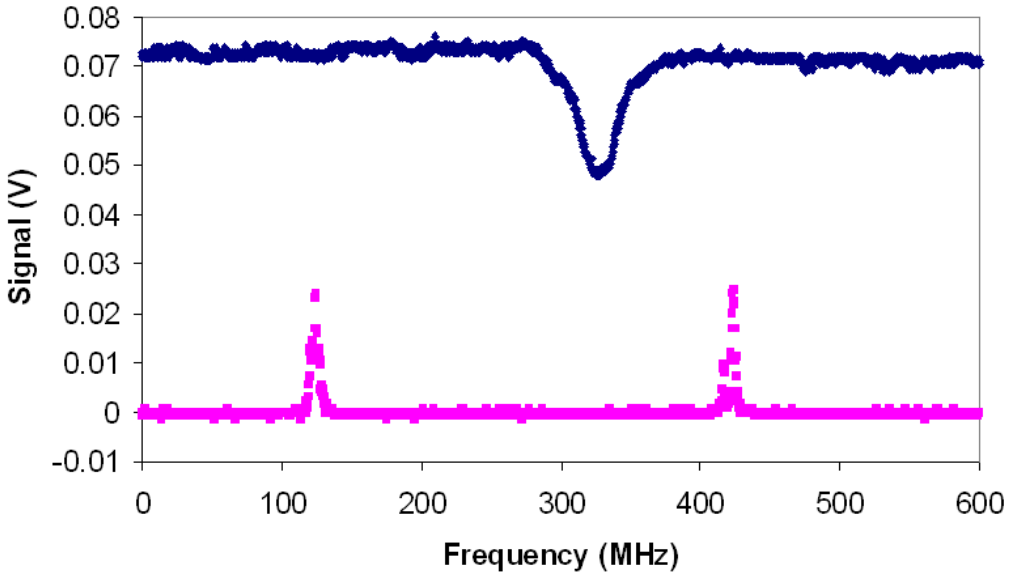

Figure 4.15: The scan on the 1530 nm laser. The blue trace represents the fluorescence signal from the MOT as the 1530 nm laser scans over the atomic resonance and the pink trace represents the 1530 nm transmission through an FPI.

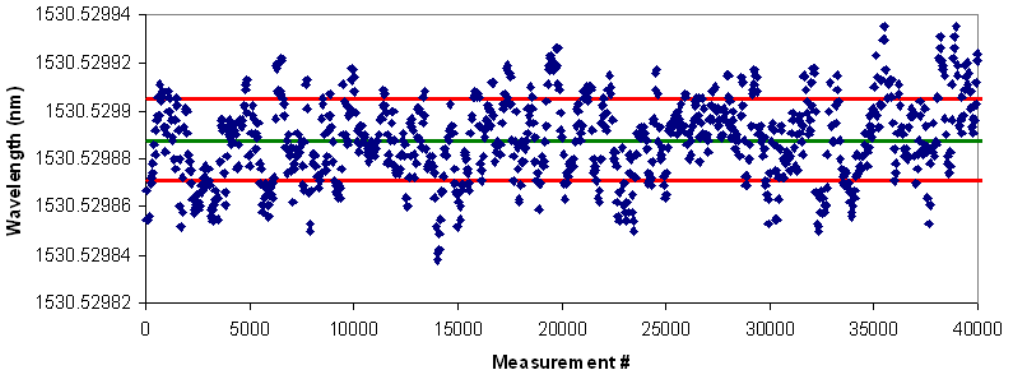

Figure 4.16: A raw data set of the wavelength meter showing the data points (blue), the mean wavelength observed (green line) and the standard deviation from the mean (red lines).

the FWHM linewidth of such a profile can be estimated as follows

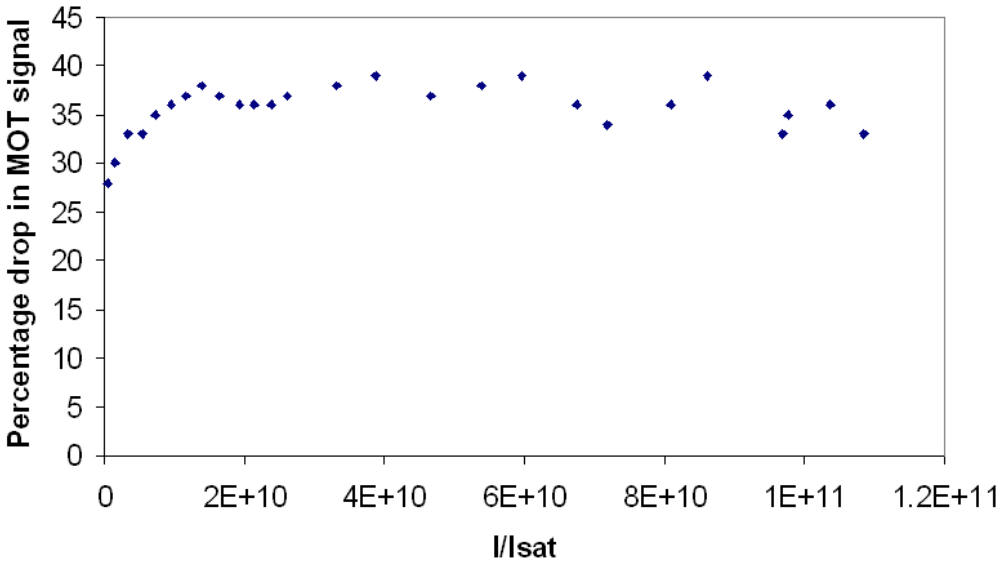

Figure 4.17: The magnitude of the signal lost from the MOT when the 1530 nm laser is on resonance as a function of 1530 nm beam power. It can be seen that there is an increase at lower powers, but once the power reaches ∼350 mW, this begins to saturate.

$$f_{Voigt} \approx 0.5346 f_L + \sqrt{0.2166 f_L^2 + f_G^2}, \tag{4.5}$$

where $f_{Voigt,L,G}$ are the Voigt, Lorentzian and Gaussian linewidths, respectively. Plotting the Voigt profile provides the green trace in Fig. 4.18. This provides a good fit a lower 1530 nm laser intensities if the fact that the linewidth of the amplified output increases by a factor of $\sim$ 3 from low power to high power. Further discrepancies also appear at higher intensities, down to the 1530 nm fiber amplifier not being particularly stable at higher settings. The intensity would fluctuate, for example. The Gaussian profile can be used here because we are dealing with a thermal distribution of atoms trapped in a harmonic potential.

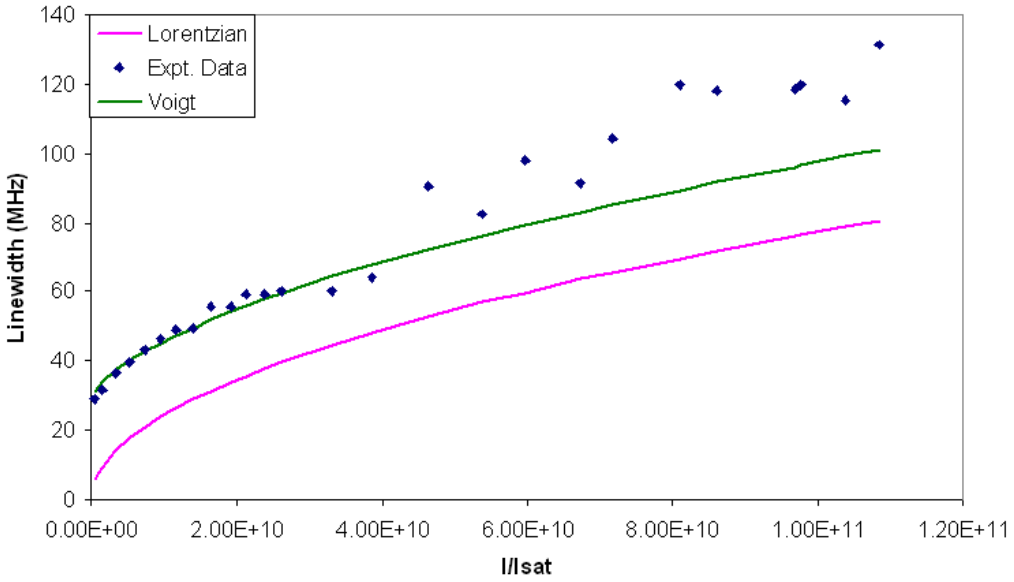

Figure 4.18: The spectral width of the 1530 nm feature as a function of the 1530 nm beam power. It can easily be seen from this that there is a power broadening effect. The blue points are the experimental data, the pink curve is the Lorentzian linewidth obtained by an analysis of the rate equations and the green curve is the Voigt profile (details in the text).

4.3.2 1530 nm laser and 672 nm laser

For this experiment, the MOT was run as normal, the 672 nm laser was run at a constant power of 15 mW and the 1530 nm laser was run at varying powers to gain a measure of how different powers affect the MOT while it is being repumped on the 672 nm line. The results showed that up to about 20 mW of 1530 nm power sees the number of trapped atoms increase to about 1.3 times the initial MOT level, beyond that power, there is very little noticeable difference to the MOT.

4.4 Effects of 672 nm laser beam power

With the effects of 1530 nm beam power investigated, it made sense to also see what effect differing powers in the 672 nm beam would have when the two lasers were on. Given that it has been shown earlier in this chapter that the 1530 nm

laser only has a beneficial effect on the number of trapped atoms when the 672 nm laser was also on, efforts were made to determine what was required of the 672 nm beam for this positive effect. For this experiment the 1530 nm laser was run at a constant power of ∼540 mW and the MOT was run as normal with the 672 nm laser locked on resonance at varying powers. The 1530 nm laser was then gated on and off for 1.5 seconds at a time and the change in the level of the MOT signal was observed. The results are shown in Fig. 4.19.

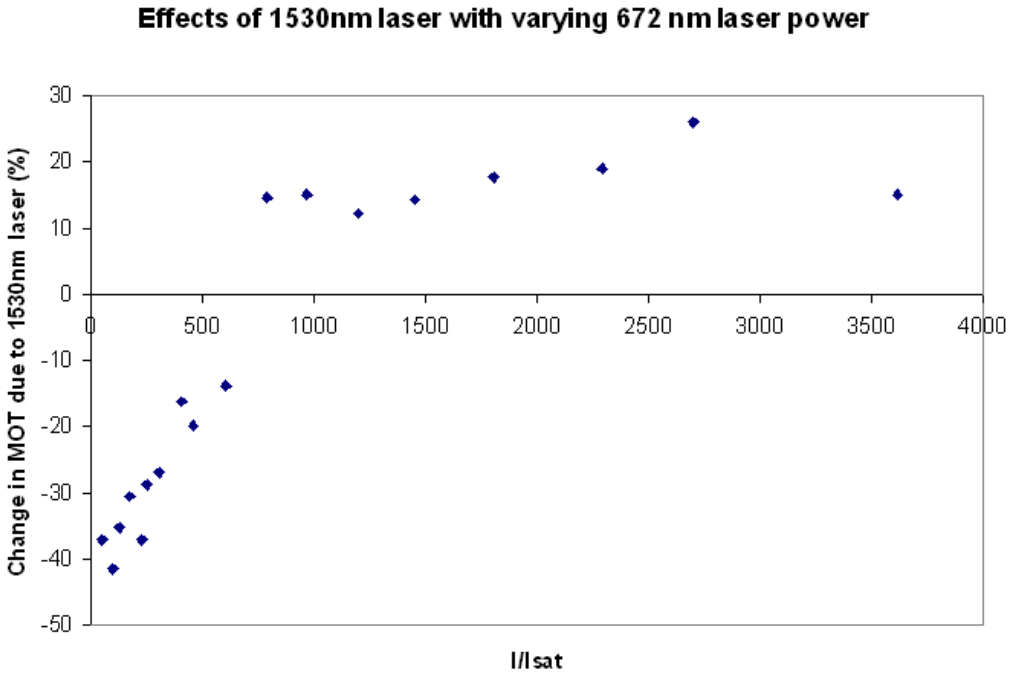

Figure 4.19: The effects of 672 nm laser beam power on the change in the level of the MOT signal caused by the 1530 nm laser. It can be seen that the positive effect starts to manifest almost immediately and appears to saturate at $\sim 700\frac{I}{I_{sat}}$.

This clearly shows that for the 1530 nm laser to have the desired positive effect on the MOT signal, the 672 nm laser not only has to be on, but also has to be of sufficient power. The point at which the data in Fig. 4.19 begins to saturate is with approximately 3-4 mW of power in the 672 nm laser.

4.5 Effects of frequency modulation of the 1530 nm laser beam

The final set of experiments performed with the amplified 1530 nm laser involved broadening the linewidth of the laser itself. It was theorised that, as the atoms in the $^3P_2$ state expand from the trap centre unmolested by the MOT beams, there would be a substantial Zeeman broadening of the transition in question. Thus, if the laser itself were broadened, the laser would be able to interact with more atoms. Three separate experiments were carried out in the following manner. First, the $^3P_2$ atoms were measured in much the same way as earlier in this chapter with a similar timing scheme and the 672 nm laser on and locked for increasing spectral widths of the 1530 nm laser. Secondly, this experiment was repeated, but with the 1530 nm laser power being increased along with the linewidth in order to keep the power spectral density constant. Finally, the first experiment was repeated with the 672 nm laser off.

4.5.1 Constant power, increasing linewidth

For the first experiment in this section the 1530 nm laser was frequency modulated at 1 MHz by way of a function generator (Agilent 33250A) and a bias tee. The amplitude of the modulation was varied from 0 mV up to 300 mV. The linewidth of the 1530 nm laser was increased in steps while the power was kept constant at approximately 70 mW (saturation parameter of 10^9. this is shown in Fig. 4.20.

A timing sequence similar to that used earlier in this chapter was used, only for this experiment the 1530 nm laser was gated on for 300 ms after the MOT beams had been gated off for 10 ms. The MOT beams were gated off 100 ms after the molasses beams were extinguished and were gated back on in time with the 1530 nm laser. Only the magnitude of the signal when the 1530 nm laser is on is taken into account in this case. This leads to the results seen in Fig. 4.21.

It can be seen from the above figure that simply increasing the linewidth of the 1530 nm laser has little to no impact on the laser's effect on the MOT signal.

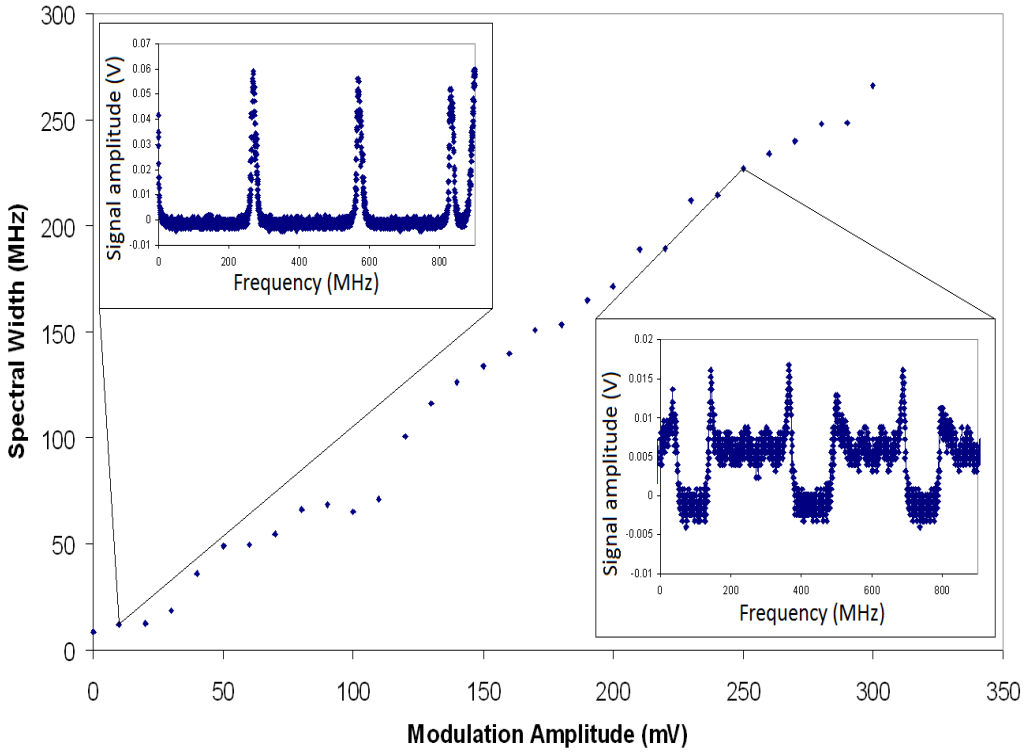

Figure 4.20: The effects of modulating the laser on the lasers linewidth. The curious lineshape at 250 mV is simply due to the frequency scan spending more time at either end of the range while it 'turns around'.

4.5.2 Constant power spectral density

Following this, the same procedure as before was followed, but this time the power of the 1530 nm laser beam was increased along with the linewidth. Earlier, by increasing the linewidth but keeping the power constant, the power in the beam ended up becoming spread out over the whole spectrum of the laser, dropping the power spectral density each time the linewidth was increased. By rasing the power together with the linewidth the power spectral density was kept at a constant 7.7 mW/MHz. The 7.7 mW corresponds to a saturation parameter of approximately 10^8. The results of this are shown in Fig. 4.22.

It can be seen from Fig. 4.22 that neither increased power nor increased linewidth have any noticeable effect on the observable effects of the 1530 nm laser with the 672 nm laser on resonance. The difference in signal between Fig. 4.21

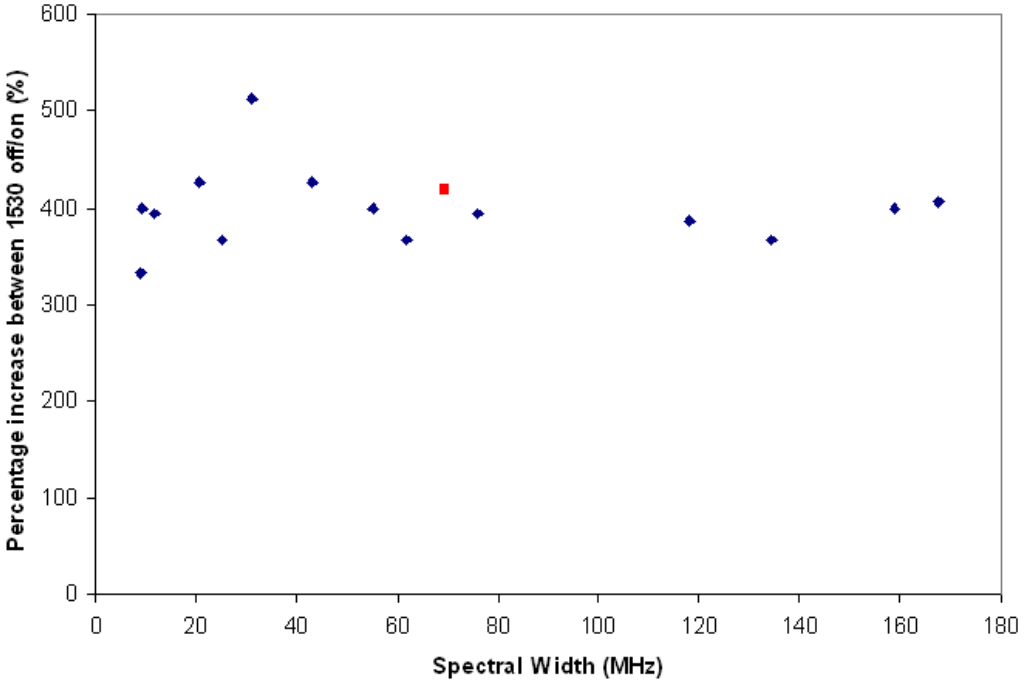

Figure 4.21: The effects of increasing linewidth of the 1530 nm laser on the MOT signal. It can be seen that there is little to no effect. The red data point corresponds to the red data point in Fig. 4.22.

and Fig. 4.22 is attributed to the fact that the experiments were run on different days and due to fluctuations in the overall MOT quality from day to day.

One final experiment was carried out, whereby the first experiment in this section was repeated with the 672 nm laser off.

4.5.3 Constant power, no 672 nm laser

For this final experiment, the only change to the first one in this section was to run without the 672 nm laser on. This removes its effects from the system and allows us to determine what effect the 1530 nm laser has on the trapped $^3P_2$ atoms when it is broadened by frequency modulation. The results are shown in Fig. 4.23

It can be seen from the above figure that the linewidth of the 1530 nm laser has very little effect on the number of $^3P_2$ atoms trapped, above a certain threshold.

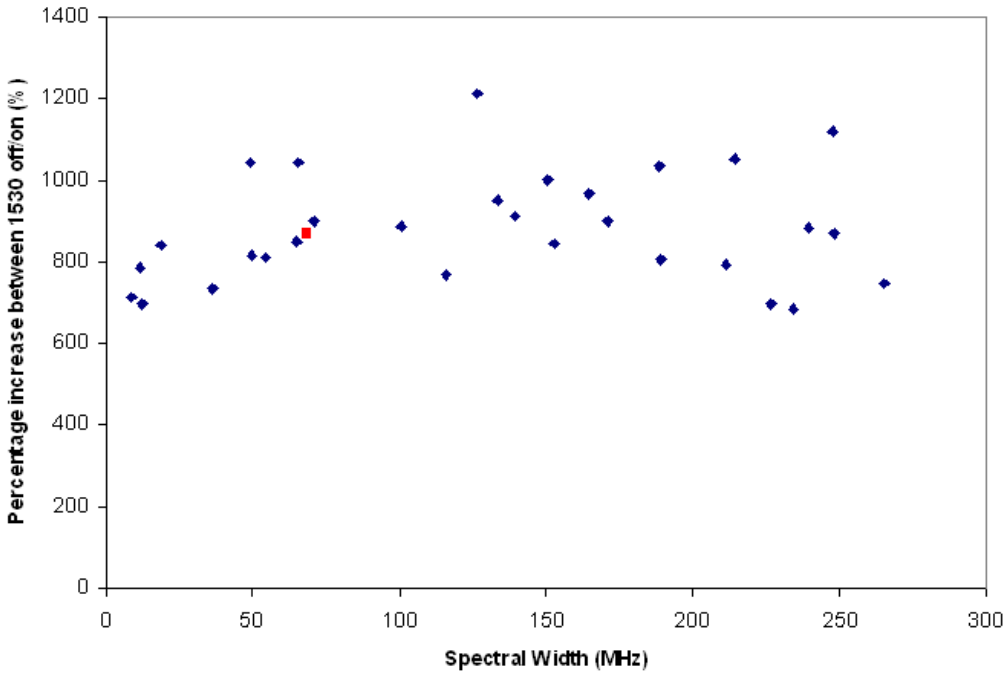

Figure 4.22: The percentage change in the MOT signal between when the 1530 nm laser is on and off as a function of the spectral width of the laser. It can be seen from this that there is little effect. The red data point corresponds to the red data point in Fig. 4.21.

4.6 Conclusions

This chapter has set out to examine the various effects a laser at 1530.5 nm repumping on the $4s4p\,^3P_2 - 4s3d\,^1D_2$ transition of magneto optically trapped calcium. Due to the relative populations of the $^1D_2$ and $^3P_2$ states, when the 1530 nm laser is on resonance with this transition, atoms are pumped into the $^3P_2$ state, instead of the other way around as was desired and expected. This has the effect of increasing the rate of the leak out of the cooling cycle. It was discovered that in order to achieve the desired effect, the 1530 nm laser had to be run in conjunction with the 672 nm laser on the $4s3d\,^1D_2 - 4s5p\,^1P_1$ transition. When both lasers were operating, the expected increase in the number of trapped atoms became apparent. The lifetime of the trapped atoms in the $^3P_2$ state was experimentally calculated to be 928(78) ms. The wavelength of the transition was measured to be 1530.5298(6) nm.

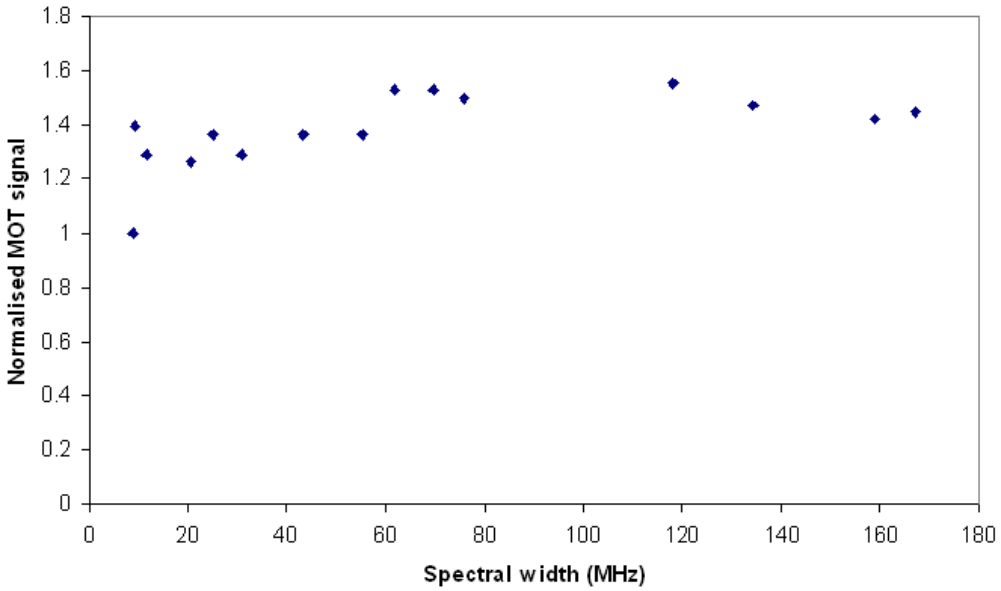

Figure 4.23: The Detected MOT signal from the $^3P_2$ atoms as a function of the 1530 nm laser's linewidth. This shows that above about 10 MHz, the increase in linewidth has no effect.

In addition, the effects of a fiber amplifier for the 1530 nm laser were observed. It was observed that, due to the finite number of trapped atoms in the $^3P_2$ state, above a certain threshold, increasing the intensity of the beam had no extra beneficial effects.

Chapter 5

Interference filter based ECDL design

5.1 Introduction

The final experimental chapter of this thesis will focus primarily on the design, construction and testing of an ECDL based on the idea of using a narrow band interference filter (IFECDL) as the frequency selective element rather than the more typical diffraction grating. This design was considered because the laser was intended for use to probe the intercombination line $4S^2\,{}^1S_0 - 4s4p\,{}^3P_1$ at 657 nm (657.46 nm [75]) and interference filters at or near this wavelength are readily available and ubiquitous in the world of astronomy. This is due to the fact that the hydrogen alpha (Hα) spectral line is at 656.28 nm and astronomers use such filters to observe the sun. Typical examples of such filters have a narrow wavelength transmission profile which can be tuned by tilting the filter through a given angle. While other filter based ECDL designs have been used [91, 92] They tend to be based around narrower, very expensive filters. More recently, broader filters have been used [93]. One benefit of this design is the low cost of the filters used, typically $\sim$ £300. Another is by using the filter as the frequency selective element, the output coupler can be built into the body of the ECDL, resulting in a more stable laser due to eliminating any mechanical movement of a typically used spring loaded mirror mount.

5.2 Design

The IFECDL is designed around the idea of an interference filter being used as the frequency selective element, but otherwise comprises of the standard elements used for a standard ECDL. The laser diode (Hitachi HL6545MG) used is a 660 nm laser diode (the same as is used for the 672 nm ECDL). It is mounted in a machined piece of aluminium behind an adjustable collimation lens. The position of the lens is adjustable by way of an externally accessible dial. The interference filter is then mounted after the collimation lens on a micrometer controlled rotation mount. After this the output coupler (a convenient piece of unnamed optics found in the lab with 10% reflectivity at 657 nm) is mounted on a PZT. The whole laser cavity is approximately 3 cm in length and this can be varied by way of the PZT mounted mirror. The cavity itself is then fixed to a water cooled mount and a Peltier cooler for more subtle temperature control than would be possible by water cooling alone. In this case the Peltier is driven by the temperature control circuit of a MOGBox (MOGLabs DLC-202) laser diode controller with temperature feedback provided by a $10k\Omega$ thermistor housed in the diode mount. It may seem like overkill to use the whole box only for temperature control but it was not suitable to drive the laser current, the current feedforward necessary and the PZT at suitable frequencies. It was, however the most convenient temperature controller available at the time. The design of the IFECDL is shown in Fig. 5.1 and a photograph is shown in Fig. 5.2.

The components are then protected from changes in external temperature and air pressure (such as those caused by periodic activation of the room air conditioning) by encasing everything with a lid machined from a sheet of aluminium.

Instead of driving the laser with the MOGBox, it is driven by a Thorlabs current control circuit (Thorlabs LD1255R) subtly adjusted to allow coarse and fine current adjustment and set up so as to allow an external amplitude modulation of the laser current. The typical power available from this laser is up to 16 mW. The laser is kept at a constant 12.6°C throughout this work.

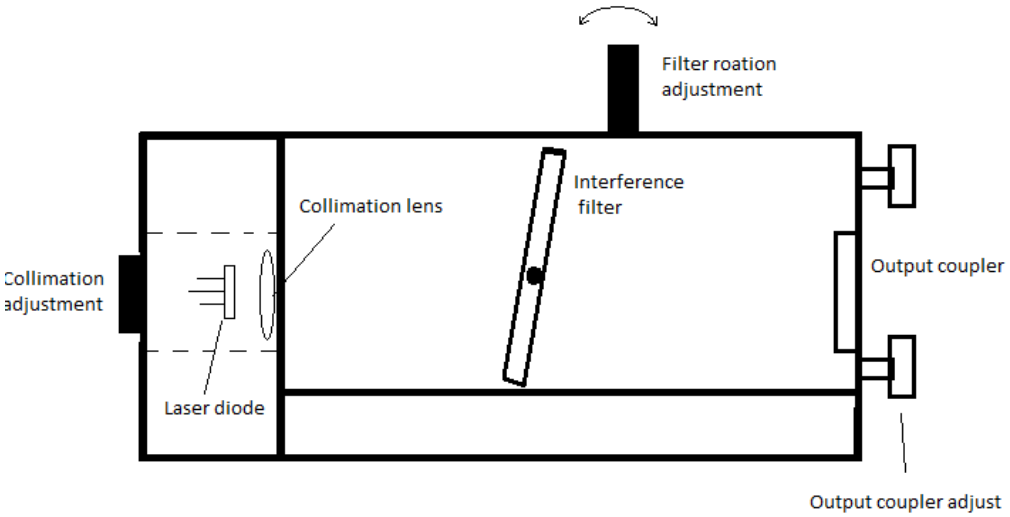

Figure 5.1: The design of the IFECDL as viewed from the top down.

5.3 Filters

For this design, there were two different interference filters to test: the hydrogen-alpha (H-α - Astrodon Tru-Balance H-a CCD Filter) centred round 656.3 nm and the nitrogen-two (NII - Astrodon Tru-Balance NII CCD Filter) filter centered around 658.4 nm. This section will concentrate on a brief, rough analysis of the transmission/angle profiles of these two filters, done in order to determine which was the filter best suited to our needs.

The filter acts precisely as an etalon (this will be important later) - as the angle between the beam and the normal to the filter changes, the filter tunes the output wavelength towards the blue end of the spectrum according to

$$\lambda_c = \lambda_0 \sqrt{1 - \frac{sin^2(\theta)}{n^2}}, \tag{5.1}$$

where $\lambda_{c,0}$ are the centre wavelengths of the output and normal incidence input beams, respectively, θ is the angle of incidence and n is the refractive index of the filter in question. It can be seen from this that altering the angle of the filter

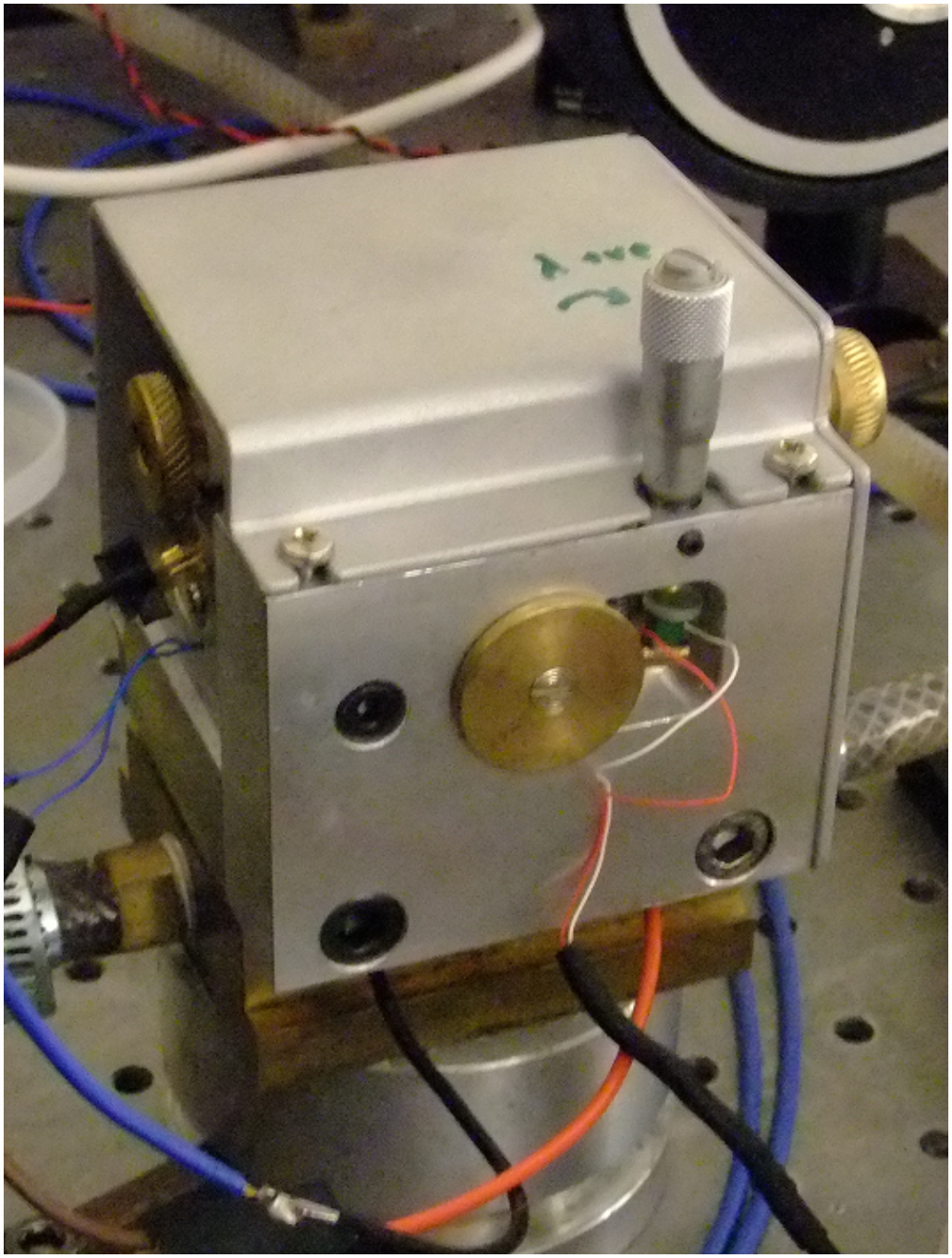

Figure 5.2: A photograph of the IFECDL.

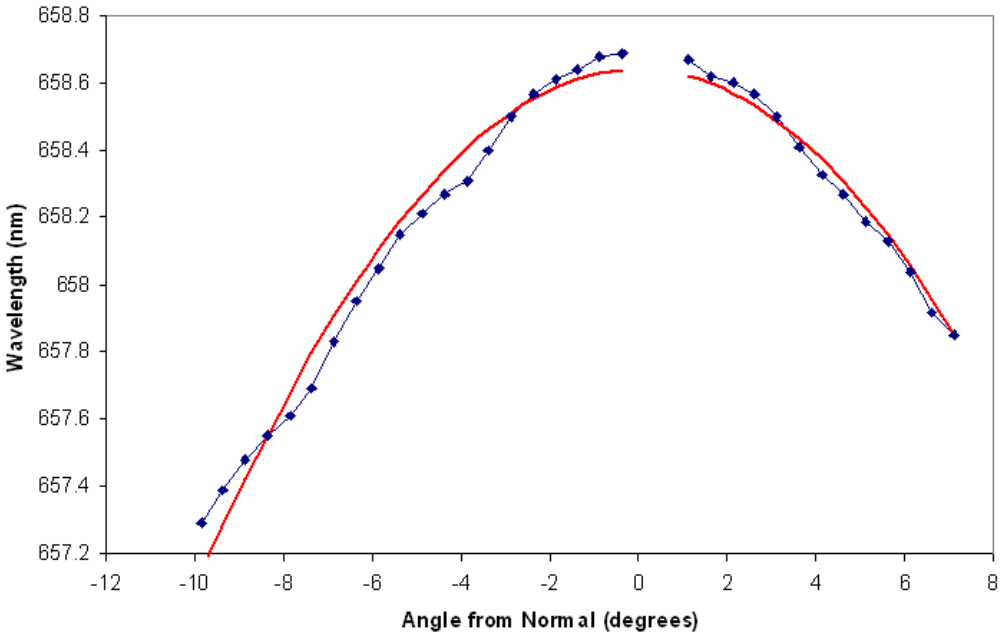

Figure 5.3: The peak transmitted wavelength as a function of filter angle of the NII filter. The blue points are experimental data, the red curve predicted by theory.

causes a lower wavelength to be transmitted. Given the NII filter has a centre wavelength to the red of the line and the H-α filter to the blue, the NII filter was the obvious choice to continue with.

To test this a simple procedure was carried out. The filter in question was placed in the centre of the cavity and rotated through several degrees. As this was done, the rough emission wavelength was observed of an optical spectrum analyser (Ocean Optics HR2000). The peak emission wavelength was then plotted against the angle of the filter with respect to the direction of beam propagation. The NII filter's tuning study is shown in Fig . 5.3.

As can be seen from Fig. 5.3, the NII filter tunes smoothly over the angles used. The fit performed in Fig. 5.3 returns a filter refractive index of ~ 2.5 The gap at $\sim 0^{\circ}$ occurs because, with the filter normal to the beam, the beam is reflected back on face of the diode, inundating it with a great deal of excess optical feedback. The 'wiggle' seen in the experimental data could, in fact, be an additional cavity of length $\sim 300\mu m$, likely to be located within the filter).

5.4 Tunability study

With the filter chosen and in place and with the laser emitting at a wavelength that was within a nanometer of the line in question, the next step was to see how tuneable the laser was. That is, to see how the laser frequency could be tuned without hopping modes. The other ECDL used in this work, the 672 nm laser discussed in detail in Chapter 3 had a mode hope free tuning range of between three and four GHz so it was decided that this was the minimum that should be aimed for.

5.4.1 Test setup

The setup for this portion of the experiment is as follows. The laser was passed through an optical isolator (Linos FI-630-5 SV) and coupled into a Fabry Perot cavity with 1GHz FSR and specified finesse of ~ 1000 (Toptica FPI-100-0750-1). Initially the laser was not scanned while the cavity was scanned to simplify the process of the coupling alignment. Once the alignment had been optimised, any adjustments to the laser current necessary to ensure single mode operation of the laser were carried out. With the laser now running in single mode operation, the cavity scan was stopped and the laser itself was scanned by way of a PZT upon which the output coupling mirror was mounted. By doing this, the mode-hop free tuning range of the laser was observed to be not more than $\sim$ 2GHz. While this could be seen as sufficient, it was not deemed good enough. The main reason for this, besides professional pride, was that it could not necessarily be guaranteed that the laser could be tuned to within 2 GHz of the line in question routinely. Also, as there was only a 2 GHz tuning range, the laser was very sensitive to drifting.

5.4.2 Scan with Feed forward circuit

Once it was determined that the laser would not provide a reliably large mode-hop free tuning range, a feed forward (FF) circuit was designed and built to remedy this. An ECDL lases when the diode's own laser modes line up with the modes of the frequency selective element. A laser will mode hop when the two drift relative

to each other, causing a different laser mode to line up with a different mode of the frequency selective element. FF attempts to stop this happening by tuning one in time with the other, so keep the two desired peaks lined up for as long as possible (see Fig. **??** later in this chapter). Additionally, feedback to the laser current (where the laser is modulated back and forth rapidly to attempt to detect potential mode-hops) was applied by way of the following setup. A portion of the light directed towards the FP cavity is split off by passing it through a glass plate at an angle to the beam. The reflected light is then detected by a photodiode and fed to a lock in amplifier (SRS SR530). At the same time, a frequency modulation is fed to both the lock-in amplifier (as the frequency reference) and to the laser diode current (via the home made FF circuit) by a signal generator (Marconi Instruments 2022C). The resulting signal from the lock-in is then fed into the FF circuit. The signal driving the PZT is also fed into this circuit. The output is then applied to the external current control port on the laser diode current driver. This can be visualised as the feedforward controlling the diode current to follow the tuning of the cavity length linearly, which may not be enough. The feedback then applies a little bit extra tuning to the current to overcome the difference. This is shown diagrammatically in Fig. 5.4.

The inclusion of this FF/FB circuit in the setup allowed a routinely attainable mode-hop-free tuning range of 8-10 GHz, with up to 15 GHz seen on occasion. A sample of of the tuning range data taken is shown in Fig. 5.5. In this situation, the 1GHz FP cavity is stationary and the laser cavity is scanned.

It can be seen from Fig. 5.5 that the IFECDL has a mode-hop free tuning range of, in this example, 10GHz. The discrepancy between the mode spacings is simply due to the nonlinearity of the PZT scan - it was not necessary to perform the same polynomial adjustment of the frequency axis as was performed in Chapter 3 in this case.

5.4.3 Effects of varying modulation power

Following this in an attempt to further improve the mode-hop free tuning range was made. The frequency and power supplied by the signal generator were varied and the effects on the tuning range were observed. First of all, the power was

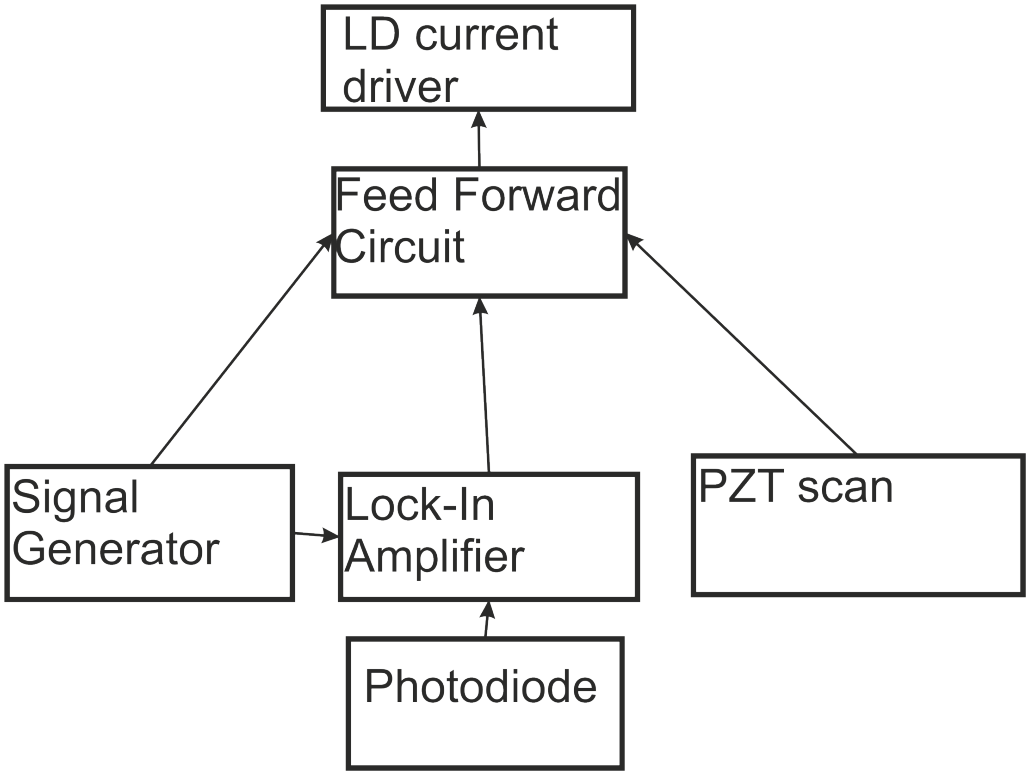

Figure 5.4: A box diagram of the feed forward and feed back setup described in the text.

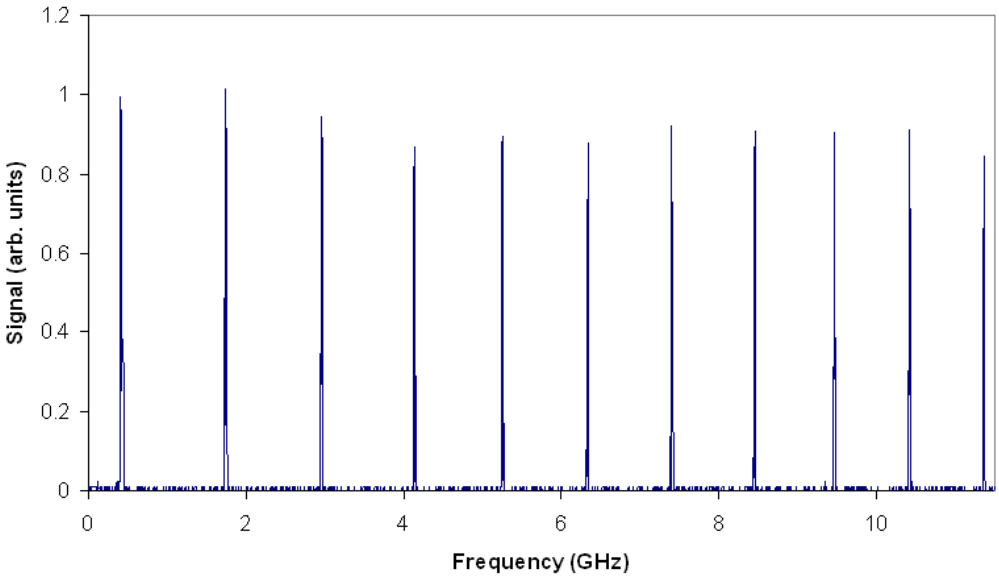

Figure 5.5: The tunability of the IFECDL with the feed forward circuit.

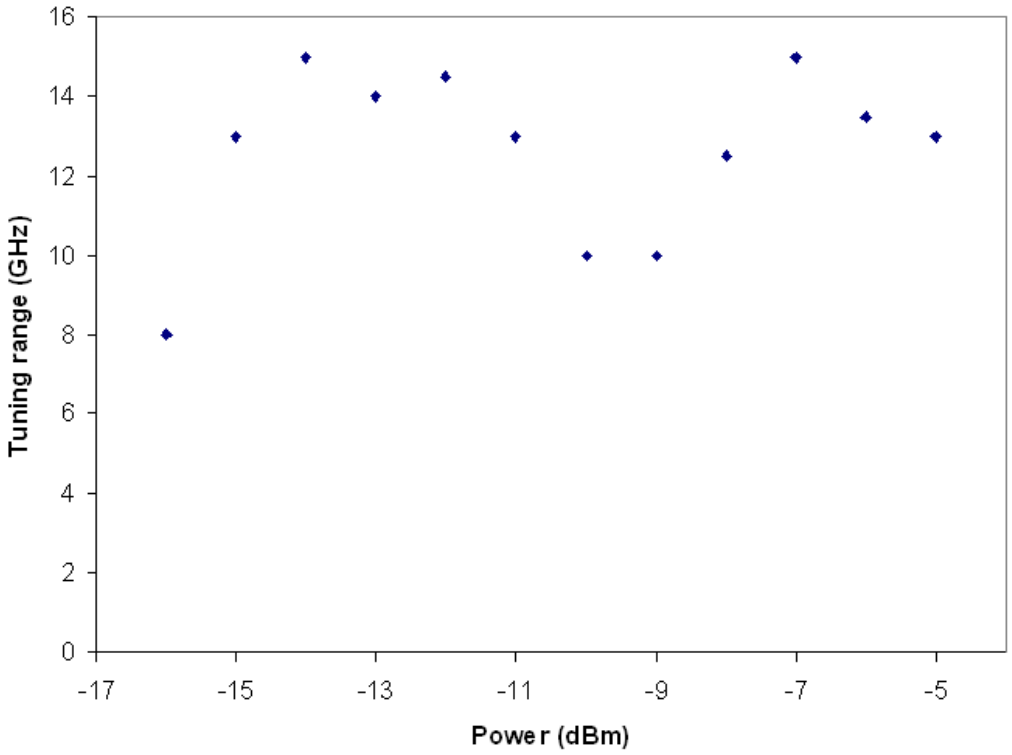

Figure 5.6: The effect of modulation power of the attainable tuning range of the laser. The frequency was kept at a constant 20 kHz.

adjusted from -20 dBm to -3 dBm with the modulation frequency kept constant at 20 kHz. The FF circuit could not be successfully locked between -20 dBm and -17 dBm, nor could it be locked at -4 dBm or -3 dBm. In Fig. 5.6, the mode-hop free tuning range as a function of modulation power power is shown. The discrepancy between the tuning range quoted above and those noted in this and the next sections is due to the previously mentioned occasionally seen 15 GHz mode-hop free tuning range of the laser.

It can be seen from Fig. 5.6 that the tuning range was not greatly affected by changes in the modulation power. There needs to be sufficient power to attain a good lock while too much power stops locking, but with the reasonably large range in between, there is no definitive effect.

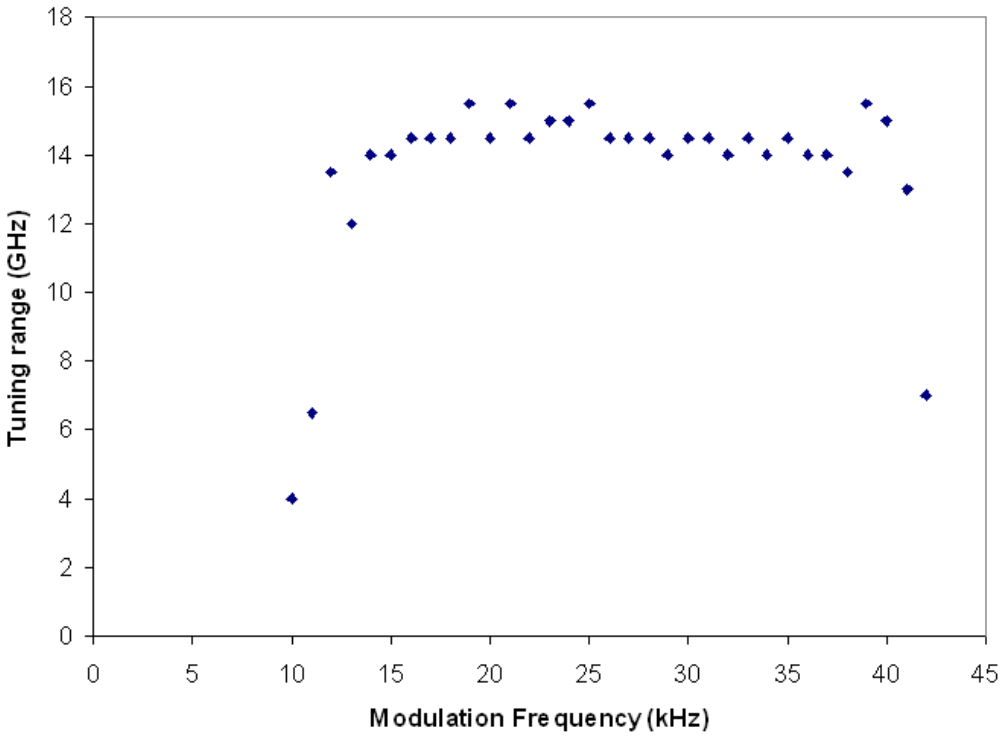

Figure 5.7: The effect of modulation frequency of the attainable tuning range of the laser. The modulation power was kept constant at -14 dBm.

5.4.4 Effects of varying modulation frequency

With differing modulation powers checked, the last parameter left to vary was the modulation frequency. To this end, the same experiment as above was repeated, but with the frequency being varied between 10 KHz and 42 KHz. Below 10 kHz and above 42 kHz the laser would not tune at all. The power was kept at a constant -14 dBm. This is shown in Fig. 5.7. It was also attempted to try and increase the modulation frequency to the MHz level by way of a bias tee, much like in Chapter 3, but this was found to have no beneficial effect.

As can be seen from Fig. 5.7, varying the modulation frequency between about 15 KHz and 40 KHz has little to no effect on the mode-hop free tuning range of the IFECDL. Either side of this range, the tuning range drops sharply.

5.5 Detection of the $4S^2\,{}^1S_0 - 4s4p\,{}^3P_1$ intercombination line at 657 nm

With the tunability of the new laser observed as being a factor of 3 better than originally hoped for, it was time to try and see the if we could find the $4s^2\,{}^1S_0 - 4s4p\,{}^3P_1$ intercombination line. The first step was to determine, given the very narrow linewidth of less than 400 Hz [94], the frequency of the transition rather than the wavelength and to tune the laser to as close to this frequency as possible. The frequency of the transition is 455986.240494158(26) GHz [95]. Our wavelength meter (Coherent Wavemaster) can display laser frequency in GHz to one decimal place, allowing us to be confident of being within 100 MHz of the intercombination line at best.

5.5.1 Setup

For this experiment, the 657 nm laser was directed towards the MOT, using the 1530 nm laser as a guide beam. This laser was used rather than the more obvious choice of the 672 nm beam because due to the nature of the setup, it was a simpler task to block the 672 nm beam and pass the 657 nm beam along the path it used to take than it would have been to do the same for the 1530 nm laser beam. This is due to the fact the key part of the setup used to overlap the 672 nm and 1530 nm beams is a dichroic mirror (Newport 10HMR-0) which reflects in the infrared and is transparent at visible wavelengths.

It was hoped that simply by passing the 657 nm laser through the MOT cloud while the laser frequency was slowly scanned, a change in fluorescence from the MOT would be visible as a decrease in signal as atoms are pumped out of the ground state as the laser came on to resonance with the ${}^1S_0 - {}^3P_1$ transition. Unfortunately, this was not the case.

Once this had been established, it was decided to try lock-in detection as there must be *some* effect on the MOT, but perhaps not be visible to either the naked eye or the MOT photodiode. Lock in detection excels at picking out very small changes in signal. To this end, a mechanical chopper driven at 500 Hz by an SRS SR540 Chopper Driver was placed in the path of the 657 nm

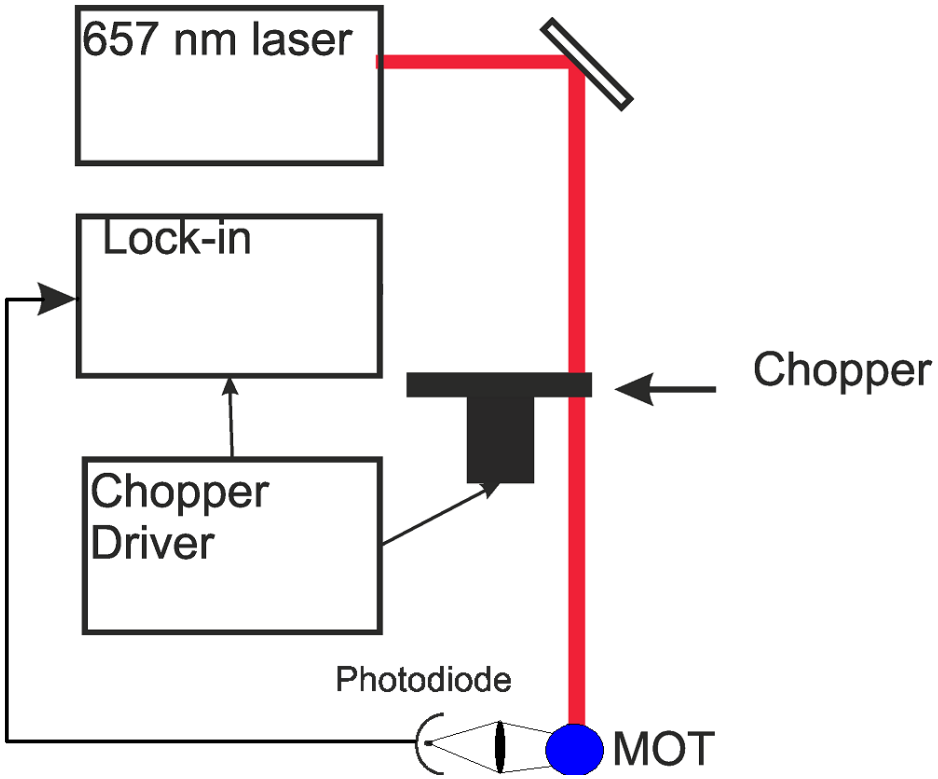

Figure 5.8: The setup for the lock-in detection of the 657 nm laser experiment.

beam. The driver also fed a 500 Hz signal to a lock-in amplifier (SRS SR510) as the reference signal. The signal to be demodulated simply came from the MOT photodiode. The resulting lock-in derived signal was fed to a standard lab oscilloscope (Tektronix TDS 2014B). This setup is shown in Fig. 5.8 and a sample of one such signal is shown in Fig. 5.9.

The signal seen in Fig. 5.9 represents a change in MOT signal of only ~ 1 mV, based on the 2 mV sensitivity setting of the lock-in amplifier and the size of the peak. This explains why the feature was not visible to the naked eye: such a small change would be lost in the MOT signal noise.

5.5.2 657 intensity

With the line located, it was time for some preliminary experiments. First of all, to determine how sensitive our detection system was, we repeated the above procedure for decreasing 657 nm laser intensities. Lowering the beam power

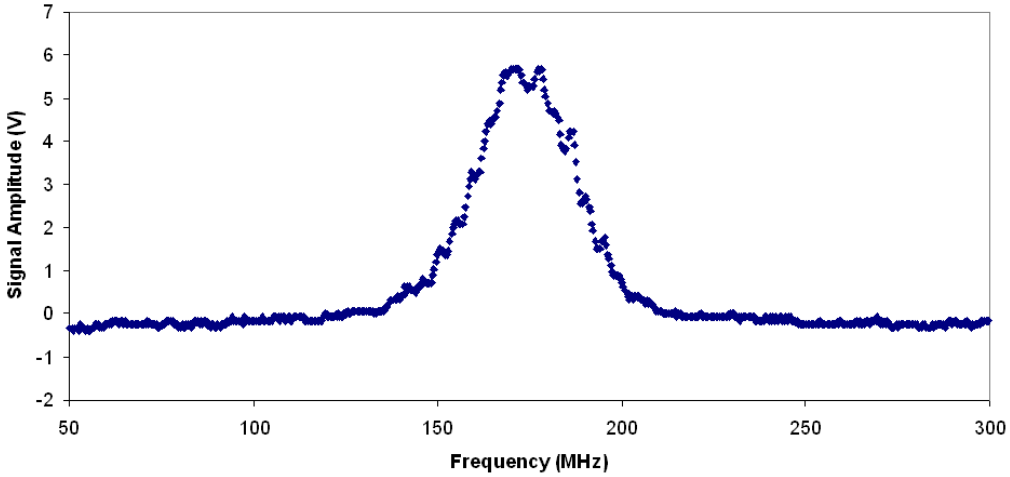

Figure 5.9: An example of the signal derived from the lock-in amplifier using this setup. The frequency axis is derived from Fig. 5.5

from 16.4 mW to 0.07 mW (and thus the intensity from ∼183 mW/cm^2 to ∼0.8 mW/cm^2), we were still able to observe the peaks seen above which represent the ${}^1S_0 - {}^3P_1$ transition. From this, cursory measurements of the peak widths were taken, as shown in Fig. 5.10.

These linewidths do not match up to our first expectations, given the purely power broadened linewidth of the 370 Hz line should be only ∼12 kHz with our laser power of 16.4 mW, according to (4.4)

This is obviously much narrower than the experimental data. However, the majority of what we see experimentally in this case could be down to the linewidth of the laser itself, which is ∼20 MHz, as seen in Fig. 5.11, which is merely a zoomed in view of Fig. 5.5.

This, however, was simply a preliminary measurement made to see if we would see anything before moving on to attempt to improve the system. In addition to these measurements, we also observed the linewidth of the 657 nm feature with lowered intensities in the MOT beams and with varying red intensities with the MOT coils off. These showed much the same features as seen in Fig. 5.9.

It was at this moment, however, that something odd struck us. As stated previously, without the FF circuit and feedback system, we get only around 2 GHz mode-hop-free tuning range. The issue is that, with a cavity of length ∼ 30

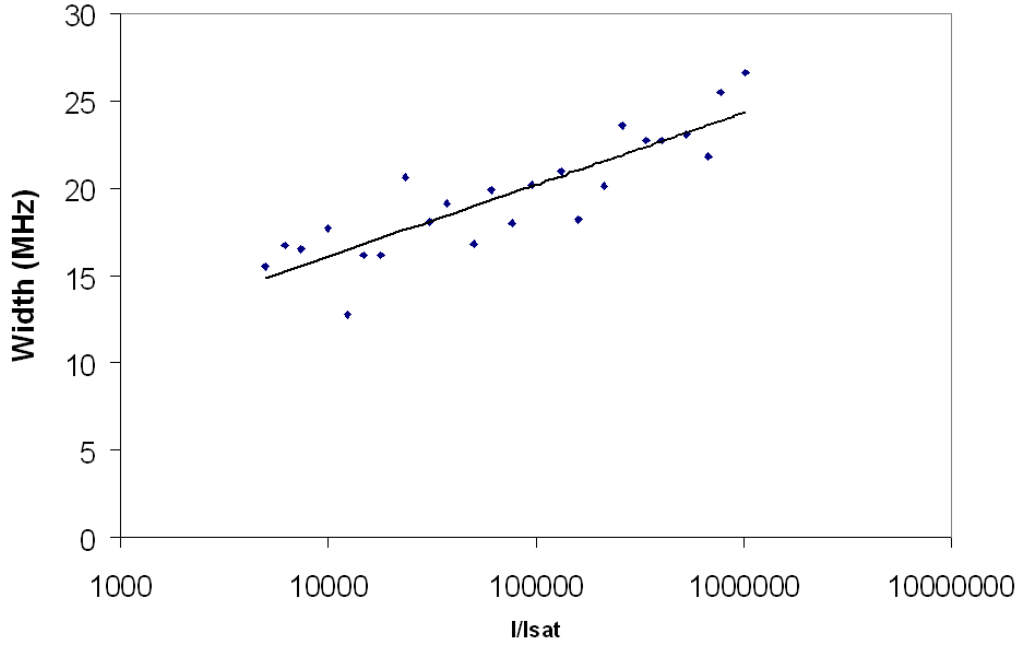

Figure 5.10: How the width of the 657 nm feature varies as the saturation parameter is increased. Widths are obtained from Lorentzian fits to the peaks derived from the lock-in amplifier. The X axis is in log scale and the black line is a logarithmic fit to guide the eye.

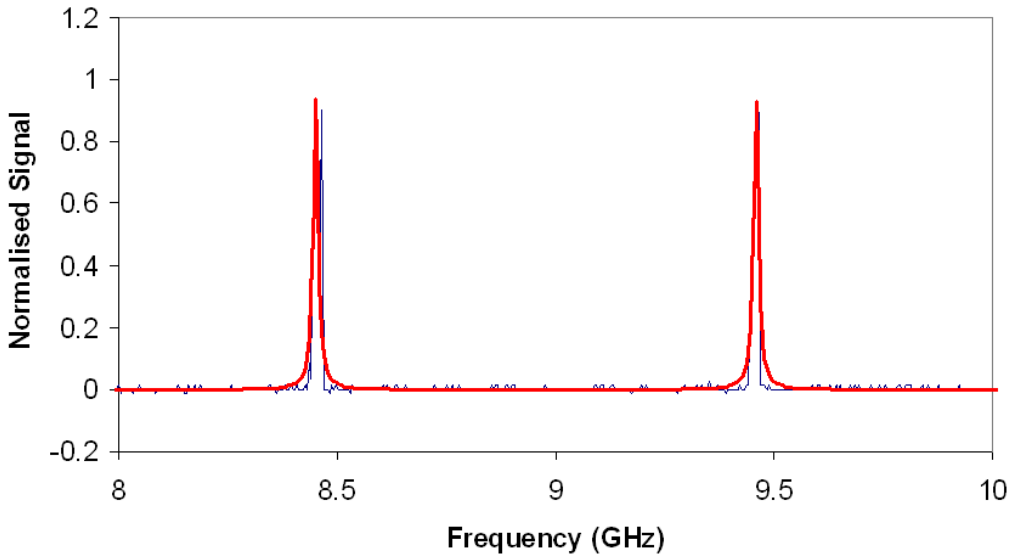

Figure 5.11: The linewidth of the laser. The blue is the experimental data and the red is the Lorentzian fit.

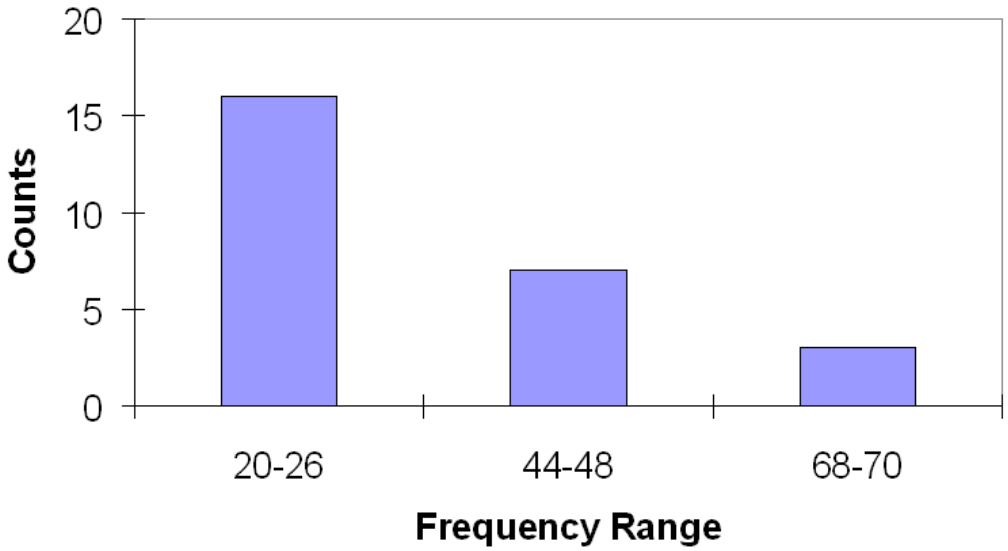

Figure 5.12: The mode hops of the 657 nm laser.

mm with FSR $\sim$ 5 GHz, we should expect to get a mode-hop-free tuning range of this FSR very easily. This was just not possible with this laser at this point.

The cause of the problem was not immediately obvious. It was only after observing the actual mode hops that the laser made on a wavelength meter (Coherent Wavemaster) that the answer started to suggest itself. To do this, either the laser current or the filter angle were adjusted through several mode hops and back again, noting the frequency of each instance of single mode operation as read off the wavemeter. If we were just dealing with the external cavity, we would expect mode hops of the external cavity FSR. This is not what we saw. Shown in Table. 5.1 are the frequencies read off the wavemeter as the laser current was tuned down and then back up again.

When looking at this data set, certain patterns begin to emerge and certain mode hops begin to seem preferential. When put into a histogram, a clear picture emerges, as seen in Fig. 5.12

With this is mind, a picture begins to form of an ECDL with a third, weak cavity with high FSR fighting the others for dominance. The diode itself is expected to form a cavity between its front and back face of around 45 GHz, as seen and the output coupler and the diode for the cavity of 5 GHz FSR, which

Frequency (GHz)	Frequency Change (GHz)
455586.3	
455609.1	+22.8
455584.9	-24.2
455560.4	-24.5
455514.8	-45.6
455536.3	+21.5
455491.0	-45.3
455512.8	+21.8
455443.6	-69.2
455512.4	+68.8
455442.6	-69.8
455420.5	-22.1
455467.0	+46.5
455512.9	+45.9
455491.0	-21.9
455513.9	+22.9
455491.0	-22.9
455537.0	+46
455515.1	-21.9
455561.0	+45.9
455584.6	+23.6
455561.0	-23.6
455538.1	-22.9
455585.2	+47.1
455562.0	-23.2
455608.6	+46.6
455632.0	-23.4

Table 5.1: Mode hops observed for the 657 nm laser. The division on the table represents when the laser current tuning was reversed.

doesn't appear in the data, as expected given the trouble tuning a whole FSR of the cavity. The third cavity is caused by the filter itself - it is acting exactly like an intra-cavity etalon with FSR $\sim$ 70 GHz. As can be seen from Fig. 5.12 and Table 5.1, the dominant mode hop is around 23 GHz, with less at $\sim$45 GHz and even fewer at $\sim$70 GHz. The dearth of 70 GHz mode hops suggests that the etalon cavity is a weak one, which is expected as the reflectivity at the correct wavelength is only about 4%. With the laser diode cavity, a stronger effect is seen, explaining the higher number of 45 GHz mode hops. The overwhelming number of 23 GHz mode hops appear to be the result of the other two cavities competing against one another: 70 GHz - 45 GHz is 25 GHz, which is close enough to the values seen to be highly suggestive.

To test this supposition, the H-α filter was placed down the beam in the beam path and tilted through a wide range of angles. If it acts like at etalon, dark fringes should appear in the reflection signifying maximum transmission through the filter/etalon. This was seen and the angle between successive dark fringes allows us to determine the filter/etalon FSR. Assuming the two filters are broadly identical, this gives us the NII filter's FSR, which matches the expectation based upon the mode hops observed on the wavemeter.

If we start thinking of things with this is mind, we get a clearer picture of why the laser behaves as it does. Consider Fig. 5.13 as representative of this system. This looks similar to a figure produced in [93], but differs due to our filter not being AR coated. The blue curve represents the filter transmission profile with this inherent etalon effect added on to it. The grey slope is the diode gain curve and the red trace represents the diode cavity fringes. The product is the green trace, which includes all the IFECDL cavity modes.

If we then look at this in more detail it can be seen that when the filter etalon fringes line up with the diode cavity fringes, one single IFECDL cavity mode is selected over all the others. Looking at Fig. 5.14, as the cavity and laser FF current is tuned, the preferred peak begins at 659.8 nm (A), begins to move to the left gradually (B), until the filter and diode cavities no longer line up and mode hops to a different, more suitable combination of the two (C). It then keeps going until there is not a clear choice between two separate cavity modes (which leads to multimode operation) (D) before it returns to the starting point (D).

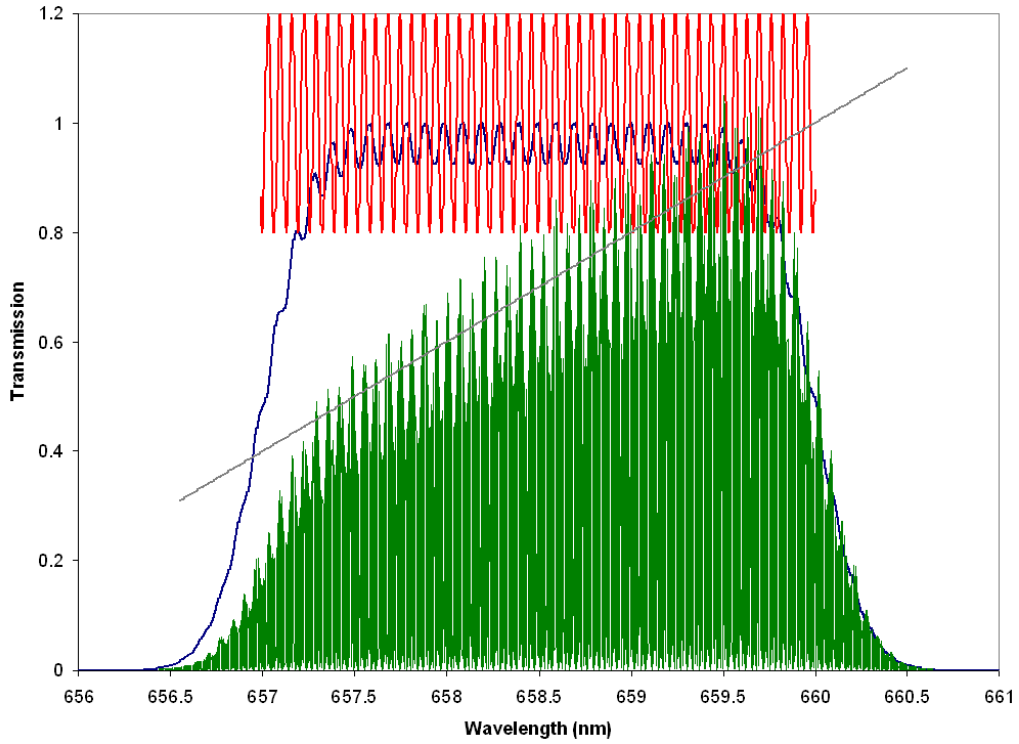

Figure 5.13: The different cavities fighting each other produces a curve like this. Blue: Filter transmission + etalon fringes. Grey: diode gain curve. Red: Diode cavity fringes. Green: the product, including the IFECDL cavity fringes.

This is borne out experimentally as the laser was frequently seen to return to within 1-3 GHz of previous frequencies.

Having seen this, an attempt was then made to try and use the existing FF circuit while also feeding forward to the filter angle. This should have the advantage of giving a longer mode-hop-free tuning range than before whilst also doing away with the need to modulate the current with the signal generator. While this did allow for a 10 GHz mode-hop-free tuning range before, it is expected that this could cause problems in the future as, while 20 kHz noise on a 20 MHz laser is fairly insignificant, if the laser is to be made comparable in linewidth to the 370 Hz transition linewidth, then 20 kHz will become *very* significant.

To allow us to try this additional FF, a PZT (Thorlabs AE0203D04F) was installed between the micrometer and the arm controlling the angle of the filter. A voltage divider circuit was then built to pick off part of the voltage driving

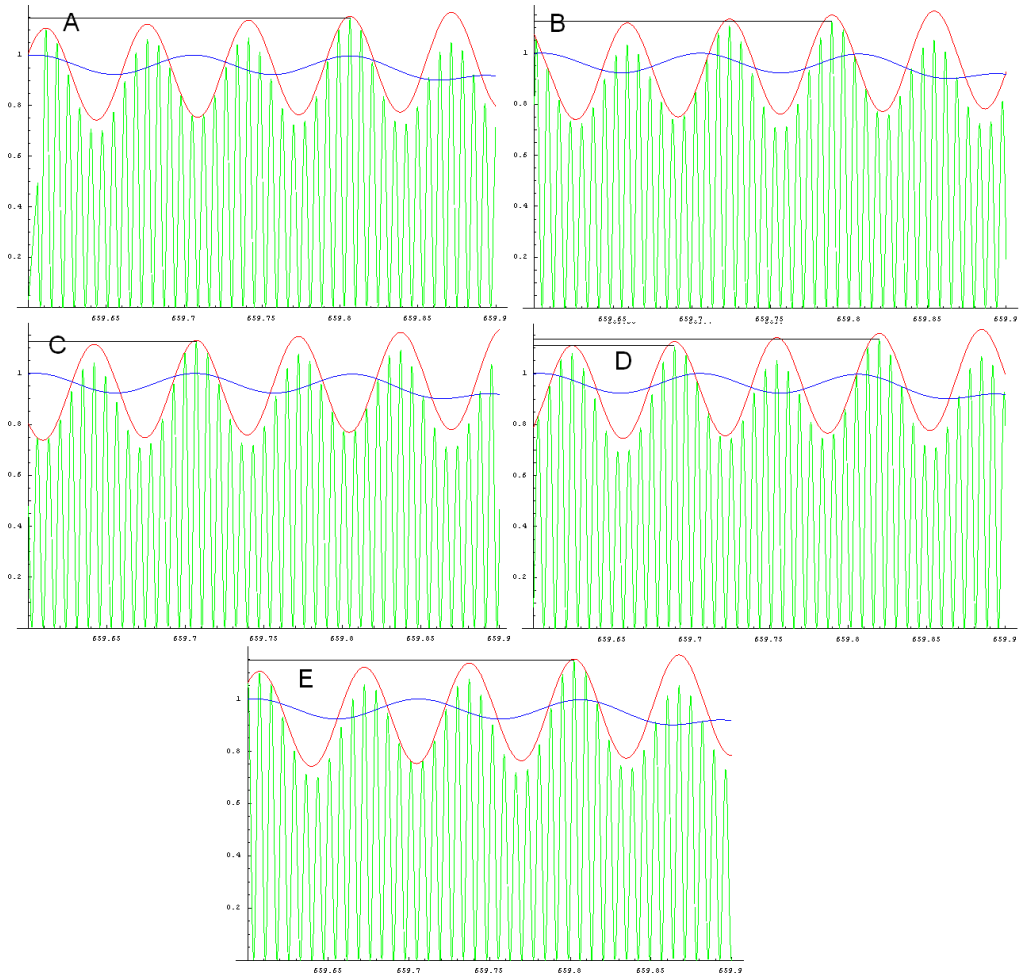

Figure 5.14: How the cavities cause different cavity modes to dominate and how this changes as the laser diode current is tuned. The horizontal black lines on each figure are there to indiciate which cavity mode is likely to be dominant.

the output coupler PZT and direct it towards the filter arm PZT. Unfortunately, this did not improve things in an appreciable way - the maximum mode-hop-free tuning range with this setup was seen to still be only $\sim$ 2 GHz.

However, this was sufficient to once again tune to and observe the 657 nm line using the same method as before. The difference this time was that the laser was locked to an external reference cavity.

5.6 Locking the IFECDL

With preliminary tests and experiments carried out with the IFECDL, it was time to attempt a more concrete approach. First of all, the IFECDL would be locked to an external reference cavity to reduce its linewidth from the free running $\sim$20 MHz to something more appropriate.

5.6.1 Setup

For locking the IFECDL to a cavity, the standard Pound-Drever-Hall (PDH) locking technique [96, 97] was used, which is summarised here.

A portion of the laser light is directed through an electro-optic modulator (EOM) towards a FP cavity (FSR of 2 GHz, finesse of $\sim$ 70). The light that is reflected from the cavity is picked off and directed towards a photodiode. The EOM is driven by an oscillator operating at $\sim$ 13 MHz. The signal is split in a directional coupler (Mini-Circuits ZFDC-20-3) so that a small fraction of the signal gets fed into a double balance mixer (Mini-Circuits ZP-3). The signal from the photodiode is then fed into the other channel of the double balance mixer. The output of this is then passed through a low-pass filter (to remove high frequency modulations) which produces a standard dispersive error signal which is fed into an integrator circuit to lock the laser frequency to the zero crossing. This setup is seen in Fig. 5.15.

A typical lock signal derived from this setup is shown in Fig. 5.16. It can be seen from a comparison between the separation of the two lock signals seen in Fig. 5.16 (being separated by the cavity FSR of 2 GHz) and the depth of the locked signal seen in Fig. 5.17 that the linewidth is now $\sim$ 1 MHz. If the two

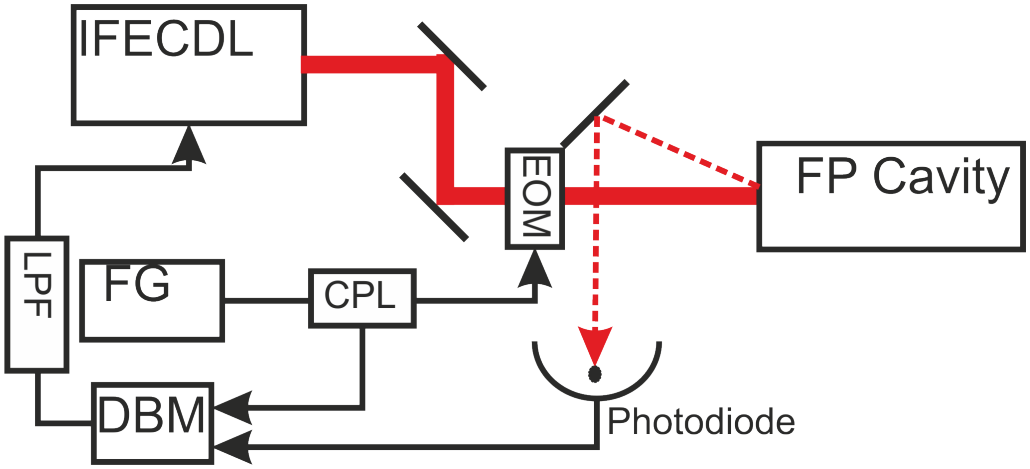

Figure 5.15: The PDH setup. FG = function generator, DBM = double balance mixer, CPL = directional coupler, LPF = low pass filter.

peaks are 2GHz apart, then it is possible to determine how far apart in frequency either side of the slope in the lock signal are. This then allows the voltage between the highest and lowest part of the locking signal to be interpreted as a frequency, giving us $\sim$ 0.3 mV/MHz. This is then used to calculate how 'deep' the locked signal is: $\sim$ 1 MHz. The spikes seen in the data in Fig. 5.17 are simply 50Hz noise, likely from the room lights. As a quick test, the frequency modulation used earlier is switched on at this point to see if the expected detrimental effect mentioned previously is apparent. This is shown in Fig. 5.18.

This shows that at the level of a 1MHz laser linewidth, the frequency modulation has a clear effect on the lock strength, effectively doubling the width of the lock point. While this could be tolerated with a 1 MHz laser, such an increase would be self defeating if applied to a much narrower laser.

With the laser locked to this reduced linewidth, it was expected that the linewidth of the observed feature would be much narrower as a result. One such measurement is shown in Fig. 5.19.

While the laser was known to be $\sim$ 1 MHz wide, the feature seen is still in the tens of MHz region. The feature linewidth for increasing beam intensities is shown in Fig. 5.20.

It could even be argued from Fig. 5.20 that the 657 nm laser intensity, at these levels, does not have much of an effect at all, with the first two points on

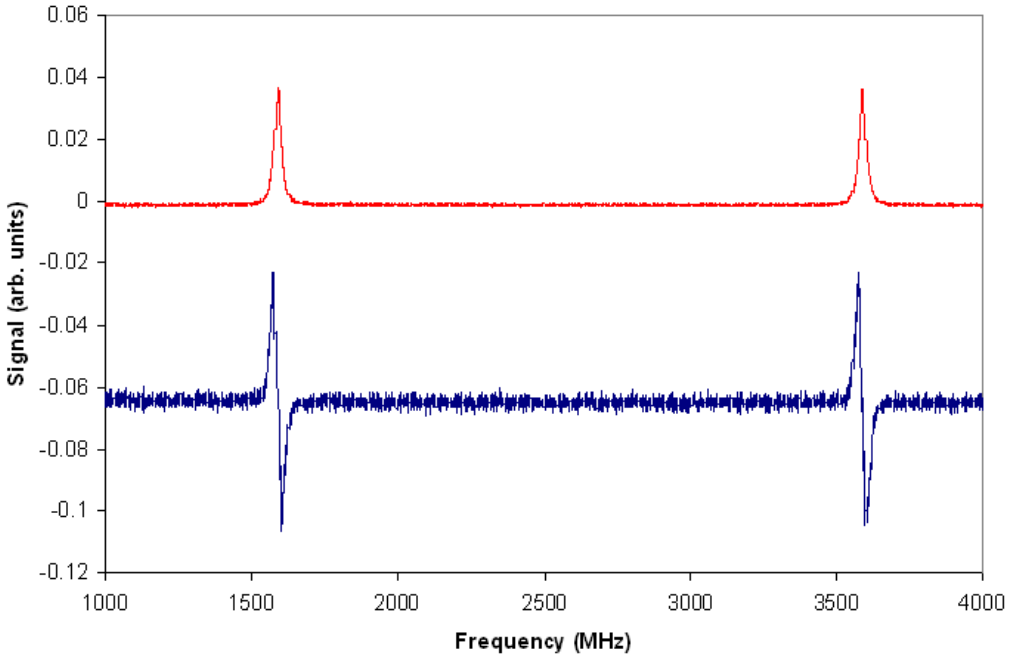

Figure 5.16: The locking signal derived from the PDH locking. The red is the cavity transmission, the blue is the resulting lock signal. Worthy of note is that in PDH locking, one would normally expect to see smaller error signals either side of the main peak, at the EOM modulation frequency. However, as the linewidth of the peaks seen is around 30 MHz, these 13 MHz features will be hidden within this linewidth.

the graph being outliers.

5.6.2 V-system

The values obtained for the linewidth of the 657 nm feature are obviously orders of magnitude above the natural linewidth of the transition, which is $\sim$ 370 Hz. This is due to the fact that we are not dealing with a simple, ideal two level atomic system. When the red transition is observed whilst the blue laser is on, there are three levels involved. If we treat the whole process here as a three level system, with the levels being the $^1S_0$ ground state and the $^1P_1$ excited state of the main cooling transition and the third being the $^3P_1$ state, we set up what is known as a V-system, shown diagrammatically in Fig. 5.21.

Consider the fact that, spin aside, the $4s^2\ 4s4p\ ^1P_1$ transition and the $4s^2\ 4s4p\ ^3P_1$

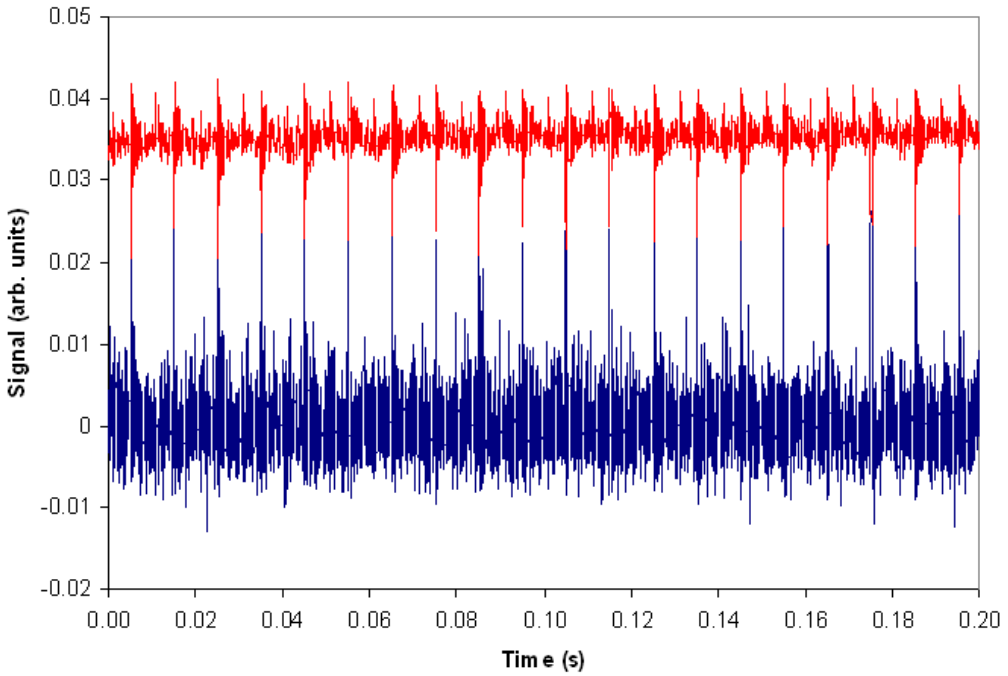

Figure 5.17: The locked signal from the PDH setup. The red is the cavity transmission, the blue is the resulting lock signal.

transition are identical. It is this similarity that allows the $4s^2\ 4s4p\ ^3P_1$ intercombination line transition to exist at all. This also brings with it some problems for the type of measurement we have tried to do. While the intercombination line exists by 'borrowing' a bit of linewidth from the main cooling transition, this same arrangement works against us when trying to measure the linewidth of the intercombination line whilst the main cooling laser is active. This is governed by the following equations [88].

$$\varrho_{33} = -\gamma_3\rho_{33} + 2i\alpha_2 cos(\Omega_2 t + k_2 z)(\rho_{32} - \rho_{23}), \tag{5.2}$$

$$\varrho_{22} = -\gamma_2\rho_{22} + 2i\alpha_2 cos(\Omega_2 t + k_2 z)(\rho_{32} - \rho_{23}) + 2i\alpha_1 cos(\Omega_1 t + k_1 z)(\rho_{21} - \rho_{12}), \tag{5.3}$$

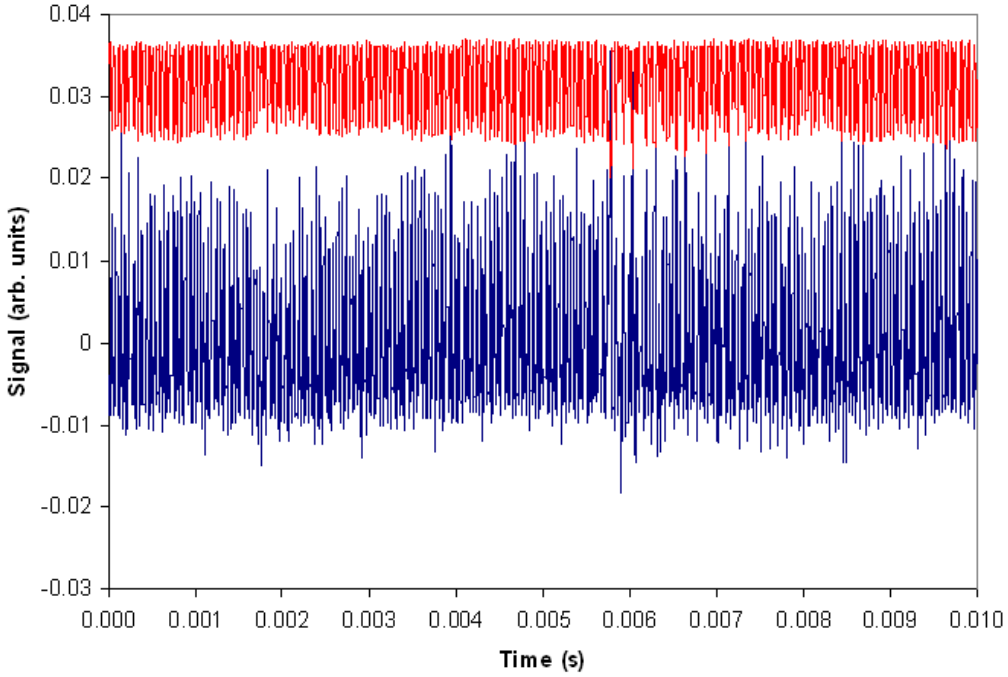

Figure 5.18: The locked signal once the frequency modulation (20 kHz, -14 dBm) is applied. The red is the cavity transmission, the blue is the resulting lock signal.

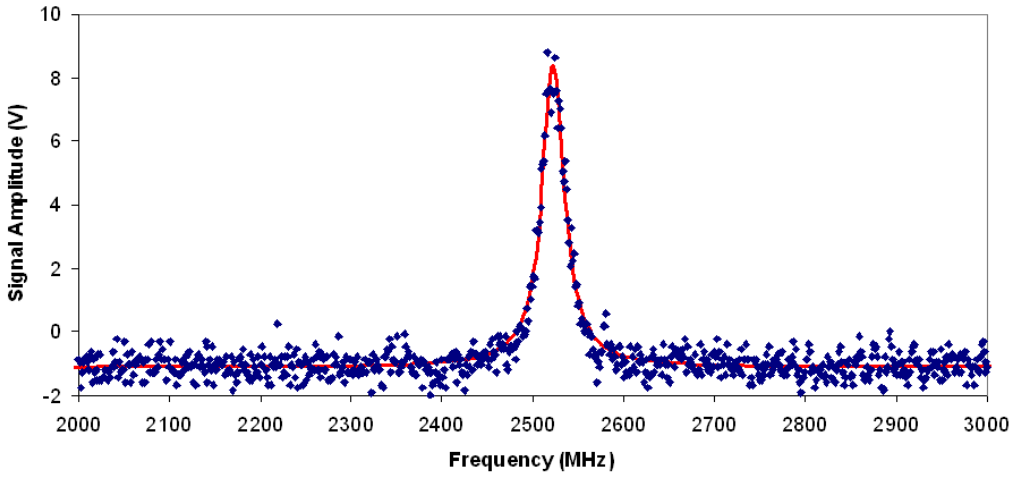

Figure 5.19: The 657 nm feature observed with a laser with $\sim$ 1 MHz linewidth.

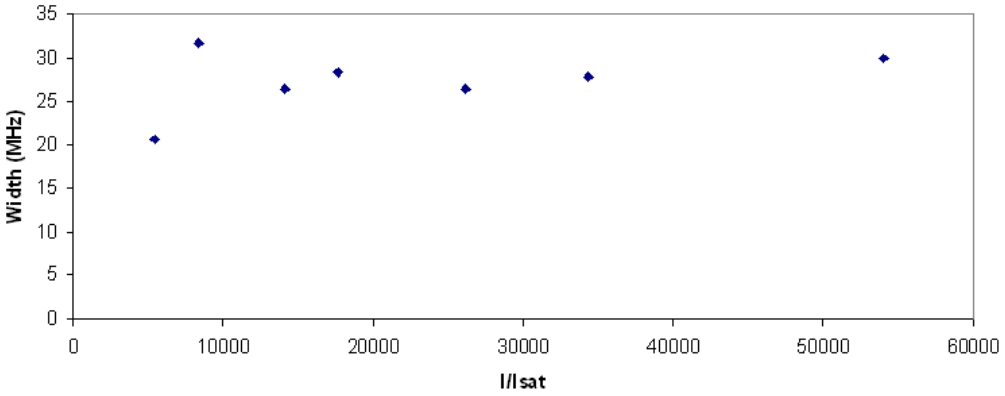

Figure 5.20: the 657 nm feature observed with a laser with ~ 1 MHz linewidth.

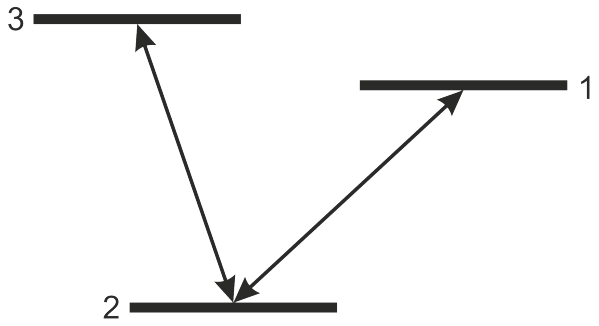

Figure 5.21: A simple representation of a V-system.

$$\varrho_{11} = R - \gamma_1\rho_{11} + 2i\alpha_1 cos(\Omega_1 t + k_1 z)(\rho_{21} - \rho_{12}) \tag{5.4}$$

and

$$\varrho_{32} = -(\gamma_{32} - i\omega_{32})\rho_{32} + 2i\alpha_2 cos(\Omega_2 t + k_2 z)(\rho_{33} - \rho_{22}), +2i\alpha_1 cos(\Omega_1 t + k_1 z)\rho_{31} \tag{5.5}$$

$$\varrho_{32} = -(\gamma_{31} - i\omega_{31})\rho_{31} + 2i\alpha_1 cos(\Omega_1 t + k_1 z)\rho_{32}, -2i\alpha_2 cos(\Omega_2 t + k_2 z)\rho_{21} \tag{5.6}$$

$$\varrho_{21} = -(\gamma_{21} - i\omega_{21})\rho_{21} + 2i\alpha_1 cos(\Omega_1 t + k_1 z)(\rho_{22} - \rho_{11}). - 2i\alpha_2 cos(\Omega_2 t + k_2 z)\rho_{31} \tag{5.7}$$

We also use the rotating wave approximation where $2cos \rightarrow 1$ and $\omega \rightarrow \Delta$, the detuning, which simplifies things. In the above equations, ρ_{xx} are the populations of states 1, 2 and 3, ϱ_{xx} are the time derivatives of these populations. ρ_{xy} are the coherences (that is, similarities between) state x and y as a result of the superposition of states x and y and ϱ_{xy} are the time derivatives of these coherences. α_x are the Rabi frequencies, γ_x are the decay rates and R is the loading rate. $cos(\Omega_x t + k_x z)$ are the electric fields provided by the drive lasers. Thus, using the first of these equations as an example, the population of state 3 decreases due to the decay out of it ($\gamma_3\rho_{33}$), but increases due to the laser driving the 3-2 and 2-3 coherences (ρ_{32}, ρ_{23}).

These equations, when solved in the steady state using various different parameters from the 657 nm drive term and for increasing values for the 423 nm drive term, show that it is the intensity of the 423 nm laser that dominates the observed linewidth of the 657 nm feature, as seen in Fig. 5.22.

It can be seen from Fig. 5.22 that with the 423 nm laser running at saturation intensity, as is a typical value during routine operation of the MOT, the 657 nm laser intensity has very little effect on the linewidth of the feature. It is only once the 423 nm intensity drops considerably that the 657 nm laser has an appreciable effect on said linewidth. This shows that in order to see the natural linewidth of the transition the blue laser would need to be run at roughly a millionth of the saturation intensity with the 657 nm laser itself at rather low intensity. This is quite impractical as at such intensities of the blue laser, we would see absolutely no trapped atoms.

Fig. 5.23 shows the same trends as Fig. 5.22, but using actual experimental values used for the 657 nm laser intensity, lowered by way of different combinations of neutral density filters. These correspond, roughly, to the space in between the top two traces in Fig. 5.22.

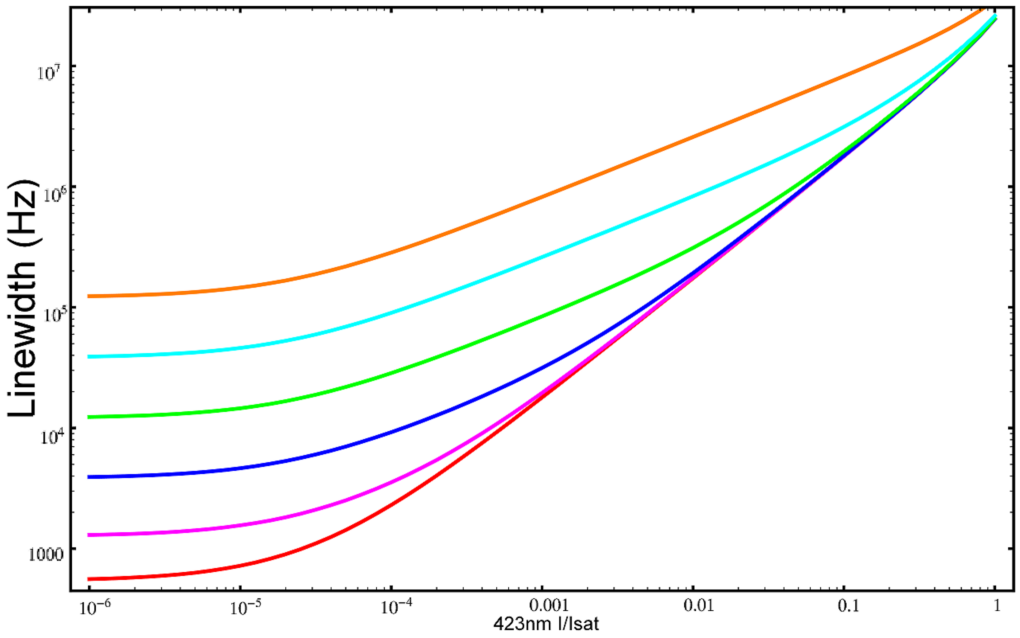

Figure 5.22: The effects of increasing the intensity of the 657 nm laser at varying intensities of the 423 nm transition. The different coloured curves represent different saturation parameters of the 657 nm laser varying in steps of an order of magnitude from 1 (red) to 100,000 (orange).

This shows that, for the experimental parameters used, there is very little difference in the expected linewidths of the 657 nm feature, which reflects the earlier data see in Fig. 5.19.

5.7 Improvements

It seems apparent that, in order to see the natural linewidth of the 657 nm transition, it will be necessary to probe it whilst the 423 nm cooling laser is off. This poses considerable problems, however, not the least of which is that our detection system depends on the fluorescence caused by this transition. No blue light means no fluorescence means no signal. Even more importantly, no blue light means no trapped atoms!

One possible solution would be to insert an AOM into both the blue and the

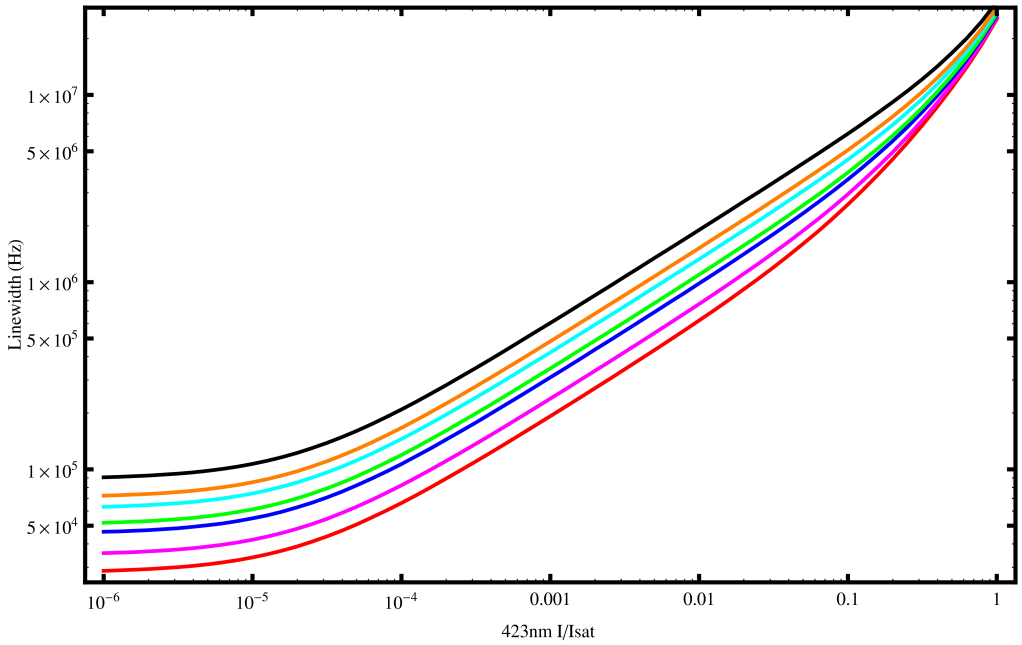

Figure 5.23: The effects of increasing the intensity of the 657 nm laser at varying intensities of the 423 nm transition. The different coloured curves represent different saturation parameters of the 657 nm laser in increasing steps, using actual experimental values. 5412 (red), 8353 (purple), 14118 (blue), 17647 (green), 26118 (cyan), 34353 (orange), 54000(black).

red beams and rapidly cycle the beams on and off so that while the MOT beams are briefly off, the 657 nm laser in on.

5.8 Conclusions

We have designed, constructed and tested an interference filter based external cavity diode laser using a cheap, commercially available astronometric filter. By use of current feed forward and feed back, the laser has been seen to be tunable up to 15 GHz occasionally and 10GHz reliably. Without the feedback and with additional feed forward to the filter rotation angle, the filter would tune only 2GHz. We have used this laser to successfully detect atoms on the 370 Hz wide $4s^2\,{}^1S_0 - 4s4p\,{}^3P_1$ intercombination line at 657 nm.

This laser design has fewer moving parts that can affect the stability of the laser. This is due to the fact that the coarse frequency selective element, the filter, cannot change the length of the cavity in any way. Also, this could perhaps be further improved upon by using a stationary mount for the output coupler, rather than an adjustable mirror mount as was the case in this instance. This would present some problems in getting the cavity to lase (due to an inability to adjust the output coupler orientation), but these should not prove to be insurmountable.

Chapter 6

Conclusions

6.1 Summary

In Chapter 1 a brief history of the work on laser cooling was presented, from the first theoretical papers through to the realisation of BEC by way of the MOT. The specific case of calcium was also presented, along with recent developments in the field.

In Chapter 2 the experimental setup was described, as well as the necessary background theory for each part of the apparatus. The concepts of laser cooling, optical molasses and the Magneto Optic Trap were discussed in depth. The relevant structure of calcium was discussed. The vacuum setup used, including the calcium oven, the Zeeman slower, deflection stage, MOT chamber and the vacuum pumps used was detailed. The optical setup used was also described in detail, including the frequency doubling and saturated absorption spectroscopy setup.

In Chapter 3 the work on the repump transition $4s3d\,{}^1D_2 - 4s5p\,{}^1P_1$ at 672 nm was described. The effects this repump laser had on the MOT were to increase the number of detected trapped atoms by more than an order of magnitude. This was experimentally determined to be by way increasing the MOT lifetime by a factor of three, pumping a factor of two previously undetected atoms out of the ${}^1D_2$ level and by improving the MOT loading rate by a factor of two. A rate equation model was introduced and the discrepancy between experimental results and those predicted by the model were noted. This was concluded to

be due to poorly known rate coefficients. Measurements of the isotope shifts of three naturally occurring calcium isotopes were measured and estimates for three others were made.

In Chapter 4 the work on the repump transition $4s4p\,^3P_1 - 4s3d\,^1D_2$ at 1530 nm was discussed. The effects of the 1530 nm laser alone on the MOT were presented, as well as the effects when used in conjunction with the 672 nm repump laser. It was noted that on its own, the 1530 nm laser causes the MOT to lose atoms, requiring the additional presence of the 672 nm laser to see an increase in the number of trapped atoms. Work carried out on the amplified 1530 nm laser was also presented, detailing the effects of increased power and spectral width of the 1530 nm laser on the MOT. A wavelength measurement was also made.

In Chapter 5 the work on the design, construction and testing of an interference filter based ECDL to probe the $4s^2\,^1S_0 - 4s4p\,^3P_1$ intercombination line at 657 nm was presented. The laser tuning range was tested with several different setups with the maximum tuning range being between 10 and 15 GHz. The setup producing this tuning range was deemed to be impractical however, as it involved modulating the laser current at 20 kHz which would be problematic when reducing the linewidth. It was also determined that the non AR coated interference filter was introducing an extra cavity into the system, reducing the mode-hop free tuning range of the device. The laser was used repeatedly to successfully detect the 370 Hz intercombination line. When the linewidth of the feature was seen to be in the tens of MHz region, it was determined that with the main cooling laser on at the same time as the 657 nm laser, the linewidth would appear to be in the tens of MHz region due to it being a V system.

6.2 Improvements

As noted in the Chapter 2, the lock signal for the 423 nm enhancement cavity was not ideal, causing the cavity to be less stable than might be hoped for. While it was still possible to lock the cavity, improving the lock signal would result in a more stable lock.

It should also be possible to improve the tuning range of the 657 nm laser by a more concerted effort into devising a feed forward circuit that would adjust

both the laser diode current and the filter rotation angle at the same time. The attempts detailed in this thesis were necessarily brief due to time constraints. If the same laser were also locked to the ULE cavity mentioned in Chapter 3, it would result in a significantly narrower laser linewidth which could, if the V system problem explained in Chapter 5 were circumvented, result in a MOT temperature measurement [40].

Other, more practical, improvements which could be made are simply things like replacing ageing hardware (such as the recalcitrant Verdi V8 used to pump the Ti:S laser), installing a complete canopy over the MOT laser table to reduce the quantity of dust collecting on the optical surfaces and installing curtains around the laser tables to reduce the effects of changes in air pressure.

6.3 Future Work

As stated above, reducing the linewidth of the 657 nm laser should, in principle, allow a MOT temperature measurement to be taken. This laser is also seen as the key to cooling to BEC entirely optically. That is, without having to make use of the inherently lossy evaporative cooling techniques. Doing so, however, poses serious challenges. As detailed in Chapter 5, while the main cooling laser is on, the linewidth of the intercombination line is broadened to tens of MHz meaning that this second stage cooling would have to be carried out while the main cooling laser was off. Also, the atoms themselves would have to be supported against gravity to be cooled by such a weak transition. The original plan had been to use the 1530 nm fiber amplifier used in Chapter 4 to create a dipole trap, but the inconsistent output power from the amplifier has made this plan less certain.

What seems certain, however, is that work on the 657 nm laser should continue. The potential to produce a narrow linewidth laser for this intercombination line transition without the mechanical noise incurred by the larger number of beam path influencing movable parts in a typical Littrow configuration ECDL is too great to ignore.

Bibliography

[1] T.W. Hänsch and A.L. Schawlow, *Cooling of gases by laser radiation*, Opt. Commun. **13**, 68 – 69 (1975)

[2] D J Wineland and H Dehmelt, *Proposed* $10^{14}\Delta v < v$ *laser fluorescence spectroscopy on* TI^{+} *III mono-ion oscillator*, Bull. Am. Phys. Soc. **20**, 637 (1975)

[3] *Research groups working with atom traps*, `http://www.uibk.ac.at/exphys/ultracold/atomtraps.html`

[4] William D. Phillips and Harold Metcalf, *Laser Deceleration of an Atomic Beam*, Phys. Rev. Lett. **48**, 596–599 (1982)

[5] Steven Chu *et al.*, *Three-dimensional viscous confinement and cooling of atoms by resonance radiation pressure*, Phys. Rev. Lett. **55**, 48–51 (1985)

[6] Alan L. Migdall *et al.*, *First Observation of Magnetically Trapped Neutral Atoms*, Phys. Rev. Lett. **54**, 2596–2599 (1985)

[7] E. L. Raab *et al.*, *Trapping of Neutral Sodium Atoms with Radiation Pressure*, Phys. Rev. Lett. **59**, 2631–2634 (1987)

[8] Paul D. Lett *et al.*, *Observation of Atoms Laser Cooled below the Doppler Limit*, Phys. Rev. Lett. **61**, 169–172 (1988)

[9] J. Dalibard and C. Cohen-Tannoudji, *Laser cooling below the Doppler limit by polarization gradients: simple theoretical models*, J. Opt. Soc. Am. B **6**, 2023–2045 (1989)

[10] P. J. Ungar, D. S. Weiss, E. Riis, and Steven Chu, *Optical molasses and multilevel atoms: theory*, J. Opt. Soc. Am. B **6**, 2058–2071 (1989)

[11] David S. Weiss *et al.*, *Optical molasses and multilevel atoms: experiment*, J. Opt. Soc. Am. B **6**, 2072–2083 (1989)

[12] M. H. Anderson *et al.*, *Observation of Bose-Einstein Condensation in a Dilute Atomic Vapor*, Science **269**, 198–201 (1995)

[13] K. B. Davis *et al.*, *Bose-Einstein Condensation in a Gas of Sodium Atoms*, Phys. Rev. Lett. **75**, 3969–3973 (1995)

[14] Satyendra Nath Bose, *Plancks Gesetz und Lichtquantenhypothese*, Z. Phys. D **26**, 178 (1924)

[15] Albert Einstein, *Quantum theory of monatomic ideal gases*, Sitzber. Kgl. Preuss. Akad. Wiss., 261(1924)

[16] C.S. Adams and E. Riis, *Laser cooling and trapping of neutral atoms*, Prog. Quant. Electr. **21**, 1 – 79 (1997)

[17] Wolfgang Petrich, Michael H. Anderson, Jason R. Ensher, and Eric A. Cornell, *Stable, Tightly Confining Magnetic Trap for Evaporative Cooling of Neutral Atoms*, Phys. Rev. Lett. **74**, 3352–3355 (1995)

[18] K B Davis, M O Mewes, and W Ketterle, *An analytical model for evaporative cooling of atoms*, Appl. Phys. B **60**, 155–159 (1994)

[19] B. DeMarco and D. S. Jin, *Onset of Fermi Degeneracy in a Trapped Atomic Gas*, Science **285**, 1703–1706 (1999)

[20] Steven Chu, *Nobel Lecture: The manipulation of neutral particles*, Rev. Mod. Phys. **70**, 685–706 (1998)

[21] Claude N. Cohen-Tannoudji, *Nobel Lecture: Manipulating atoms with photons*, Rev. Mod. Phys. **70**, 707–719 (1998)

[22] William D. Phillips, *Nobel Lecture: Laser cooling and trapping of neutral atoms*, Rev. Mod. Phys. **70**, 721–741 (1998)

[23] E. A. Cornell and C. E. Wieman, *Nobel Lecture: Bose-Einstein condensation in a dilute gas, the first 70 years and some recent experiments*, Rev. Mod. Phys. **74**, 875–893 (2002)

[24] Wolfgang Ketterle, *Nobel lecture: When atoms behave as waves: Bose-Einstein condensation and the atom laser*, Rev. Mod. Phys. **74**, 1131–1151 (2002)

[25] Dale G. Fried *et al.*, *Bose-Einstein Condensation of Atomic Hydrogen*, Phys. Rev. Lett. **81**, 3811–3814 (1998)

[26] C. C. Bradley, C. A. Sackett, and R. G. Hulet, *Bose-Einstein Condensation of Lithium: Observation of Limited Condensate Number*, Phys. Rev. Lett. **78**, 985–989 (1997)

[27] G. Modugno *et al.*, *Bose-Einstein Condensation of Potassium Atoms by Sympathetic Cooling*, Science **294**, 1320–1322 (2001)

[28] Tino Weber *et al.*, *Bose-Einstein Condensation of Cesium*, Science **299**, 232–235 (2003)

[29] F. Pereira Dos Santos *et al.*, *Bose-Einstein Condensation of Metastable Helium*, Phys. Rev. Lett. **86**, 3459–3462 (2001)

[30] Yosuke Takasu *et al.*, *Spin-Singlet Bose-Einstein Condensation of Two-Electron Atoms*, Phys. Rev. Lett. **91**, 040404 (2003)

[31] Axel Griesmaier *et al.*, *Bose-Einstein Condensation of Chromium*, Phys. Rev. Lett. **94**, 160401 (2005)

[32] Mingwu Lu, Nathaniel Q. Burdick, Seo Ho Youn, and Benjamin L. Lev, *Strongly Dipolar Bose-Einstein Condensate of Dysprosium*, Phys. Rev. Lett. **107**, 190401 (2011)

[33] Sebastian Kraft *et al.*, *Bose-Einstein Condensation of Alkaline Earth Atoms:* ^{40}Ca, Phys. Rev. Lett. **103**, 130401 (2009)

[34] S. Stellmer, M. K. Tey, R. Grimm, and F. Schreck, *Bose-Einstein Condensation of Strontium*, Phys. Rev. Lett. **103**, 200401 (2009)

[35] Y. N. Martinez de Escobar *et al.*, *Bose-Einstein Condensation of* ^{84}Sr, Phys. Rev. Lett. **103**, 200402 (2009)

[36] P. G. Mickelson *et al.*, *Bose-Einstein condensation of* ^{88}Sr *through sympathetic cooling with* ^{87}Sr, Phys. Rev. A **81**, 051601 (2010)

[37] S. Stellmer, M. K. Tey, R. Grimm, and F. Schreck, *Bose-Einstein condensation of* ^{86}Sr, Phys. Rev. A **82**, 041602 (2010)

[38] O. I. de la Convention du Metre, *The International System of Units (SI)*, Online (2006), 8th Edition

[39] Carsten Degenhardt *et al.*, *Calcium optical frequency standard with ultracold atoms: Approaching* 10-15 *relative uncertainty*, Phys. Rev. A **72**, 062111 (2005)

[40] C. W. Oates, E. A. Curtis, and L. Hollberg, *Improved short-term stability of optical frequency standards: approaching 1 Hz in 1 s with the Ca standard at 657 nm*, Opt. Lett. **25**, 1603–1605 (2000)

[41] St Falke *et al.*, *The* ^{87}Sr *optical frequency standard at PTB*, Metrologia **48**, 399 (2011)

[42] P. Halder, C.-Y. Yang, and A. Hemmerich, *A novel route to Bose-Einstein condensation of two-electron atoms*, arXiv:1201.2573v1 [cond-mat.quant-gas](2012)

[43] C S Adams, S G Cox, E Riis, and A S Arnold, *Laser cooling of calcium in a 'golden ratio' quasi-electrostatic lattice*, J. Phys B **36**, 1933 (2003)

[44] H. Stoehr, F. Mensing, J. Helmcke, and U. Sterr, *Diode laser with 1 Hz linewidth*, Opt. Lett. **31**, 736–738 (2006)

[45] E. Anne Curtis, Christopher W. Oates, and Leo Hollberg, *Quenched narrow-line second- and third-stage laser cooling of* ^{40}Ca, *J.Opt.Soc.Am.B* ***20***, 977 – −984(2003)*U. Dammalapati*et al., Spectroscopy and isotope shifts of the $4s3d\ ^1D_2$˘$4s5p$

[46] *U. Dammalapati, I. Norris, C. Burrows, and E. Riis,* Laser spectroscopy of the $4s4p\ ^3P_2$ ˘ $4s3d\ ^1D_2$ transition on magnetically trapped calcium atoms*, Phys. Rev. A* ***83****, 062513 (2011)*

[48] U Dammalapati et al.*,* A compact magneto-optical trap apparatus for calcium*, Meas. Sci. Technol.* ***20****, 095303 (2009)*

[49] U Dammalapati, I Norris, and E Riis, Saturated absorption spectroscopy of calcium in a hollow-cathode lamp*, J. Phys B* ***42****, 165001 (2009)*

[50] Ian Norris, Laser Cooling and Trapping of Neutral Calcium Atoms*, Ph.D. thesis, University of Strathclyde (2009)*

[51] C. J. Foot, Atomic Physics *(Oxford University Press, 2005)*

[52] Albert Mollema, Laser Cooling, Trapping and Spectroscopy of Ca Isotopes*, Ph.D. thesis, University of Groningen (2008)*

[53] G. W. C. Kaye and T. Laby, Tables of physical and chemical constants *(Longman, 1995)*

[54] D.R. Lide, CRC Handbook of chemistry and physics 74th Edition *(CRC Press, 1995)*

[55] N. Beverini et al.*,* Measurement of the calcium 1P11D2 transition rate in a laser-cooled atomic beam*, J. Opt. Soc. Am. B* ***6****, 2188–2193 (1989)*

[56] Takayuki Kurosu and Fujio Shimizu, Laser Cooling and Trapping of Calcium and Strontium*, Jpn. J. Appl. Phys.* ***29****, L2127–L2129 (1990)*

[57] Andrei Derevianko, Feasibility of Cooling and Trapping Metastable Alkaline-Earth Atoms*, Phys. Rev. Lett.* ***87****, 023002 (2001)*

[58] Jan Grünert and Andreas Hemmerich, Sub-Doppler magneto-optical trap for calcium*, Phys. Rev. A* ***65****, 041401 (2002)*

[59] Carl E. Wieman and Leo Hollberg, Using diode lasers for atomic physics*, Rev. Sci. Instrum.* ***62****, 1–20 (1991)*

[60] P. F. Moulton, Spectroscopic and laser characteristics of $Ti : Al_2O_3$*, J. Opt. Soc. Am. B* ***3****, 125–133 (1986)*

[61] Firuz Torabi-Goudarzi and Erling Riis, Efficient cw high-power frequency doubling in periodically poled KTP*, Opt. Commun.* ***227****, 389–403 (2003)*

[62] P. A. Franken and J. F. Ward, Optical harmonics and nonlinear phenomena

[63] T.W. Hänsch and B. Couillaud, Laser frequency stabilization by polarization spectroscopy of a reflecting reference cavity*, Opt. Commun.* ***35****, 441 – 444 (1980)*

[64] Manual, Varian VacIon Plus 55l/s Diode vacuum pump

[65] N. F. Ramsey, Molecular Beams *(Oxford: New York, 1985)*

[66] Andrew James Murray, Martyn J Hussey, and Michael Needham, Design and characterization of an atomic beam source with narrow angular divergence for alkali-earth targets*, Meas. Sci. Technol.* ***17****, 3094 (2006)*

[67] K. J. Weatherill et al.*,* A versatile and reliably reusable ultrahigh vacuum viewport*, Rev. Sci. Instrum.* ***80****, 026105 (2009)*

[68] Xinye Xu et al.*,* Cooling and trapping of atomic strontium*, J. Opt. Soc. Am. B* ***20****, 968–976 (2003)*

[69] U. Dammalapati, S. De, K. Jungmann, and L. Willmann, Isotope shifts of $6s5d\,^3D - 6s6p\,^1P_1$ transitions in neutral barium*, Eur. Phys. J. D* ***53****, 1–8 (2009)*

[70] A. S. Arnold, J. S. Wilson, and M. G. Boshier, A simple extended-cavity diode laser*, Rev. Sci. Instrum.* ***69****, 1236–1239 (1998)*

[71] Hitachi, HL6545MG Visible High Power LAser Diode for Recordable-DVD

[72] R. L. Kurucz and B. Bell, 1995 Atomic Line Data*, CD ROM No.23 (1995)*

[73] A. G. Adam, T. E. Gough, and N. R. Isenor, CO_2 laser stabilization using an external cavity locked to a reference HeNe laser*, Rev. Sci. Instrum.* ***57****, 6–8 (1986)*

[74] R. Balhorn, H. Kunzmann, and F. Lebowsky, Frequency Stabilization of Internal-Mirror Helium-Neon Lasers*, Appl. Opt.* ***11****, 742–744 (1972)*

[75] Y. Ralchenko, A. Kramida, J. Reader, and NIST ASD Team, NIST Atomic Spectra Database (version 4.1)*, Online (2011),* ***http://physics.nist.gov/asd***

[76] R. Drozdowski, J. Kwela, and M. Walkiewicz, Lifetimes of the 4s4p 3P1 and 4s3d 1D2 states of Ca I*, Z. Phys. D* ***27****, 321–324 (1993)*

[77] W. Nortershauser, N. Trautmann, K. Wendt, and B.A. Bushaw, Isotope shifts and hyperfine structure in the $4s^2 {}^1S_0 - 4s4p {}^1P_1 - 4s4d {}^1D_2$ transitions of stable calcium isotopes and calcium-41*, Spectrochim. Acta. B* ***53****, 709 – 721 (1998)*

[78] R. Ciuryło, E. Tiesinga, and P. S. Julienne, Optical tuning of the scattering length of cold alkaline-earth-metal atoms*, Phys. Rev. A* ***71****, 030701 (2005)*

[79] G. M. Rasibeck and F. Yiou, Possible use of ^{41}Ca for radioactive dating*, Nature* ***277****, 42 (1979)*

[80] David Elmore, Maryka H. Bhattacharyya, Nancy Sacco-Gibson, and David P. Peterson, Calcium-41 as a long-term biological tracer for bone resorption*, Nucl. Intrum. Meth. B* ***52****, 531 – 535 (1990)*

[81] I. D. Moore et al.*,* Counting Individual ^{41}Ca Atoms with a Magneto-Optical Trap*, Phys. Rev. Lett.* ***92****, 153002 (2004)*

[82] S. Hoekstra et al.*,* Single-atom detection of calcium isotopes by atom-trap trace analysis*, Phys. Rev. A* ***71****, 023409 (2005)*

[83] W. H. King, Comments on the Article "Peculiarities of the Isotope Shift in the Samarium Spectrum"*, J. Opt. Soc. Am.* ***53****, 638–639 (1963)*

[84] K. Heilig and A. Steudel, Changes in mean-square nuclear charge radii from optical isotope shifts*, At. Data Nucl. Data Tables* ***14****, 613 – 638 (1974)*

[85] S. F. Jacobs, ed., Variable invariables: dimensional instability with time and temperature (Proceedings Paper)*, Vol. CR43 (SPIE, 1992)*

[86] Amnon Yariv, Optical Electronics 3rd Edition *(Holt, Rinehart and Wilson, Inc, 1985)*

[87] C W P Palmer et al.*,* Laser spectroscopy of calcium isotopes*, J. Phys. B* ***17****, 2197 (1984)*

[88] Stig Stenholm, Foundations of Laser Spectroscopy *(Dover Publications, New York, 2005)*

[89] Harold J. Metcalf and Peter van der Straten, Laser Cooling and Trapping *(Springer-Verlag New York, 1999)*

[90] J.J. Olivero and R.L. Longbothum, Empirical fits to the Voigt line width: A brief review*, J. Quant. Sprectrosc. Radiat. Transfer* ***17****, 233 – 236 (1977)*

[91] P. Zorabedian and Jr. W. R. Trutna, Interference-filter-tuned, alignment-stabilized, semiconductor external-cavity laser*, Opt. Lett.* ***13****, 826–828 (1988)*

[92] X. Baillard et al.*,* Interference-filter-stabilized external-cavity diode lasers*, Opt. Commun.* ***266****, 609 – 613 (2006)*

[93] Daniel J. Thompson and Robert E. Scholten, Narrow linewidth tunable external cavity diode laser using wide bandwidth filter*, Rev. Sci. Instrum.* ***83****, 023107 (2012)*

[94] Th. Kisters, K. Zeiske, F. Riehle, and J. Helmcke, High-resolution spectroscopy with laser-cooled and trapped calcium atoms*, Appl. Phys. B* ***59****, 89–98 (1994)*

[95] Th. Udem et al., Absolute Frequency Measurements of the Hg^+ and Ca Optical Clock Transitions with a Femtosecond Laser, *Phys. Rev. Lett.* ***86*** *(2001)*

[96] R. W. P. Drever et al., Laser phase and frequency stabilization using an optical resonator, *Appl. Phys. B* ***31****, 97–105 (1983)*

[97] Eric D. Black, An introduction to Pound–Drever–Hall laser frequency stabilization, *Am. J. Phys.* ***69****, 79–87 (2001)*